Myocardial tissue characterization with motion-corrected 3D whole-heart MRI

Lopez Gonzalez, Karina

Awarding institution:
King's College London

King's College London

Myocardial Tissue Characterization with Motion-Corrected 3D Whole-Heart MRI

Karina López González

Supervised by

René Botnar, Ph.D.

Reza Razavi, M.D.

Thesis submitted to King's College of London for the degree of Doctor of Philosophy

July 2020

Chapter 1 Front Matter

Abstract

The aim of this project was to develop novel quantitative MR techniques to characterise cardiac tissue for the management of cardiac arrhythmias without the use of exogenous contrast agents to improve patient safety and allow scar imaging during and after ablation therapy. This project had a particular focus on driving the innovation that underpins an interventional MRI electrophysiology program, e.g., developing techniques for the assessment of the arrhythmia substrate within the atria and ventricles, guiding risk stratification and intervention planning. These techniques would often relate to substrate analysis for ventricular tachycardia (VT) and atrial fibrosis assessment, including fibrosis/scar quantification and wall thickness. Indeed, MR imaging has been used extensively for characterisation of the arrhythmic substrate for both atrial and ventricular arrhythmias. However, such MR techniques remain imperfect, and substantial clinical impact is anticipated from the development of robust techniques for the assessment of atrial and ventricular substrate. Because the imaging challenge is generally greatest for the thin walled atrial myocardium, techniques are often developed for ventricular imaging in the first instance, as it is the case for this study.

As described in the following Chapters, imaging solutions to the above challenges were implemented during the course of this project. This report lays out the theoretical basis and experimental results of roughly 4 years of research on the area of contrast-free quantitative magnetization transfer imaging for myocardial tissue characterization and in-vivo assessment of myocardial fibrosis in patients.

Chapters 1-4 describe the clinical background, mathematical and physical concepts necessary to understand and evaluate the methods developed herein. Chapters 5-7 describe the methods, experimental results and conclusions obtained. Specifically, Chapters 5 and 6 are adaptations of two manuscripts submitted and accepted[1] for publication in peer-reviewed international journals (MAGMA

[1] The manuscript presented in Chapter 6 has been published on 17 November 2020 in *Magnetic Resonance in Medicine*,, https://doi.org/10.1002/mrm.28577 .

and MRM, respectively). Chapter 7 is the result of the last few months of this project and has not yet been submitted for external review.

As a result of the research carried out, and in addition to the work presented herein, I attended three consecutive annual meetings of the International Society for Magnetic Resonance in Medicine (ISMRM) with abstract presentations and obtained two Magna Cum Laude Awards (2017 and 2019). I also attended and presented an abstract at the annual meeting of the Society for Cardiovascular Magnetic Resonance (SCMR) in February 2019 in the USA and presented posters at numerous events in London (UK) between 2016-2019.

Acknowledgements

I would like to thank all the great scientists who have contributed directly or indirectly to this work. First, without the help and support of Radhouene Neji and my supervisor, René Botnar, I cannot imagine having learned nor delivered anything close to the subject matters discussed in this report. To both, I admire your technical capabilites and experience but, above all, I appreciate your endless patience. I consider myself lucky to have spent these 4 years under your guidance.

Although I'm a rather private and introverted person, I was made to feel welcome in our research group at St Thomas' Hospital and I would like to thank everyone for their constant support, collaboration and time. Special thanks to Camila Muñoz and Giovanna Nordio for all the handy tips, tutoring, and, crucially, editing of parts of this report. Thanks and best wishes to all the "healthy subjects" (and great colleagues) always willing to give me an hour of their time, Andreia Gaspar, Olivier Jaubert, Aurélien Bustin, Giorgia Milotta, Giulia Ginami, Gastao Cruz, Begoña Lavín, Haikun Qi and Teresa Correia. Many thanks also for the invaluable advice (and patience through multiple manuscript writing iterations) to Claudia Prieto, Sébastien Roujol, Shaihan Malik and Imran Rashid.

Finally, I want to thank my family for their love and encouragement throughout. The finalization of this step of my career is only the result of a concerted group effort of which I admittedly benefit the most. This would not have been possible without the loving advice and support of my husband and my parents, which gave me strength and comfort when I was most in distress.

Gracias.

Contents

List of Figures

Chapter 2 : Myocardial Tissue Characterization

Abstract

This chapter will discuss the clinical motivation for this research, including the fundamentals of the most widely adopted techniques in cardiac MR for the detection of myocardial fibrosis, highlighting its main advantages and challenges. State-of-the-art research in contrast and non-contrast enhanced and quantitative MRI for the detection of myocardial fibrosis will be discussed, including late gadolinium enhancement, T1, T2, and T1-rho mapping. Finally, the physics and motivation for the use of Magnetization Transfer will be described, with an emphasis on its current clinical applications and the potential of novel quantitative approaches in non-contrast enhanced myocardial tissue characterization.

The clinical problem: cardiac fibrosis

Cardiac fibrosis consists of a thickening of connective tissue in the heart which affects either the heart's valves or muscle, the latter also called myocardial fibrosis. Cardiac fibrosis has been shown to have prognostic value in heart failure [1] and a variety of cardiomyopathies [2]. More specifically, myocardial fibrosis can be a substrate for arrhythmia [3]. For these reasons, determination of the characteristics, shape and extent of cardiac fibrosis is of utmost importance in the diagnosis and treatment of many cardiovascular patients.

Fibroblasts and collagen

The heart is a very complex organ whose function is to maintain the circulation of blood throughout the body, pumping deoxygenated blood from all the organs to the lungs while pushing oxygenated blood from the lungs to all the organs. The heart is a muscle in perpetual motion, wherein each heart beat comprises a phase of contraction (systole) and a phase of relaxation (diastole), orchestrated by a number of cell types including myocytes, smooth muscle cells, endothelial cells and large amounts of connective tissue [4]. The fibrous structure

that connects all muscle cells and helps to transmit the contractile motion of individual cardiomyocytes is called the extracellular matrix (ECM) and is maintained by cardiac fibroblasts, arguably the most abundant cell type in the heart [5].

In addition to their role in regulating the structural integrity of the ECM in healthy myocardium, cardiac fibroblasts differentiate as myofibroblasts upon external mechanical stimulus by expressing contractile proteins and increased migratory and secretive properties, which are key to their functional role in the heart [6]. Myofibroblasts play an important role in the regulation of many processes in the remodelling heart by generating provisional and structural proteins for the ECM, growth factors, cytokines and proteases during cardiac fibrosis and inflammation [7].

Proteins such as collagen I and III are key components of the ECM and comprise 85% and 11% of total volume in the cardiac interstitium in primates, respectively [8]. A disturbance in the balance of normal degradation and synthesis of the proteins that compose the ECM, e.g. collagens, affects the integrity of cardiac structure and may compromise cardiac function. For example, degradation of cross-links between collagen fibres weakens the ECM and may lead to systolic dysfunction [9]. On the other hand, increased collagen volume fraction in the hypertrophic myocardium is associated with stiffness and diastolic dysfunction [10]. Impaired electrical conduction as a result of cardiac remodelling and fibrosis may create loops (or re-entry circuits) and ultimately leads to arrhythmia [11].

Replacement and reactive fibrosis

Cardiac fibrosis entails an excess of fibrous tissue in the heart caused by a disruption in the normal balance between production and degradation of the proteins that form the ECM, i.e., when the degradation does not keep up with the production. In myocardial fibrosis, elastin and collagen fibres overpopulate the interstitium of the myocardium. This process can be triggered

by cell death, pressure overload, inflammation, toxic agents or metabolic disturbances, among others. After myocardial ischaemia, some parts of the myocardium might not be able to recover, and massive cell death ensues (**Figure 2-1A**). The fibrotic process that follows cell death in the myocardium can be broadly divided in three parts: inflammation and oedema, proliferation of myofibroblasts, and maturation of a collagenous scar which replaces the dead cardiomyocytes. The purpose of this *replacement* cardiac fibrosis is to prevent the debilitated injured myocardium from causing further complications such as ventricular dilation or even rupture [12]. Myocardial fibrosis triggered by other than cell death is often called *reactive* fibrosis and consists of systemic collagen deposition in the extra cellular and perivascular space (**Figure 2-1B** and **Figure 2-1C**). An increase in pressure load due to hypertension may cause extensive fibrosis through perivascular macrophage infiltration, which in turn affects fibroblast differentiation and proliferation [13]. Hypertensive cardiac fibrosis is one of the main causes of myocardial stiffness and may lead to both diastolic and systolic failure [14]. For all these reasons, evaluation of the extent of fibrosis (whether replacement or reactive fibrosis) is critical for patient prognosis and to improve our understanding of the mechanisms that cause heart failure [4].

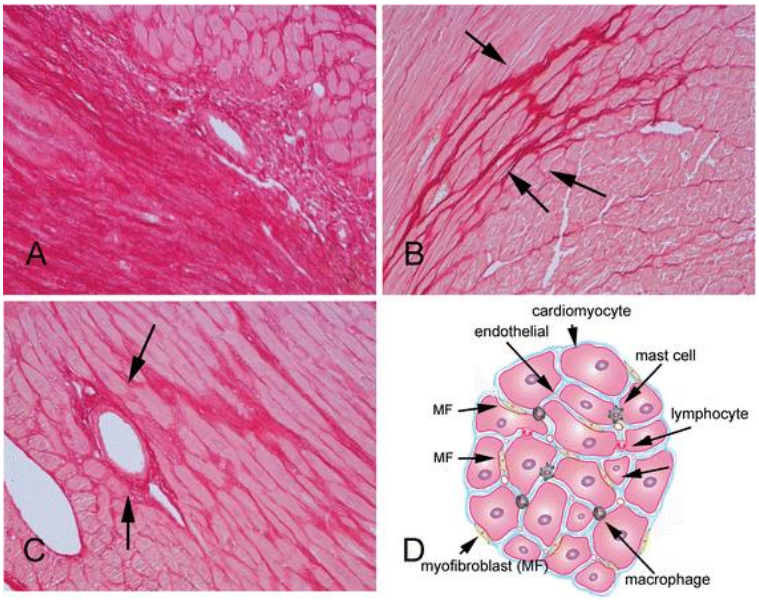

***Figure 2-1**. Different types of cardiac fibrosis in mouse models. A) Post-myocardial infarction replacement fibrosis. B) Interstitial fibrosis with increased deposition of collagen (black arrows) in the absence of cardiomyocyte death. C) Perivascular fibrosis with increased collagen (black arrows) in the vascular adventitial matrix. D) Schematic drawing of myocardial fibrosis, highlighting all the main effector cells involved. Figure obtained from Ping et al. [12], copyright license order number **4677070657265** RightsLink / Springer Nature.*

Basics of magnetic resonance imaging

In the simplest Nuclear Magnetic Resonance (NMR) experiment, the setting comprises a collection of atoms with non-zero nuclear spin which are placed under the influence of an external static magnetic field. This external field aligns their magnetic moment $\vec{\mu}$ either parallel or anti-parallel to it, where the distribution of spins in one or the other state follows a Boltzmann distribution and depends generally on the temperature and field strength (see scheme in **Figure 2-2**). In this situation, the magnetic moment of a single atom may be understood as having two

separate components: the longitudinal moment which is oriented in the direction of the external magnetic field, and the transverse moment which lays in the perpendicular plane. From the point of view of quantum mechanics, as the longitudinal moment is fully determined by the external magnetic field, the transverse moment becomes undefined until it is disturbed, following Heisenberg's Uncertainty Principle. On the other hand, using the classical analogy of a magnetic dipole, the transverse moment of each atom is considered to 'spin' around the longitudinal axis at a resonant frequency ω proportional to the magnitude of the external magnetic field B_0, with proportional constant γ (the gyromagnetic ratio). The phase of the rotation is arbitrary and therefore the net transverse magnetization for a large ensemble of nuclei is zero.

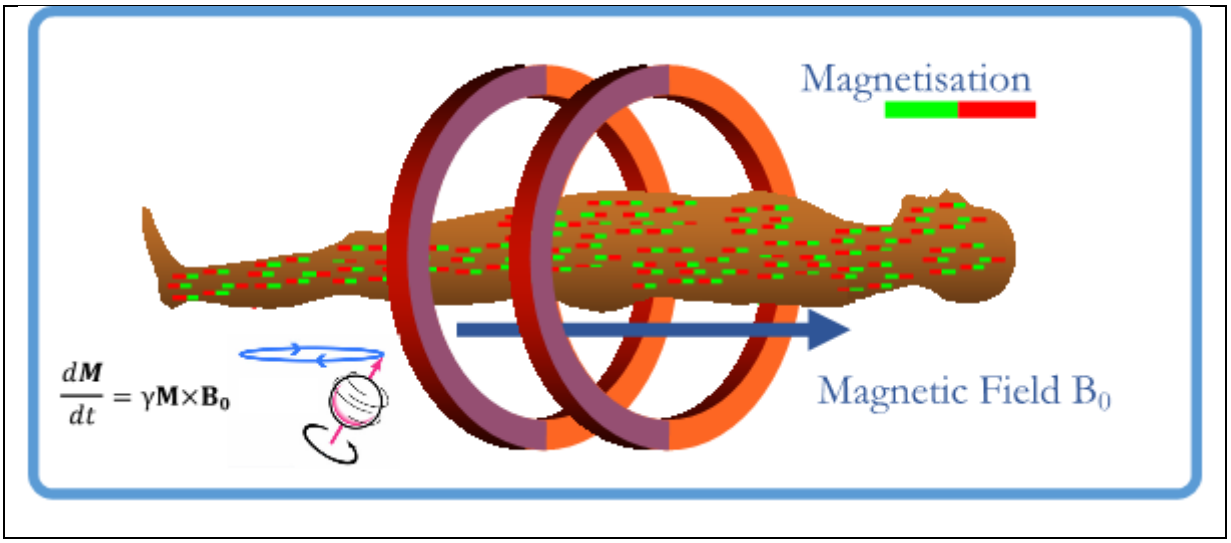

Figure 2-2. The nuclear magnetic resonance experiments involves a large static magnetic field B_0 acting upon a collection of magnetic dipoles, wherein the net longitudinal magnetization M_0 follows a Boltzmann distribution which is proportional to the strength of the external magnetic and inversely proportional to the temperature of the ensemble.

The second part of the experiment consists of the signal generation and collection. The signal is generated by irradiating the ensemble of nuclei with a magnetic field B_1 (with $\vec{B}_1 \perp \vec{B}_0$) oscilates at the Larmor frequency ω_0 (on-resonance), which *tips* the net magnetization vector

into the transverse plane, where it can be measured by magnetic induction using a receiver coil positioned perpendicular to the B_0 field (see scheme in **Figure 2-3**). The irradiation field (or usually called excitation) may be generated with a quadrature body coil set which creates a uniform (but rotating) B_1 field while the transverse magnetisation is either measured with the same body coil or with a dedicated receiver coil. In the quantum framework, the introduction of energy into the system in the form of photons with angular frequency ω_0 allows the spins to transition from the state of lower energy to the state of higher energy (e.g., from parallel to anti-parallel for protons). As soon as the external photon radiation is over, the spins return to the ground state, back to thermal equilibrium by photon emission. The energy of the transition $E = \hbar\,\gamma B_0 = \ h\omega_0$ has the same characteristic frequency ω_0, that is, the Larmor frequency. This response is commonly referred to as Free Induction Decay (FID).

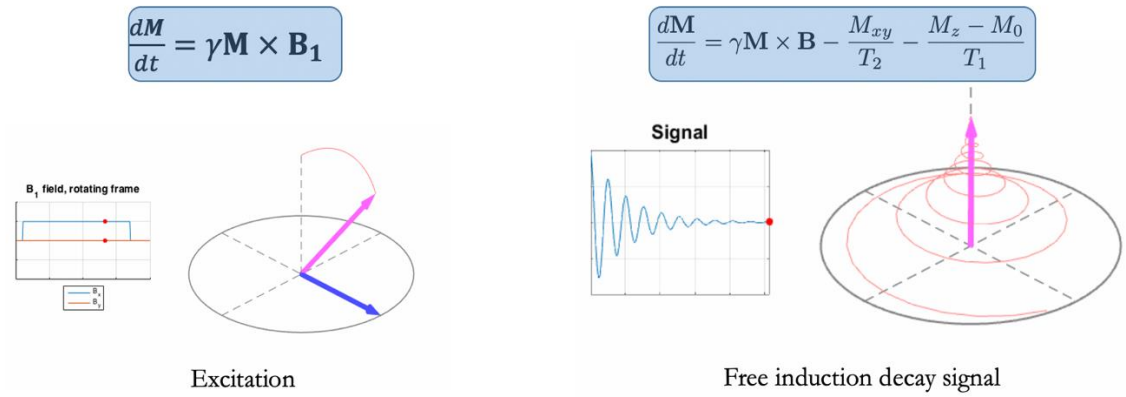

***Figure 2-3**. Scheme of net magnetization M (pink) under the influence of the static excitation magnetic field B1 in the rotating frame, and under the influence of the main magnetic field B0 (after B1 has been turn off) resultinh in the Free Induction Decay (FID), which is also described as the MR signal. T1 and T2 are the longitudinal and transverse relaxation times that govern the return to the equilibrium magnetization M_{z0} and the decay of the MR signal, M_{xy}.*

There are two intrinsic processes which modulate the signal collected in magnetic resonance imaging. First, the FID signal is a sine wave whose amplitude is exponentially modulated by the dephasing of the transverse magnetization due to interactions between excited spins and

the inhomogeneity of the external static magnetic field, ΔB_0. The decay constant of this modulation is called T2*, or T2 if the static magnetic field is assumed perfectly homogeneous (or the inhomogeneity can be corrected). The other modulating process comes from the fact that MRI is a raster scanning system, which requires the acquisition of a large set of signals, one by one, in order to provide spatial localization. A train of radiofrequency (RF) pulses is applied and a train of MR signals is collected after every pulse, respectively, creating a signal modulation along the data acquisition train related to the restoration of the net equilibrium magnetization during the time between RF pulses (commonly referred to as TR). The exponential recovery of the thermal equilibrium is given by the interactions between excited and non-excited nuclei, also called spin-lattice interactions. The characteristic time constant for this recovery is called T1 relaxation.

Spin to lattice relaxation and T1 mapping

Spin-lattice relaxation can give valuable information about the tissue studied, because it relates to structural properties of the molecules such as their size and molecular tumbling. Generally, T1-related processes are made more efficient and quicker when molecules natural rotation rates (or correlation times) approach the Larmor frequency, since the probability of interaction with the excited spins increases (see scheme in **Figure 2-4**). Protons within long lipid chains typically have short T1 recovery times, given that the complicated molecular tumbling of such structures spans a large spectrum of frequencies, often including the Larmor frequency. Large macromolecules and proteins have slower correlation times, often significantly below the Larmor frequency, thus they have longer T1. Very small molecules such as those found in fluids (e.g. H2O) have fast free motion, often beyond the Larmor frequency, which also translates into long T1 times.

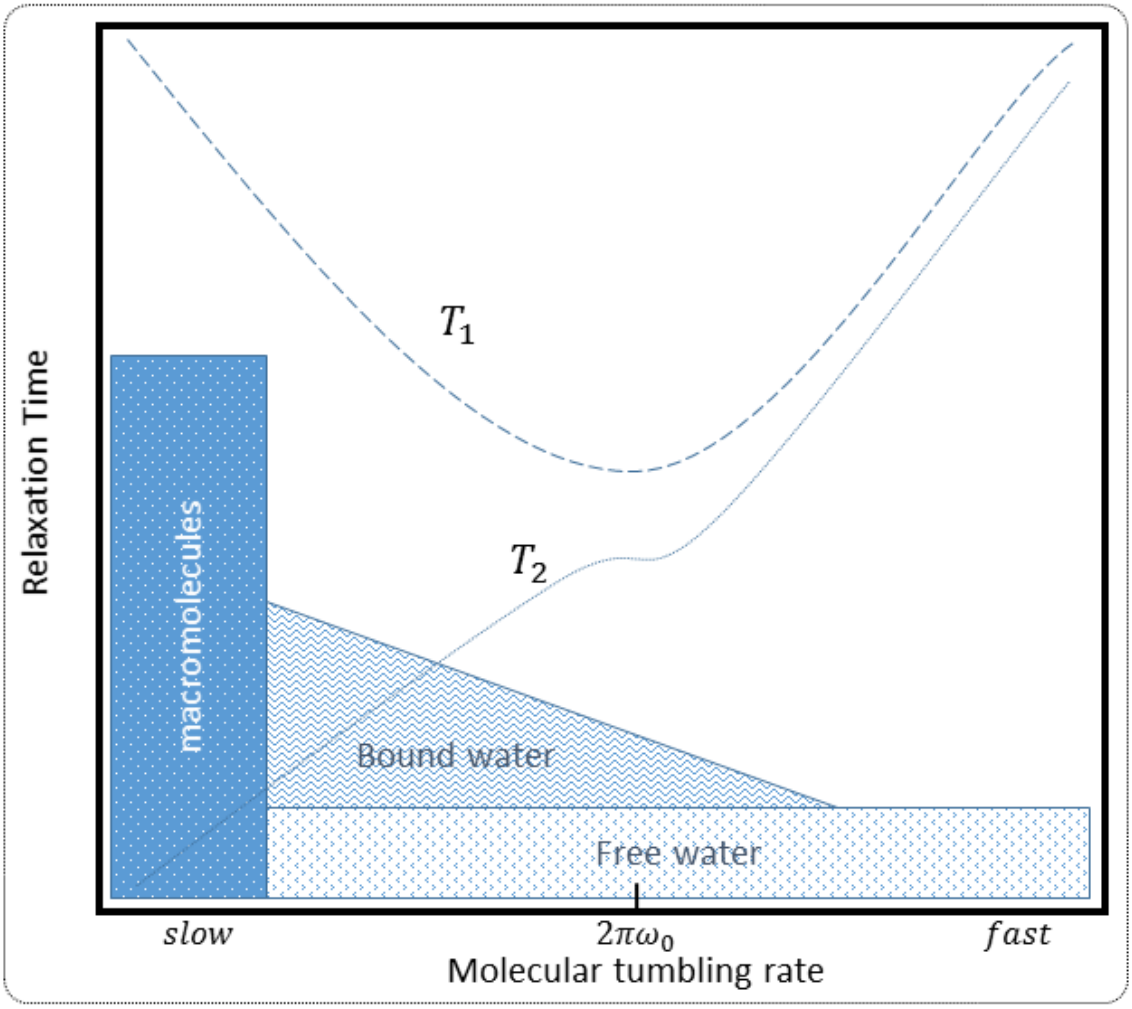

***Figure 2-4**. Scheme of T1 and T2 characteristic relaxation associated with the molecular tumbling rate for different types of lattices, including macromolecules, 'bound' water protons (attached to macromolecules), and free water protons. Molecular tumbling rate is a function of many molecular characteristics though a main contributing factor is molecular size. Small molecules such as free water spin fast while large macromolecules spin slowly. T1 is the most efficient when the molecular tumbling rate coincides with the spinning of the excited nuclei (at the Larmor frequency, $2\pi\omega_0$) since the likelihood of spin-to-lattice interactions is maximised.*

T1 mapping techniques aim to quantify T1 values by acquiring a train of T1 weighted images at different points along the exponential recovery curve of the longitudinal magnetization, which can then be fitted to a model to obtain the characteristic time constant. The simplest model suggests that T1 recovery is mono-exponential after a saturation or inversion pulse:

$$I(t) = A + B\, e^{-t/T_1} \tag{2-1}$$

Here, I is the total magnetization after time t, where A and B are functions of the initial and the equilibrium magnetization while T_1 is the characteristic time constant. T1 modulation is controlled using preparation pulses that invert the net magnetization (or inversion pulses) prior to the signal acquisition so the difference in magnetization between spins and lattice is maximized.

A common T1 mapping technique used in cardiac imaging is the modified Look-Locker inversion recovery (MOLLI) sequence [15]. The Look-Locker (LL) experiment [16] consists of a single inversion pulse followed by train of images acquired at regular intervals τ with the first image acquisition starting at time *TI* after the inversion pulse. In this case, the model follows the same mono-exponential form as in equation *(2-1*), but the parameters also depend on the characteristics of the image acquisition such as the flip angle α and τ, which can be written as [17]:

$$I(n\tau) = m_\infty - (1 + m_\infty)e^{-\frac{n\tau}{T_1^*}};\ n \in \mathbb{N} \tag{2-2}$$

with,

$$m_\infty \equiv \frac{1 - e^{-\tau\,/\,T_1}}{1 - e^{-\tau\,/\,T_1^*}}$$

$$T_1^* \equiv \left\{-\frac{1}{T_1} - \frac{\ln(\cos\alpha)}{\tau}\right\}^{-1}$$

Here, a spoiled gradient echo acquisition with flip angle α is assumed. T_1 is calculated using the measured T_1^* and the sequence parameters. Because cardiac imaging is constrained by cardiac and respiratory motion, the MOLLI sequence combines multiple LL experiments with different *TI* and only a few images (3 to 5) per train, as shown in **Figure 2-5**, in order to

efficiently sample the recovery curve for a limited time or phase during each cardiac cycle and in a total scan time no longer than a patient's breath-hold (<20 sec).

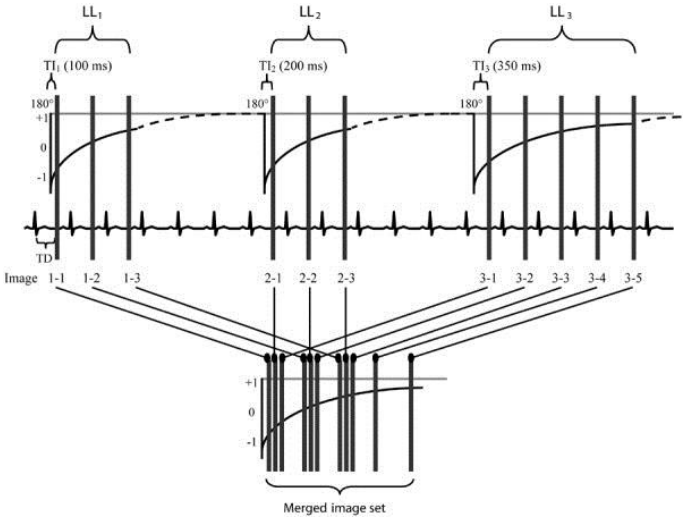

***Figure 2-5**. Modified Look-Locker (MOLLI) pulse diagram where vertical bars represent image acquisition and dashed lines represent periods of relaxation. Three sets of Look-Locker experiments are performed with increasing inversion times (TIs). Trigger delay (TD) typically selects end-diatolic resting period. After acquisition, the eight images are re-grouped according to their effective TI for calculation of the T1 constant. Figure obtained from Messroghli et al. [15], copyright license order number **4677090059585** RightsLink / John Wiley and Sons.*

Single T1-weighted images have been used to observe both functional [18] and structural [19] changes in the brain. However, these are qualitative changes that are difficult to compare among subjects, between sequences and scanners, and may only be observed if focal T1 alterations exist. The quantitative nature of T1 mapping allows to observe global or diffuse changes in T1 that are normally associated with early stages of disease or disease type [20]. In cardiac imaging, T1 mapping techniques have been used to detect oedema with [21] and without infarct [22], as well as chronic myocardial infarction [23] and diffuse fibrosis [24]. However, the native T1 differences between normal myocardium, acute infarction, chronic

infarction and diffuse fibrosis might be very small so the sensitivity is low and only iron overload, amyloidosis and Fabry's disease can be detected reliably with native T1 mapping [25]. Furthermore, T1 values may not be reproducible between different T1 mapping approaches [26], thus, each T1 mapping sequence has sequence specific normal or reference values.

Transverse relaxation and T2 mapping

The dephasing of the transverse magnetization occurs due to local inhomogeneity of the magnetic field, either caused by the proximity of neighbouring nuclei (spin-spin interaction; T_2 relaxation) or the presence of imperfections in the external static magnetic field (T_2^* relaxation). The rate of change of the transverse magnetization due to T_2 relaxation is proportional to the number of interacting spins and therefore proportional to the total magnetization itself. The evolution of the transverse magnetization $I(t)$ in the presence of a homogenous external static magnetic field can be modelled by an exponential decay where the time constant T_2 is, among others, a function of the mean free path or density of excited spins:

$$I(t) = A + B\, e^{-t/T_2} \tag{2-3}$$

Here, *B* is a constant dependent of the initial transverse magnetization $I(0)$ and *A* is zero in the absence of bias. Generally, T1 and T_2 times are different. In soft tissue and semi-solids, T_2 times are typically orders of magnitude shorter than T1 [27].

T_2 weighting of the signal occurs during the time between excitation and acquisition of the MR signal or, in other words, the time that the magnetization spends in the transverse plane. The most efficient way to control the amount of T_2 weighting in cardiac MRI is to use a magnetization preparation scheme that encodes transverse magnetization relaxation into the longitudinal magnetization right before the image acquisition [28]. Generally, this can be achieved by applying an excitation pulse (90˚) which tips the longitudinal magnetization into

the transverse plane, followed by a train of refocusing pulses (180˚) at regular intervals to keep spin-to-spin relaxation going for the desired TE, and finalising with a tip-up pulse (90˚) to restore the modulated magnetization back into the longitudinal direction (a detailed scheme is also shown in **Figure 2-6**).

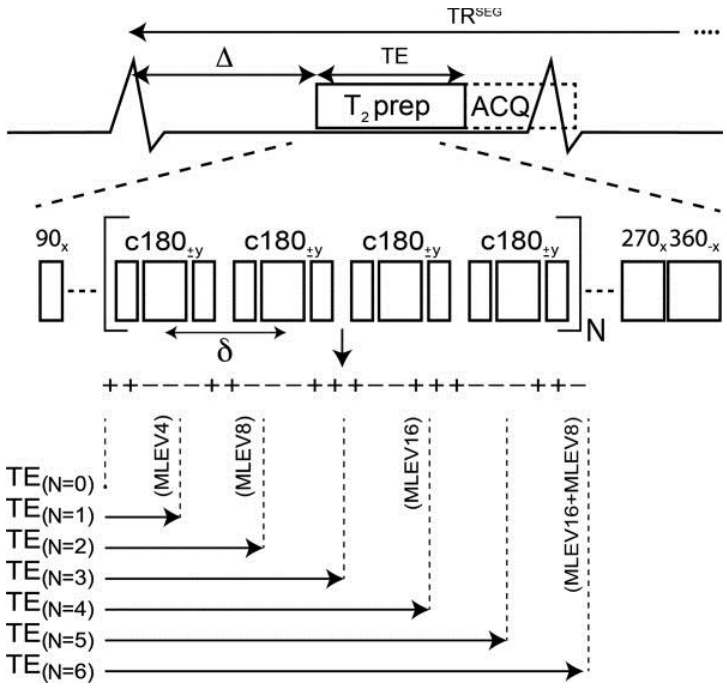

***Figure 2-6**. Mouse cardiac T2-prepared mapping scheme. Seven images are acquired at different echo times (TE) with preparation consisting of: (I) a 90˚ excitation pulse, (II) 'N' blocks of four composite 180˚ (refocusing) pulses ($c180_{\pm y}$) with MLEV16 phase cycling pattern, and (II) a composite 90˚ flip back pulse. Length of T2-prep and ACQ modules is not drawn at scale. Figure obtained from Coolen et al. [29], copyright license order number **4677130605754** RightsLink / John Wiley and Sons.*

T_2 or T_2^*-weighted images have been used in multiple applications including localization of micro-haemorrhages in the brain [30] (T_2^*), cartilage defects or depletion [31] (T_2), characterisation of atherosclerotic plaques [32] (T_2), and localization/extent of myocardial injury and area at risk (demarcated by extent of oedema) in ischemic and non-ischemic disease [33] (T_2). In most of the cases, T_2 findings are related to changes in the tissue's water content,

such as in an early study in acute myocardial infarction in dogs by Higgins *et al.* [34], where T_2 values in the infarcted area correlated with percent water content measurements from histology.

T2 mapping consists in the acquisition of a series of images n at different TEs (TE_i , $i = 1..n$) or, most commonly, the acquisition of a series of images n with constant TE but a respective preceding T2 preparation stage where T2 weighting associated with varying TEs is encoded into the longitudinal magnetization (see **Figure 2-6**). The images allow to estimate the T2 time constant using a two or three parameter model, e.g., as the model described in equation *(2-3*) where each TE_i is a different t in the $I(t)$ curve. Approaches to T2 mapping in the heart have shown similar potential for the localization of oedema [35] and haemorrhage [36] with respect to single T2-weighted images, however with improved robustness against coils sensitivity and heart motion [37]. T2 values in the healthy myocardium have generally shown significant inter-subject variability, demonstrating good sensitivity but perhaps low specificity to inflammation, including oedema [38].

Contrast agents

Late Gadolinium Enhancement

Late gadolinium enhancement (LGE) MRI is the gold standard for the assessment of myocardial fibrosis [39]. LGE shows enhanced signal intensity in the area of fibrosis because of accumulation and delayed washout of Gadolinium-based contrast agents in the enlarged extracellular space [2].

Gadolinium is a paramagnetic material with up to seven unpaired electrons (Gd+++). When placed in biological tissue it accelerates both the restoration of the equilibrium magnetization and the dephasing of the transverse magnetization after an RF excitation, generating an

effective shortening of T1 and T2. This is mostly due to its strong magnetic moment and multiple coordination sites open for fast-exchanging water protons [40].

Free gadolinium molecules (or other metallic ions) can have toxic effects in the body so they require complexation when administered in-vivo. Gadolinium is known to form a highly thermodynamically stable compound with *diethylenetriamine pentaacetic acid* (DTPA), with a strong binding/formation constant of log K=22-23 [41]. The chelated ion (Gd-DTPA) is a large hydrophilic molecule typically unable to cross barriers such as cell membranes, therefore it its distributed mostly in the extracellular space [40]. This kinetics contributes to its non-toxicity and also forms the basis for its application in the assessment of myocardial fibrosis.

The use of Gd-DTPA LGE for the localization of acute myocardial infarction was demonstrated in dogs [42] and humans [43] as early as 1986. Nowadays, LGE is mainly used to assess the extent, localization, and viability of infarcted myocardium, however, its enhancement is non-specific and has also been observed in fibrotic tissue associated to non-ischaemic diseases such as myocarditis, cardiac sarcoidosis, neoplasms and congenital diseases [44].

Despite its many advantages LGE is a qualitative imaging technique that is unsurpassed for the detection of focal "replacement" fibrosis but can be challenging to use for the detection of diffuse "reactive" fibrosis. The intensity and pattern of signal enhancement using paramagnetic contrast agents such as Gd-DTPA (or newer, more stable Gd-DOTA) depend on the pharmacokinetics (target tissue and lesion) and the native contrast associated with imaging sequence parameters such as flip angle, TE/TR times and preparation pulses. For example, the pattern of enhancement in myocardial infarction findings is affected by the dose and time point of imaging after the injection of the contrast agent. While core infarct regions enhance strongly and late during the contrast wash-out (> 20 min), the signal from the rim of an infarcted region (area at risk) might enhance very early on (2-3 min, typically called early gadolinium

enhancement (EGE)), only to return to normal at later stages [45]. The pathology and patient-specific perfusion kinetics may also affect the wash-in/wash-out timings. Furthermore, reactive fibrosis or similar cardiomyopathies which often result in diffuse fibrosis in the myocardium are difficult to assess using LGE because a reference signal from healthy myocardium is needed in order to observe the signal enhancement associated with the pathology.

Extracellular volume measurements

A quantitative technique that combines LGE and T1 mapping has been used in the assessment of reactive or diffuse fibrosis [46], which consists in the measurement of the fractional volume of the extra-cellular (or interstitium) with respect to the intra-cellular space. The key hypothesis of extra-cellular volume (ECV) techniques is that the expansion of the ECM is directly driven by the characteristic excess of collagen deposition in cardiac fibrosis [47], at least in the absence of other culprits such as amyloidosis or oedema. ECV techniques do not measure other structural characteristics of the ECM such as the degree of cross-linking or specific ECM protein types such as collagen, elastin or proteoglycans.

An ECV map is obtained by calculating the difference in the relaxation rates ΔR_1 $(1/\Delta T_1)$ before and after the injection of a Gd-based contrast agent, in the myocardium and blood. The contrast agent bolus is slowly injected into the bloodstream and diffuses exclusively to the extracellular space in tissue until its concentration in the blood and tissue compartments reaches an equilibrium. The difference in the relaxation rates $\Delta R1$, pre- and post-contrast, is proportional to the concentration of Gd in a given voxel. If the distribution of contrast agent in the blood was assumed uniform, the ratio between ΔR_1 in myocardium and ΔR_1 in blood would be the partition coefficient of extra- to intra-cellular space in the myocardium. However, Gd-based contrast agents are typically too big to enter red blood cells and they remain exclusively in the plasma. In order to quantify ECV, the haematocrit fraction must be measured [48]:

$$ECV = (1 - haematocrit)\frac{\Delta R_1^{myo}}{\Delta R_1^{blood}} \quad (2\text{-}4)$$

The haematocrit fraction of each patient is obtained with an independent blood test.

ECV suffers the limitations of other quantitative techniques, including mis-registration between images acquired at significantly separate time points and breath-hold positions, which can lead to inaccuracy, however, this may be partially corrected for with the use of in-plane motion correction strategies and/or non-rigid registration algorithms [49]. Other issue of concern, in this case to both LGE and ECV techniques, is that the use of gadolinium-based contrast agents may be associated with an increased risk of nephrogenic systemic fibrosis in patients with pre-existing renal dysfunction [50], which partially can be addressed by using more stable cyclic chelates such as DOTA and by minimising the dose injected. Kanda *et al*. [51] has also recently reported gadolinium accumulation in the neural system associated with the use of some gadolinium-based contrast agents. Therefore, the development of quantitative or semi-quantitative gadolinium-free approaches for the assessment of myocardial fibrosis is of great interest.

Advanced native contrast techniques

T1-rho imaging

As described earlier, the T1 relaxation process involves the restoration of the thermal equilibrium magnetization by means of interactions between spins and non-excited atoms and molecules (lattice), while the magnetic moments precesses around the static magnetic field B_0 with frequency ω_0. As described too, the likelihood of such interactions increases when the thermally-induced vibrational and rotational motion of the molecules approaches ω_0. Consequently, the T1 relaxation constant of a given sample depends both on the structural characteristics of the lattice and the spin's resonant frequency, ω_0. In a clinical MRI scanner,

however, the magnitude of the external static magnetic field B_0 is fixed by the choice of the scanner used, therefore ω_0 is also fixed (since $\omega_0 = \gamma B_0$, where γ the gyromagnetic ratio is a constant that depends on fundamental characteristics of the nucleus). For this reason, the T1 contrast in a typical case of H+ (proton) imaging with a 1.5T scanner is given by the different tissues' ability to facilitate interactions at or around a given resonant frequency, i.e., ω_0=63.87MHz.

T1 measurements do not provide enough information to observe small differences between different types of solids and semi-solids, because their molecules typically vibrate and rotate at frequencies in the order of Hz or a few KHz, that is, at least 1000 times slower than λ=63.87MHz. In nuclear magnetic resonance (NMR) spectroscopy, B_0 can be cycled through a range of values and therefore a T1 'dispersion' or spectrum is obtained to better investigate proteins and other solids or semi-solids [52]. The variation of B_0 or field-cycling is difficult in large, super-conducting magnets such as those in most clinical scanners and therefore manufacturers do not provide this feature. T1-ρ experiments are an approach to measure the T1 dispersion in clinical scanners using the ability to vary the amplitude of the rotating magnetic field B_1 instead.

In a T1-ρ experiment, an RF pulse parallel to the rotating transverse magnetization may be applied during the time between excitation and signal acquisition. The pulse is called spin-lock (SL) because it acts as a static magnetic field $\vec{B}_{SL}$ in the spins' rotating frame, therefore generating a secondary precession of the magnetic moment around $\vec{B}_{SL}$ with frequency $\omega_{SL} = \gamma B_{SL}$. An example T1-rho weighted sequence is shown in **Figure 2-7**. The decay of transverse magnetization during the SL pulse is due to spin-lattice interactions, while dephasing caused by spin-spin interactions is compensated by the continuous SL feed. The time constant of the exponential decay of the transverse magnetization in this scheme, $T_1\rho$, gives us

information about the spin's ability to interact at the chosen ω_{SL}. The amplitude of the SL pulse determines ω_{SL} and may be easily varied using standard amplifiers to achieve any frequency between hundreds of Hz and a few KHz.

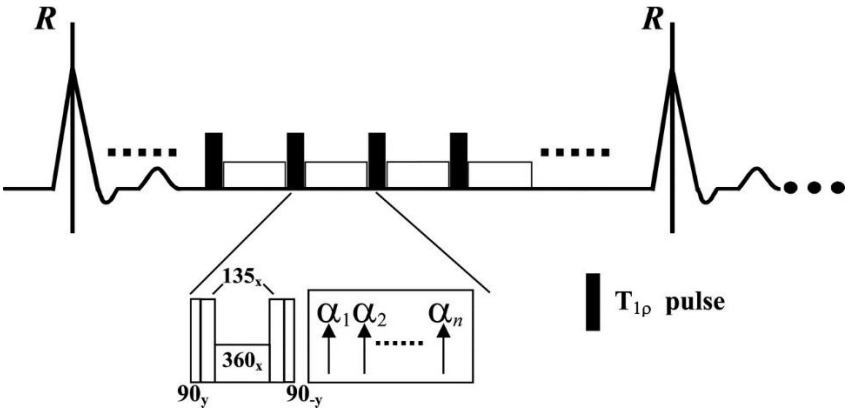

***Figure 2-7**. Pulse diagram of a $T_1\rho$-weighted segmented cardiac cine sequence. The spin-locking preparation consists of a composite $90_y - 360_x - 90_{-y}$ pulse while the image is acquired in segments $\alpha_1$to α_n. The 360_x pulse is the spin locking pulse while 90_y and 90_{-y} are the tip-down and tip-up pulses, respectively. Figure obtained from Muthupillai et al. [53].*

In $T_1\rho$ mapping of biological systems, typically, a series of images *I* are collected with different SL preparation times (TSL) and fitted to a mono-exponential decay model [54]:

$$I(TSL) = I(0)\, e^{TSL/T_1\rho} \tag{2-5}$$

$T_1\rho$ mapping has been used to assess cartilage degeneration due to its sensitivity to proteoglycans loss at ω_{SL} = 400-500 Hz [54, 55]. $T_1\rho$ has also been used for localization of myocardial edema [56], chronic myocardial scar [57] and hypertrophic cardiomyopathy [58]. Elevated values of $T_1\rho$ have been associated with myocardial oedema, which is likely related to the significant increase in water content. Hypertrophic cardiomyopathy and chronic myocardial scar are known to generate an elevated concentration of collagen in the extra-cellular matrix with respect to healthy myocardium, however, all studies to date have also found elevated $T_1\rho$ values. Witschley *et al.* [59] has also found that higher than typical ω_{SL} (>

2 KHz) produces stronger contrast between remote myocardium and collagenous scar, in a swine model of chronic myocardial infarction.

Some of the limitations that have prevented widespread adoption of $T_1\rho$ contrast (and mapping) techniques in clinical practise include, but are not limited to, strong dependence to B1 and B0 homogeneity, energy/SAR intensiveness because of the long SL pulses (typically up to 50 ms), RF power limitations, complexity of parameter setup e.g. choice of ω_{SL}, and quantification of $T_1\rho$ confounded by the inherent contrast (T1 & T2) of the imaging acquisition module.

Magnetization transfer

Molecular interpretation

Solid or semi-solid structures in tissue are often made of clusters or arrays of large macromolecules such as proteins. As described earlier, these macromolecules have low rotational and vibrational frequency, mostly because of their size, which entails typically long T1 relaxation times. On the other hand, H+ spins bound to the macromolecules have very efficient interactions with neighbouring spins due to higher density and restricted translational motion, which translates into very short T2 relaxation times making direct proton imaging of macromolecules very challenging unless ultra-short echo time sequences are used. Protein-rich tissue such as cartilage, white matter or muscle have been found to have T2 relaxation times in the order of 15-60 ms [60-62]. But these complex tissues often have multiple components of T2 decay [63, 64], representative of the different structures they are made of. Adler *et al.* [65] showed that a two or three compartment model may explain T2 decay in fibrocartilage and hyaline cartilage, respectively, with the shortest T2 components (in both cases) in the order of ~12-14 microseconds. The extremely short component is associated with the collagen fibres that create the core structure of the extracellular matrix.

Signals which decay in a timeframe of tens or hundreds of microseconds are typically invisible to MRI, where an echo time (TE) below 1 or 2 milliseconds is impractical to achieve. But this doesn't mean that their energy is completely lost. The excited (transverse) magnetization within macromolecules has a very short lifespan, however, individual macromolecule-bound spins may interact or even exchange places with free water spins if they come close enough. Once it reaches a different molecular environment, the acquired transverse magnetization may just live long enough to make it into the MRI signal. This effect is called Magnetization Transfer (MT).

MT was first demonstrated to occur in kidney and skeletal muscle by Wolff and Balaban [66]. They showed a signal loss in free water protons after selectively saturating only the macromolecule-bound protons with an off-resonance Continuous Wave (CW) pulse. The signal decrease is explained by an exchange of magnetization between the protons with restricted motion (bound pool) and the water protons (free pool). The exchange happens via two main processes: dipolar coupling between bound and free water protons or chemical exchange. The characteristics of the exchange are determined by the tissue composition, including the size and distribution of its macromolecular components.

CW experiments apply an off-resonance preparation pulse to selectively saturate the bound pool, because of its wide or 'flattened' line absorption shape (as in a scheme in **Figure 2-8**). The preparation pulse is long and has constant amplitude to achieve full and steady state saturation. However, this approach is power intensive and difficult to apply in-vivo with high-resolution protocols. Alternatively, a train of shaped and shorter off-resonance preparation pulses, often called pulsed MT, is more popular in human *in-vivo* studies.

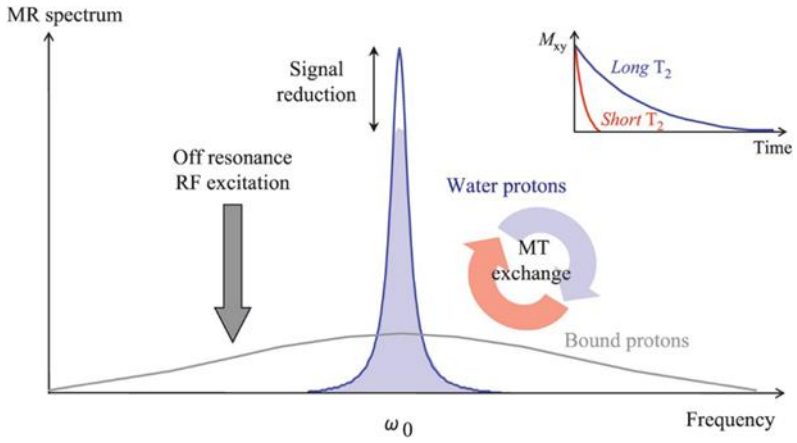

***Figure 2-8**. Scheme of the line absorption shape of Free Water protons (blue) vs. Macromolecule-bound protons (grey). An off-resonance MT pulse can saturate the bound pool without affecting the water pool because the extremely short T2 of bound protons defines a wide and flattened line absorption shape that resonates far beyond the Larmor frequency. MT exchange between bound pool protons and free water protons then leads to a reduction of the water signal, which can be observed with proton imaging.*

Common clinical applications

A major clinical application of MT contrast has been to suppress signal coming from protein-rich (short T2) tissue, such as muscle. For example, MT effect can generate good contrast between myocardium and blood irrespective of blood oxygenation and therefore can improve cardiac vein visualization [67, 68]. While T2 preparation is known to be useful in coronary angiography [69], the large reduction in T2 of deoxygenated blood causes difficulty in coronary vein imaging. On the other hand, MT preparation is largely independent of the magnetic susceptibility effect that causes T2 reduction in venous blood and has been shown to generate a contrast enhancement that is superior to T2 based approaches in the cardiac veins [68].

The magnetization transfer ratio (MTR) is a widely used semi-quantitative approach to MT contrast. The MTR method comprises two sets of images, one with MT preparation and one without it, and the calculation of the percentage difference or ratio between them. MTR has

been mostly used to study white matter integrity in the brain, where a reduction in myelin content has been shown to correlate with reduced MTR values [70]. However, some studies have found that MTR is also affected by changes in the water content associated to inflammation or oedema [71]. Its widespread use in brain studies does not compare to its use in cardiac applications, perhaps because of concerns with misregistration artefacts and the length of the acquisition protocols. Nevertheless, a few cardiac studies have been published over the last 20 years, such as a post-mortem study which showed a correlation between MTR reduction and areas of oedematous or granulocyte-infiltrated tissue by histology [72], in patients with acute myocardial infarction (MI). A breath-held 2D cine steady state technique has also shown reduced MTR values associated with LGE enhancement in acute MI patients [73]. But breath-holding can be difficult in sick patients, where the length of breath-hold may limit the spatial resolution and different breath-hold positions may lead to misregistration artefacts between slices. Germain *et al.* [74] recently proposed a 1D-navigated free-breathing on-resonance (bSSFP) MT approach, where they show some agreement between LGE enhancement and reduced MT effects in patients with acute or recent MI. However, partial volume effects and likely residual motion may have caused significant intra and inter subject variability. Moreover, MTR represents a complex interplay of physiological and experimental parameters, which can be difficult to link to an specific pathology [75].

Quantitative magnetization transfer

Multiple models to explain the MT signal have been proposed over the years [65, 75, 76], with the spin-bath exchange model being the most widely used. The spin-bath exchange model considers two different compartments, namely the bound protons (B) and the free water protons (A), where the former are only a small fraction of the latter. The two compartments can exchange magnetization from B to A and from A to B. The exchange rates are proportional to the equilibrium magnetization of the target compartment. The evolution of the total

magnetization of the bound and free water protons can be characterized by a set of differential equation (see Chapter 3), which include the exchange parameters between the longitudinal magnetization of the two compartments. The transverse magnetization of the free water protons is given by their T2 rate and the frequency and amplitude of the RF excitation pulse. The transverse magnetization of the bound protons is negligible due to its extremely short T2, therefore the overall effect of the RF pulse over the bound pool magnetization is a saturation of the longitudinal magnetization at rate which, among others, depends on the amplitude of the RF pulse and the line absorption shape of the bound spins.

It is important to note that the signal evolution equations for a quantitative MT experiment depend on the choice of selective saturation method. The off-resonance saturation method described above is the most widely used, however, other methods such binomial composite (on-resonance) preparation [77] or optimized bSSFP strategies [78] exist. In this work, only the off-resonance saturation method was used and the mathematical interpretations described in Chapter 2 and Chapter 3 consider only this case.

In terms of clinical applications, quantitative MT studies have been used to characterize pathological changes associated with multiple sclerosis in the macromolecular content in brain [79]. More specifically, the pool size ratio (PSR) or M_0^B/M_0^A is often used as a marker of protein or macromolecular content [78, 80, 81]. The forwards exchange rate $k_f = RM_0^B$, which is also proportional to the bound pool equilibrium magnetization has been shown to reduce in chronic and acute infarct with respect to normal myocardium in rats [82]. Mapping of PSR and/or the forward exchange have been proposed as candidates for non-contrast assessment of myocardial fibrosis before [25].

REFERENCES

1. Ho, J.E., et al., *Galectin-3, a marker of cardiac fibrosis, predicts incident heart failure in the community.* J Am Coll Cardiol, 2012. **60**(14): p. 1249-56.
2. Mewton, N., et al., *Assessment of myocardial fibrosis with cardiovascular magnetic resonance.* J Am Coll Cardiol, 2011. **57**(8): p. 891-903.
3. de Jong, S., et al., *Fibrosis and cardiac arrhythmias.* J Cardiovasc Pharmacol, 2011. **57**(6): p. 630-8.
4. Cowling, R.T., et al., *Mechanisms of cardiac collagen deposition in experimental models and human disease.* Transl Res, 2019.
5. Souders, C.A., S.L. Bowers, and T.A. Baudino, *Cardiac fibroblast: the renaissance cell.* Circ Res, 2009. **105**(12): p. 1164-76.
6. Porter, K.E. and N.A. Turner, *Cardiac fibroblasts: at the heart of myocardial remodeling.* Pharmacol Ther, 2009. **123**(2): p. 255-78.
7. Manabe, I., T. Shindo, and R. Nagai, *Gene expression in fibroblasts and fibrosis: involvement in cardiac hypertrophy.* Circ Res, 2002. **91**(12): p. 1103-13.
8. Weber, K.T., *Cardiac interstitium in health and disease: the fibrillar collagen network.* J Am Coll Cardiol, 1989. **13**(7): p. 1637-52.
9. Gunja-Smith, Z., et al., *Remodeling of human myocardial collagen in idiopathic dilated cardiomyopathy. Role of metalloproteinases and pyridinoline cross-links.* Am J Pathol, 1996. **148**(5): p. 1639-48.
10. Doering, C.W., et al., *Collagen network remodelling and diastolic stiffness of the rat left ventricle with pressure overload hypertrophy.* Cardiovasc Res, 1988. **22**(10): p. 686-95.
11. Rohr, S., *Myofibroblasts in diseased hearts: new players in cardiac arrhythmias?* Heart Rhythm, 2009. **6**(6): p. 848-56.
12. Kong, P., P. Christia, and N.G. Frangogiannis, *The pathogenesis of cardiac fibrosis.* Cell Mol Life Sci, 2014. **71**(4): p. 549-74.
13. Kai, H., et al., *Diastolic dysfunction in hypertensive hearts: roles of perivascular inflammation and reactive myocardial fibrosis.* Hypertens Res, 2005. **28**(6): p. 483-90.
14. Berk, B.C., K. Fujiwara, and S. Lehoux, *ECM remodeling in hypertensive heart disease.* J Clin Invest, 2007. **117**(3): p. 568-75.
15. Messroghli, D.R., et al., *Modified Look-Locker inversion recovery (MOLLI) for high-resolution T1 mapping of the heart.* Magn Reson Med, 2004. **52**(1): p. 141-6.
16. Look, D.C. and D.R. Locker, *Time Saving in Measurement of NMR and EPR Relaxation Times.* Review of Scientific Instruments, 1970. **41**(2): p. 250-251.
17. Deichmann, R. and A. Haase, *Quantification of T1 values by SNAPSHOT-FLASH NMR imaging.* Journal of Magnetic Resonance (1969), 1992. **96**(3): p. 608-612.
18. Lin, Y.J. and A.P. Koretsky, *Manganese ion enhances T1-weighted MRI during brain activation: an approach to direct imaging of brain function.* Magn Reson Med, 1997. **38**(3): p. 378-88.
19. van Walderveen, M.A., et al., *Histopathologic correlate of hypointense lesions on T1-weighted spin-echo MRI in multiple sclerosis.* Neurology, 1998. **50**(5): p. 1282-8.
20. Vrenken, H., et al., *Whole-brain T1 mapping in multiple sclerosis: global changes of normal-appearing gray and white matter.* Radiology, 2006. **240**(3): p. 811-20.
21. Dall'Armellina, E., et al., *Cardiovascular magnetic resonance by non contrast T1-mapping allows assessment of severity of injury in acute myocardial infarction.* J Cardiovasc Magn Reson, 2012. **14**: p. 15.

22. Ferreira, V.M., et al., *Non-contrast T1-mapping detects acute myocardial edema with high diagnostic accuracy: a comparison to T2-weighted cardiovascular magnetic resonance.* J Cardiovasc Magn Reson, 2012. **14**: p. 42.
23. Messroghli, D.R., et al., *Myocardial T1 mapping: application to patients with acute and chronic myocardial infarction.* Magn Reson Med, 2007. **58**(1): p. 34-40.
24. Puntmann, V.O., et al., *Native T1 mapping in differentiation of normal myocardium from diffuse disease in hypertrophic and dilated cardiomyopathy.* JACC Cardiovasc Imaging, 2013. **6**(4): p. 475-84.
25. van Oorschot, J.W., et al., *Endogenous contrast MRI of cardiac fibrosis: beyond late gadolinium enhancement.* J Magn Reson Imaging, 2015. **41**(5): p. 1181-9.
26. Roujol, S., et al., *Accuracy, precision, and reproducibility of four T1 mapping sequences: a head-to-head comparison of MOLLI, ShMOLLI, SASHA, and SAPPHIRE.* Radiology, 2014. **272**(3): p. 683-9.
27. Bloch, F., *Nuclear induction.* Physical review, 1946. **70**(7-8): p. 460.
28. Haase, A., *Snapshot FLASH MRI. Applications to T1, T2, and chemical-shift imaging.* Magn Reson Med, 1990. **13**(1): p. 77-89.
29. Coolen, B.F., et al., *Quantitative T2 mapping of the mouse heart by segmented MLEV phase-cycled T2 preparation.* Magn Reson Med, 2014. **72**(2): p. 409-17.
30. Nighoghossian, N., et al., *Old microbleeds are a potential risk factor for cerebral bleeding after ischemic stroke: a gradient-echo T2*-weighted brain MRI study.* Stroke, 2002. **33**(3): p. 735-42.
31. Bredella, M.A., et al., *Accuracy of T2-weighted fast spin-echo MR imaging with fat saturation in detecting cartilage defects in the knee: comparison with arthroscopy in 130 patients.* AJR Am J Roentgenol, 1999. **172**(4): p. 1073-80.
32. Toussaint, J.F., et al., *T2-weighted contrast for NMR characterization of human atherosclerosis.* Arterioscler Thromb Vasc Biol, 1995. **15**(10): p. 1533-42.
33. Abdel-Aty, H., O. Simonetti, and M.G. Friedrich, *T2-weighted cardiovascular magnetic resonance imaging.* J Magn Reson Imaging, 2007. **26**(3): p. 452-9.
34. Higgins, C.B., et al., *Nuclear magnetic resonance imaging of acute myocardial infarction in dogs: alterations in magnetic relaxation times.* Am J Cardiol, 1983. **52**(1): p. 184-8.
35. Ugander, M., et al., *Myocardial edema as detected by pre-contrast T1 and T2 CMR delineates area at risk associated with acute myocardial infarction.* JACC Cardiovasc Imaging, 2012. **5**(6): p. 596-603.
36. Zia, M.I., et al., *Characterizing myocardial edema and hemorrhage using quantitative T2 and T2* mapping at multiple time intervals post ST-segment elevation myocardial infarction.* Circ Cardiovasc Imaging, 2012. **5**(5): p. 566-72.
37. Giri, S., et al., *T2 quantification for improved detection of myocardial edema.* J Cardiovasc Magn Reson, 2009. **11**: p. 56.
38. Wassmuth, R., et al., *Variability and homogeneity of cardiovascular magnetic resonance myocardial T2-mapping in volunteers compared to patients with edema.* J Cardiovasc Magn Reson, 2013. **15**: p. 27.
39. Flett, A.S., et al., *Evaluation of techniques for the quantification of myocardial scar of differing etiology using cardiac magnetic resonance.* JACC Cardiovasc Imaging, 2011. **4**(2): p. 150-6.
40. Weinmann, H.J., et al., *Characteristics of gadolinium-DTPA complex: a potential NMR contrast agent.* AJR Am J Roentgenol, 1984. **142**(3): p. 619-24.
41. Sherry, A.D., W.P. Cacheris, and K.T. Kuan, *Stability constants for Gd3+ binding to model DTPA-conjugates and DTPA-proteins: implications for their use as magnetic resonance contrast agents.* Magn Reson Med, 1988. **8**(2): p. 180-90.

42. Rehr, R.B., et al., *Improved in vivo magnetic resonance imaging of acute myocardial infarction after intravenous paramagnetic contrast agent administration.* Am J Cardiol, 1986. **57**(10): p. 864-8.
43. de Roos, A., et al., *MR imaging of acute myocardial infarction: value of Gd-DTPA.* AJR Am J Roentgenol, 1988. **150**(3): p. 531-4.
44. Doltra, A., et al., *Emerging concepts for myocardial late gadolinium enhancement MRI.* Curr Cardiol Rev, 2013. **9**(3): p. 185-90.
45. Kim, R.J., et al., *Myocardial Gd-DTPA kinetics determine MRI contrast enhancement and reflect the extent and severity of myocardial injury after acute reperfused infarction.* Circulation, 1996. **94**(12): p. 3318-26.
46. Moon, J.C., et al., *Myocardial T1 mapping and extracellular volume quantification: a Society for Cardiovascular Magnetic Resonance (SCMR) and CMR Working Group of the European Society of Cardiology consensus statement.* J Cardiovasc Magn Reson, 2013. **15**: p. 92.
47. Fontana, M., et al., *Comparison of T1 mapping techniques for ECV quantification. Histological validation and reproducibility of ShMOLLI versus multibreath-hold T1 quantification equilibrium contrast CMR.* J Cardiovasc Magn Reson, 2012. **14**: p. 88.
48. Arheden, H., et al., *Measurement of the distribution volume of gadopentetate dimeglumine at echo-planar MR imaging to quantify myocardial infarction: comparison with 99mTc-DTPA autoradiography in rats.* Radiology, 1999. **211**(3): p. 698-708.
49. Kellman, P., et al., *Extracellular volume fraction mapping in the myocardium, part 1: evaluation of an automated method.* J Cardiovasc Magn Reson, 2012. **14**: p. 63.
50. Kuo, P.H., et al., *Gadolinium-based MR contrast agents and nephrogenic systemic fibrosis.* Radiology, 2007. **242**(3): p. 647-9.
51. Kanda, T., et al., *Gadolinium-based Contrast Agent Accumulates in the Brain Even in Subjects without Severe Renal Dysfunction: Evaluation of Autopsy Brain Specimens with Inductively Coupled Plasma Mass Spectroscopy.* Radiology, 2015. **276**(1): p. 228-32.
52. Kimmich, R. and E. Anoardo, *Field-cycling NMR relaxometry.* Progress in Nuclear Magnetic Resonance Spectroscopy, 2004. **44**(3): p. 257.
53. Muthupillai, R., et al., *Acute myocardial infarction: tissue characterization with T1rho-weighted MR imaging--initial experience.* Radiology, 2004. **232**(2): p. 606-10.
54. Wheaton, A.J., et al., *Quantification of cartilage biomechanical and biochemical properties via T1rho magnetic resonance imaging.* Magn Reson Med, 2005. **54**(5): p. 1087-93.
55. Rakhra, K.S., et al., *Can T1-rho MRI detect acetabular cartilage degeneration in femoroacetabular impingement?: a pilot study.* J Bone Joint Surg Br, 2012. **94**(9): p. 1187-92.
56. Stoffers, R.H., et al., *Assessment of myocardial injury after reperfused infarction by T1rho cardiovascular magnetic resonance.* J Cardiovasc Magn Reson, 2017. **19**(1): p. 17.
57. Witschey, W.R., et al., *In vivo chronic myocardial infarction characterization by spin locked cardiovascular magnetic resonance.* J Cardiovasc Magn Reson, 2012. **14**: p. 37.
58. Wang, C., et al., *Endogenous contrast T1rho cardiac magnetic resonance for myocardial fibrosis in hypertrophic cardiomyopathy patients.* J Cardiol, 2015. **66**(6): p. 520-6.

59. Witschey, W.R., et al., *Rotating frame spin lattice relaxation in a swine model of chronic, left ventricular myocardial infarction.* Magn Reson Med, 2010. **64**(5): p. 1453-60.
60. Maier, C.F., et al., *T2 quantitation of articular cartilage at 1.5 T.* J Magn Reson Imaging, 2003. **17**(3): p. 358-64.
61. Huang, T.Y., et al., *T2 measurement of the human myocardium using a T2-prepared transient-state TrueFISP sequence.* Magn Reson Med, 2007. **57**(5): p. 960-6.
62. Deoni, S.C.L., et al., *Standardized structural magnetic resonance imaging in multicentre studies using quantitative T1 and T2 imaging at 1.5 T.* Neuroimage, 2008. **40**(2): p. 662-671.
63. Wang, N. and Y. Xia, *Dependencies of multi-component T2 and T1rho relaxation on the anisotropy of collagen fibrils in bovine nasal cartilage.* J Magn Reson, 2011. **212**(1): p. 124-32.
64. Saab, G., R.T. Thompson, and G.D. Marsh, *Multicomponent T2 relaxation of in vivo skeletal muscle.* Magn Reson Med, 1999. **42**(1): p. 150-7.
65. Adler, R.S., S.D. Swanson, and H.N. Yeung, *A three-component model for magnetization transfer. Solution by projection-operator technique, and application to cartilage.* J Magn Reson B, 1996. **110**(1): p. 1-8.
66. Wolff, S.D. and R.S. Balaban, *Magnetization transfer contrast (MTC) and tissue water proton relaxation in vivo.* Magn Reson Med, 1989. **10**(1): p. 135-44.
67. Nezafat, R., et al., *Coronary magnetic resonance vein imaging: imaging contrast, sequence, and timing.* Magn Reson Med, 2007. **58**(6): p. 1196-206.
68. Ginami, G., et al., *Non-contrast enhanced simultaneous 3D whole-heart bright-blood pulmonary veins visualization and black-blood quantification of atrial wall thickness.* Magn Reson Med, 2019. **81**(2): p. 1066-1079.
69. Botnar, R.M., et al., *Improved coronary artery definition with T2-weighted, free-breathing, three-dimensional coronary MRA.* Circulation, 1999. **99**(24): p. 3139-48.
70. Schmierer, K., et al., *Magnetization transfer ratio and myelin in postmortem multiple sclerosis brain.* Ann Neurol, 2004. **56**(3): p. 407-15.
71. Vavasour, I.M., et al., *Is the magnetization transfer ratio a marker for myelin in multiple sclerosis?* J Magn Reson Imaging, 2011. **33**(3): p. 713-8.
72. Crooijmans, H.J., et al., *Cardiovascular magnetization transfer ratio imaging compared with histology: a postmortem study.* J Magn Reson Imaging, 2014. **40**(4): p. 915-9.
73. Weber, O.M., et al., *Assessment of magnetization transfer effects in myocardial tissue using balanced steady-state free precession (bSSFP) cine MRI.* Magn Reson Med, 2009. **62**(3): p. 699-705.
74. Germain, P., et al., *A dual flip angle 3D bSSFP magnetization transfer-like method to differentiate between recent and old myocardial infarction.* J Magn Reson Imaging, 2018. **47**(3): p. 798-808.
75. Henkelman, R.M., et al., *Quantitative interpretation of magnetization transfer.* Magn Reson Med, 1993. **29**(6): p. 759-66.
76. Gochberg, D.F. and J.C. Gore, *Quantitative magnetization transfer imaging via selective inversion recovery with short repetition times.* Magn Reson Med, 2007. **57**(2): p. 437-41.
77. Stoeck, C.T., et al., *Optimization of on-resonant magnetization transfer contrast in coronary vein MRI.* Magn Reson Med, 2010. **64**(6): p. 1849-54.
78. Gloor, M., K. Scheffler, and O. Bieri, *Quantitative magnetization transfer imaging using balanced SSFP.* Magn Reson Med, 2008. **60**(3): p. 691-700.

79. Giulietti, G., et al., *Quantitative magnetization transfer provides information complementary to grey matter atrophy in Alzheimer's disease brains.* Neuroimage, 2012. **59**(2): p. 1114-22.
80. Li, W., et al., *Magnetization transfer imaging provides a quantitative measure of chondrogenic differentiation and tissue development.* Tissue Eng Part C Methods, 2010. **16**(6): p. 1407-15.
81. Li, K., et al., *A rapid approach for quantitative magnetization transfer imaging in thigh muscles using the pulsed saturation method.* Magn Reson Imaging, 2015. **33**(6): p. 709-17.
82. Scholz, T.D., et al., *Water-macromolecular proton magnetization transfer in infarcted myocardium: a method to enhance magnetic resonance image contrast.* Magn Reson Med, 1995. **33**(2): p. 178-84.

Chapter 3 : Signal Simulation Theory

Abstract

In this Chapter, the theoretical basis for MR signal simulations and modelling used in this work are described. First, basic concepts such as free-precession, relaxation, the rotating frame and flip angles are introduced. Then, the spin-bath exchange model for magnetization transfer is studied in detail and two main ways to solve it are discussed: the linear problem approach with Minimal Approximation Magnetization Transfer (MAMT), and the Extended Phase Graph Exchange MT (EPGX-MT) approach.

The free precession model

In 1946, Felix Bloch introduced a set of differential equations to describe the evolution of net (macroscopic) magnetization [1] as a result of the interaction of all spins N in a sample with net magnetic moment $\vec{M} = \sum_{i=1}^{N} \vec{\mu}_i$ and an external magnetic field $\vec{B}$. The model is based on the linear relationship between magnetic moment $\vec{M}$ and angular moment $\vec{L}$ in a magnetic dipole, i.e. a rotating charged particle.

An intuitive way to understand it is using the Ampere Law, where the magnetic moment of a charged particle is associated with the current loop that is created by its rotation and is proportional to both the current (I) and the loop area (A),

$\mu = I \times A$, or

$$\mu = \frac{q \times v}{2\pi r} \tag{3-1}$$

where q is the charge, v is the speed of rotation and r the radius of the loop. But a rotating particle also possess angular momentum, defined by its mass m, speed v and radius r,

$$L = m\, v\, r \tag{3-2}$$

So if we connect equations *(3-1)* and *(3-2)* we find:

$$\mu = \frac{q}{2m} L \tag{3-3}$$

In other words, a magnetic moment arises from the angular moment of a charged particle, which allows it to interact with other magnetic fields. The force exerted by an external magnetic field $\overrightarrow{B_0}$ at an angle θ to the magnetic dipole generates a torque τ,

$$\vec{\tau} = \vec{\mu} \times \overrightarrow{B_0} = |\mu| \cdot |B_0| \cdot \sin\theta \ \hat{n} \tag{3-4}$$

Where $\hat{n}$ is a unitary vector, normal to the plane that contains $\overrightarrow{B_0}$ and $\vec{\mu}$. A non-zero torque implicates a constant change of the angular moment and, in this case according to equation *(3-3)*, a corresponding change in the magnetic moment thus pointing in the direction of $\hat{n}$,

$$\frac{d\vec{L}}{dt} = \gamma \vec{L} \times \overrightarrow{B_0} \tag{3-5}$$

which leads to a precession of the magnetic moment around the external magnetic field with characteristic angular frequency ω, also called Larmor frequency for physicist Joseph Larmor:

$$\omega_0 = \gamma B_0 \tag{3-6}$$

Thus, the evolution of net the magnetization $\vec{M} = \sum_{i=1}^{N} \vec{\mu}_i$ of a sample using equations *(3-3)*, *(3-4)* and (*3-5*) can be described such that:

$$\frac{d\vec{M}}{dt} = \gamma \overrightarrow{M} \times \overrightarrow{B_0} \tag{3-7}$$

Now, if we choose the z-axis to be in the direction of the external static magnetic field $\overrightarrow{B_0} = B_0 \hat{z}$, we can express this system of differential equations as:

$$\frac{dM_x}{dt} = \gamma M_y \cdot B_0 \qquad (3\text{-}8)$$

$$\frac{dM_y}{dt} = -\gamma M_x \cdot B_0$$

$$\frac{dM_z}{dt} = 0$$

And solve using the initial conditions $\vec{M}_0 = [M_x^0, M_y^0, M_z^0]$,

$$M_z(t) = M_z^0 \qquad (3\text{-}9)$$

$$M_x(t) = M_x^0 \cos\omega t + M_y^0 \sin\omega t$$

$$M_y(t) = -M_x^0 \sin\omega t + M_y^0 \cos\omega t$$

So that M_z (or the longitudinal component) which points in the direction of $\overrightarrow{B_0}$ remains constant, while the transversal components $[M_x, M_y]$ harmonically oscillate at the Larmor frequency. This is called the free precession model.

The rotating frame and the flip angle

But the clever part of the NMR experiment is the resonance bit, which consists in disturbing the magnetization with a another (perpendicular) magnetic field, $\overrightarrow{B_1}(t)$, rotating at a frequency ω, for a short period of time. Depending on its amplitude, the $\overrightarrow{B_1}$ pulse has the effect of tipping at least part of the net longitudinal magnetization into the transverse plane or, in terms of the individual spins, it gives them the amount of energy necessary to 'jump' to the excited state (if $\omega = \omega_0 \rightarrow E = h\omega_0$). So if we add the new (time-dependent) magnetic field into equation (*3-5*) we obtain:

$$\frac{d\vec{M}}{dt} = \gamma \vec{M} \times \left(\vec{B}_0 + \vec{B}_1\right) \qquad (3\text{-}10)$$

$$\rightarrow \left(\vec{B}_0 + \vec{B}_1\right) = B(t) = B_1 \cos \omega t\, \hat{x} + B_1 \sin \omega t\, \hat{y} + B_0 \hat{z}$$

Moreover, we can expand the model even further if we consider the relaxation processes discussed in Chapter 2, such as the spin-to-lattice mono-exponential recovery with characteristic time constant T1 (equation 2.1 acting on the longitudinal component) and spin-to-spin mono-exponential decay with characteristic time constant T2 (equation 2.3, acting on the transverse components) such that:

$$\frac{dM_x}{dt} = \gamma \left(M_y B_0 + M_z B_1 \sin \omega t\right) - \frac{1}{T_2} M_x \tag{3-11}$$

$$\frac{dM_y}{dt} = \gamma \left(M_z B_1 \cos \omega t - M_x B_0\right) - \frac{1}{T_2} M_y$$

$$\frac{dM_z}{dt} = \gamma \left(M_x B_1 \sin \omega t - M_y B_1 \cos \omega t\right) - \frac{1}{T_1}(M_z - M_0)$$

With M_0 the equilibrium longitudinal magnetization.

However, the set of equations (*3-11*) is very difficult to solve. Instead, we can simplify it by changing to a frame of reference that keeps the magnetic field constant over time. This frame can have the same longitudinal (*z*) axis as before, however, its *x* and *y* axis must rotate in the transverse plane at the same frequency as $\vec{B}_1$. In this *rotating frame*, the transverse magnetization components can be changed for auxiliary variables,

$$M'_x \equiv M_x \cos \omega t - M_y \sin \omega t \tag{3-12}$$

$$M'_y \equiv M_y \cos \omega t + M_x \sin \omega t$$

So if we replace (*3-12*) and *(3-6)* in the set of equations (*3-11*) we obtain:

$$\frac{dM'_x}{dt} = (\omega_0 - \omega) M'_y - \frac{1}{T_2} M'_x \tag{3-13}$$

$$\frac{dM'_y}{dt} = (\omega_0 - \omega)M'_x + \omega_1 M_z - \frac{1}{T_2}M'_y$$

$$\frac{dM_z}{dt} = \omega_1 M'_y - \frac{1}{T_1}(M_z - M_0)$$

Where $\omega_1 = \gamma B_1$, i.e., the angular frequency of the precession induced by $\vec{B}_1$. If we consider B_1's rotating frequency (ω) equal to the Larmor frequency (ω_0), we see that the effect of $\vec{B}_1$ over the initial magnetization $\vec{M}'_0 = [M'^0_x, M'^0_y, M'^0_z]$ immediately after the end of the pulse ($t = T_{RF}$) is analogue to that of $\vec{B}_0$ in equation *(3-9), mutatis mutandi*:

$$M'_x(T_{RF}) = M^0_x \tag{3-14}$$

$$M'_y(T_{RF}) = M'^0_y \cos\omega_1 T_{RF} + M'^0_z \sin\omega_1 T_{RF}$$

$$M'_z(T_{RF}) = -M'^0_y \sin\omega_1 T_{RF} + M'^0_z \cos\omega_1 T_{RF}$$

. When the initial magnetization is aligned with the z axis, i.e., $\vec{M}'_0 = [0,0,M_0]$, the effect is a precession around the direction of the static field, now the *x* axis. Therefore, at the end of a $\vec{B}_1$ pulse with length $t = T_{RF}$ the result is $\vec{M}'_0 = [0, M_0 \sin\alpha, M_0 \cos\alpha]$, a rotation about *x* with angle $\alpha = \omega_1 T_{RF}$. This is often called the *flip angle*.

Spin-bath exchange model for Magnetization Transfer

The Bloch-McConnell equations

To model magnetization transfer effects we must expand the free-precession model even further. Recalling from Chapter 2, the spin-bath exchange model considers two different compartments for the magnetization, namely, the bound protons (B) and the free water protons (A), where the former are only a small fraction of the latter. The evolution of the total magnetization of the bound and free water protons during off-resonance excitation may then

be described by the Bloch-McConnel equations [2, 3]. First, the transverse magnetization of the free water protons (M_x^A, M_y^A) is determined by exponential decay T_2^A, precession due to the frequency offset ($\Delta = \omega_0/2\pi - \omega/2\pi$) and the flipped longitudinal magnetization:

$$\frac{\partial M_x^A}{\partial t} = -\frac{M_x^A}{T_2^A} - 2\pi\,\Delta\,M_y^A \tag{3-15}$$

$$\frac{\partial M_y^A}{\partial t} = -\frac{M_y^A}{T_2^A} + 2\pi\,\Delta\,M_x^A + \omega_1 M_z^A \tag{3-16}$$

On the other hand, the transverse magnetization of the bound protons is negligible due to its extremely short T2. The overall effect of the RF pulse over the bound pool magnetization is a saturation of the longitudinal magnetization M_z^B at a rate R_{rfb}, while both longitudinal components exchange magnetization at rates RM_0^A (also called k forward) or RM_0^B, which are proportional to the equilibrium magnetization of each pool M_0^A and M_0^B:

$$\frac{\partial M_z^A}{\partial t} = R_1^A(M_0^A - M_z^A) - RM_0^B M_z^A + RM_0^A M_z^B + \omega_1 M_y^A \tag{3-17}$$

$$\frac{\partial M_z^B}{\partial t} = R_1^B(M_0^B - M_z^B) + RM_0^B M_z^A - (RM_0^B + R_{rfb})M_z^B \tag{3-18}$$

The saturation rate R_{rfb} is proportional to the convolution of the power deposition (ω_1^2) and the bound pools' absorption rate profile or line absorption shape, $G(2\pi\,\Delta)$ [4]:

$$R_{rfb} = \pi\,\omega_1^2 * G(2\pi\,\Delta) \tag{3-19}$$

Where, due to extremely short T_2^B and long preparation pulses (>10ms), the convolution may be approximated by simple multiplication, that is, only if the bandwidth of the RF pulse is significantly smaller compared to the spread of the line absorption shape (e.g., $MT_{Bandwidth} \ll 1/T_2^B$).

The line absorption shape (G) of the bound pool is mainly determined by the characteristics of the translational motion of the spins. In liquids, motion is generally unrestricted and the transverse relaxation processes follow mono exponential decay, as described earlier. In this situation, the frequency domain of the solution to the Bloch equations follows a Lorentzian line shape, where the T_2 constant determines the width of the spectrum. On the other hand, rigid materials with zero net translational motion of spins in every direction are better modelled by a Gaussian line shape. Unfortunately, biological-like systems are often neither fully liquid nor fully rigid materials. Partially ordered or semi-solid materials such as lipids and white matter which have complex asymmetric translation motion, have been experimentally shown to fit a super-Lorentzian line absorption shape [5]. This accounts for a dipolar Hamiltonian which does not average to zero over time. The width of the super-Lorentzian is also characterized by T2 (T_2^B), and may be obtained as:

$$G(2\pi\Delta, T_2^B) = \sqrt{2/\pi}\; T_2^B \int_0^{\pi/2} \frac{e^{-2\frac{(2\pi\Delta\, T_2^B)^2}{(3cos^2\theta-1)^2}}}{|3cos^2\theta - 1|}\; sin\theta d\theta \qquad (3\text{-}20)$$

Where θ is the angle between the external magnetic field and the normal to the symmetry plane, as a partially ordered material.

If a steady state is achieved after a long constant-amplitude pulse, an analytical solution [3] to the set of differential equations *(3-15)* to *(3-18)* is known to determine the saturation of the longitudinal magnetization of the free pool due to magnetization transfer immediately after the end of the preparation pulse. However, constant amplitude pulses are typically too energy-intensive for *in vivo* protocols. Pulsed MT protocols consist of a long train of shaped (variable amplitude) pulses spaced along (no-RF) free-precession periods, which makes them friendlier to *in vivo* studies. In these cases, the set of differential equations may be solved approximating

the time-dependent amplitude $\omega_1(t)$ by a constant, e.g. the constant waveform power equivalent (CWPE) method proposed by Ramani *et al.* [6]:

$$CWPE = \sqrt{\frac{\int_0^T \omega_1^2(t)dt}{TR}} \tag{3-21}$$

where T is the length of each pulse and TR is the pulse repetition period, that is, the length of a single pulse in addition to the pause period between pulses.

However, such approximations of the pulses' shape may result in signal simulation inaccuracy, especially when using low off-resonance frequency (<1 kHz) and/or high flip angles (>700˚) [2]. Portnoy *et al.* has shown that a more accurate solution may be obtained using the Minimal Approximation Magnetization Transfer (MAMT) method which, in addition, does not require steady state conditions [2].

Minimal Approximation Magnetization Transfer Method

The described set of differential equations *(3-15)* to *(3-18)* may also be expressed in matrix form:

$$\frac{d\,M(t)}{dt} = \Lambda(t)M(t) + \beta M_0 \tag{3-22}$$

Where Λ and β are the coefficients matrices. When $\Lambda(t)$ is constant in time, the solution to equation *(3-22)* has a well-known double exponential form:

$$M(t) = e^{\Lambda t}M(t=0) + \Lambda^{-1}(e^{\Lambda t} - I)\beta M_0 \tag{3-23}$$

Where Λ^{-1} is the matrix inverse of Λ and I is the identity matrix.

However, when using amplitude shaped RF pulses (in pulsed MT), $\omega_1 = \omega_1(t)$ and therefore $\Lambda(t)$ is not a constant. The MAMT method uses the fact that equation *(3-23)* is still a valid solution to *(3-22)* for a period of time (δt) small enough that $\Lambda(\delta t)$ is approximately constant. The entire evolution of the magnetization $M(t)$ can then be computed by splitting the time-

dependent amplitude in n steps (with $\omega_1^i(\delta t_i) \rightarrow i = 1..n$) and solving *(3-22)* in a piece-wise manner, using the solution for each step as the initial conditions for the next equation.

The MAMT method is computationally intensive, since the number of *n* steps in a single 50ms shaped RF pulse can be up to 1000 in order to achieve reasonable accuracy [2]. Furthermore, the method cannot take advantage of parallel computing techniques, since by design each computation must take input from the previous one.

Magnetization Transfer with Extended Phase Graph Simulation

Another quantitative MT transient approach has been proposed recently, using Extended Phase Graphs (EPG) simulation. Crucially, the EPGX-MT method by Malik *et al*. [7] may require significantly less computation resources and time than the MAMT method.

The standard EPG framework studies a system's magnetization response in terms of its configuration states [8] , defined as Fourier transforms of the spatial magnetization components:

$$\tilde{F}_+(\boldsymbol{k}) = \int_V \left(M_x(r) + iM_y(r)\right) e^{-i\boldsymbol{k}r} d^3r \tag{3-24}$$

$$\tilde{F}_-(\boldsymbol{k}) = \int_V \left(M_x(r) - iM_y(r)\right) e^{-i\boldsymbol{k}r} d^3r \tag{3-25}$$

$$\tilde{Z}(\boldsymbol{k}) = \int_V M_z \; e^{-i\boldsymbol{k}r} d^3r \tag{3-26}$$

where $[\tilde{F}_+, \tilde{F}_-, \tilde{Z}]$ are the configuration states and $[M_x, M_y, M_z]$ are the traditional spatial components of the magnetization vector. In this space, the net magnetization dephasing caused by spatially-variant gradients over a large ensemble of spins (within a volume V) is uniquely described by **k**, making computation much more efficient. The interactions with RF pulses, gradients, and the effects of relaxation and exchange are all represented by simple matrix operators.

The EPGX-MT [7] method extends the classic framework to include a fourth configuration state, $\tilde{Z}_B$, associated with the longitudinal magnetization of the bound pool, $[\tilde{F}_+, \tilde{F}_-, \tilde{Z}_A, \tilde{Z}_B]^T$ with $\tilde{Z}_B = \int_V M_Z^B \; e^{-i\boldsymbol{k}\boldsymbol{r}} d^3r$ coupled to $\tilde{Z}_A$ via first order forward and backward exchange rates: k_f, k_b . Because the time scale of the decay of transverse magnetization in the bound pool is so short (<20μs), it is assumed to decay instantaneously and only the exchange between longitudinal magnetizations is considered into the model. Another consequence of this instantaneous decay is that for the bound pool, RF excitation can be totally described by an instant saturation of the longitudinal magnetization at a rate R_{rfb}, proportional to RF power deposition, ω_1^2, and the bound pool's line absorption profile, $G(2\pi\,\Delta)$, as described in equation *(3-19)*.

REFERENCES

1. Bloch, F., *Nuclear induction.* Physical review, 1946. **70**(7-8): p. 460.
2. Portnoy, S. and G.J. Stanisz, *Modeling pulsed magnetization transfer.* Magn Reson Med, 2007. **58**(1): p. 144-55.
3. Henkelman, R.M., et al., *Quantitative interpretation of magnetization transfer.* Magn Reson Med, 1993. **29**(6): p. 759-66.
4. Sled, J.G. and G.B. Pike, *Quantitative interpretation of magnetization transfer in spoiled gradient echo MRI sequences.* J Magn Reson, 2000. **145**(1): p. 24-36.
5. Morrison, C., G. Stanisz, and R.M. Henkelman, *Modeling magnetization transfer for biological-like systems using a semi-solid pool with a super-Lorentzian lineshape and dipolar reservoir.* J Magn Reson B, 1995. **108**(2): p. 103-13.
6. Ramani, A., et al., *Precise estimate of fundamental in-vivo MT parameters in human brain in clinically feasible times.* Magn Reson Imaging, 2002. **20**(10): p. 721-31.
7. Malik, S.J., R. Teixeira, and J.V. Hajnal, *Extended phase graph formalism for systems with magnetization transfer and exchange.* Magn Reson Med, 2018. **80**(2): p. 767-779.
8. Weigel, M., *Extended phase graphs: dephasing, RF pulses, and echoes - pure and simple.* J Magn Reson Imaging, 2015. **41**(2): p. 266-95.

Chapter 4 Imaging Challenges of Cardiac Magnetic Resonance

Abstract

This chapter is about the imaging part in cardiac MRI. More specifically, the issue of respiratory motion and the need for accelerated image acquisition schemes in cardiac MRI. The basic concepts to understand the challenges posed by motion and accelerated acquisition in the MR image reconstruction problem are discussed, including spatial encoding and the Fourier Transformation. Some of the image reconstruction techniques currently used in cardiac MR are also described, including parallel imaging, sparsity and low-rank based methods, with special emphasis on a promising new technique exploiting local, non-local and contrast redundancies that can achieve high acceleration factors. Finally, rigid and non-rigid body models for motion correction in cardiac MRI are studied in detail.

Spatial encoding

As described in the previous chapter, the NMR experiment may provide an idea of the physical and chemical components of a sample by probing its magnetic relaxation properties. The time evolution and spectrum of the signal coming from a homogeneous sample may be analysed to infer information about microscopic properties of the sample such as contribution or presence of certain chemical populations and lattice characteristics. But if the size of the sample is large compared to the precision of the information, i.e., the sample is not microscopic, the inference may be flawed. If the large sample is anything but perfectly homogenous a confounding factor associated with the spatial distribution is introduced.

In MRI, a large heterogeneous sample is not an anomaly but the norm. Typically, the sample is either an entire patient or a large part of their body and thus the signal is inherently integrated from a diversity of microscopic and macroscopic biological structures. In order to overcome

this limitation, spatial information must be encoded into the signal so that a map of the spatial distribution of the microscopic properties can be created. This is the *imaging* bit in MRI.

Slice selection

In classic two-dimensional MRI, slice selection is the first of three spatial encoding steps. A 'slice' or 'cut' through the sample is selected by modifying the external static magnetic field using an array of coils enclosed within the main magnet. The coils are turned on to create a linearly varying spatial distribution of $\vec{B}_0 \rightarrow \vec{B}_0(\vec{r})$ so that its *gradient* points in a single direction. The resonance frequency, which depends on $\vec{B}_0$ (see equation *(3-6)*), acquires the same spatial distribution, $\omega_0 \rightarrow \omega_0(\vec{r})$ and therefore only the spins at a given position $r_0 \pm \Delta$ along the gradient direction are able to resonate with an excitation pulse of frequency ω_{RF} and bandwidth δ, where $r_0 \pm \Delta$ is determined by $\omega_0(r_0 \pm \Delta) = \omega_{RF} \pm \delta/2$. As a result, the collected signal comes only from a thin *slice* or 'cut through' the sample, made up of all the spins at position $\vec{r} \approx r_0 \pm \Delta$ and appropriately selected by modifying the strength and direction of the $\vec{B}_0$ gradient.

Frequency and Phase encoding

After slice selection, the three-dimensional sample can be considered approximately two-dimensional, therefore two more (linearly independent) spatial information data points are required for full spatial localisation. This can be done efficiently by using the complex nature of the collected signal, which consists of a voltage induced in receiver coils by the time-varying transverse magnetization. This effect is explained by the Maxwell-Faraday equation (from classical electromagnetism) which states that the work per unit charge (or voltage) done by the electric field ($\vec{E}$) that is required to move a charge around a close loop (Σ) is equal to the negative magnetic flux through the loop's surface:

$$\oint_{\Sigma} \vec{E}\, dl = -\frac{d}{dt}\iint_{\Sigma} \vec{B}\, dS \tag{4-1}$$

This means that the collected signal preserves the frequency, phase and amplitude of the rate of change of the magnetic flux which originates it. The amplitude is proportional to the number of spins that make up the signal and thus constitutes the actual spin (or most commonly proton) distribution we are most interested in. The signal's two other degrees of freedom, i.e., the frequency and phase, can therefore be used to encode the two spatial information bits which are needed.

The evolution of the transverse magnetization vector of a single spin over time may be expressed in a generic complex form, associated with its circularly rotating motion,

$$\vec{M}(t) = M_0\, e^{i(\omega_0 t + \phi)} \tag{4-2}$$

where M_0 is the magnitude of the vector, ω_0 is the frequency of the rotation and ϕ is the phase. In this notation, the MRI's direct measurement of a signal S from a slice U in the x-y plane is given by:

$$S(t) = \iint_{U} M_0(x,y)\, e^{i(\omega_0 t + \phi)} dx\, dy \tag{4-3}$$

where $M_0(x,y)$ is the spatial distribution of spins (or spin probability density), that is, our target measurement. The clever way to obtain $M_0(x,y)$ from $S(t)$ is to observe that equation (*4-3*) looks a little bit like a two-dimensional Fourier Transform (FT), which is the representation of a signal (any signal) by the weighted sum of the infinite harmonics of which is composed. In a single dimension,

$$\tilde{f}(k) = \int_{-\infty}^{\infty} f(x) e^{-2i\pi kx} dx \tag{4-4}$$

where $\tilde{f}(k)$ is the FT of $f(x)$, for any real number k. In two dimensions, a second degree of freedom is introduced in k, with $k \to k_x, k_y$:

$$\tilde{f}(k_x, k_y) = \iint_U f(x,y)\, e^{2i\pi(k_x x + k_y y)} dx\, dy \tag{4-5}$$

or,

$$\tilde{f}(k_x, k_y) = C \iint_U f(x,y)\, e^{i(k_x x + k_y y)} dx\, dy$$

and correspondingly, the inverse FT is

$$f(x,y) = \tilde{C} \int_{-\infty}^{\infty} \tilde{f}(k_x, k_y) e^{i(x k_x + y k_y)} dk_x\, dk_y \tag{4-6}$$

Where $\tilde{C}$ and C are arbitrary constants. Thus, from equations *(4-3)* and *(4-5)*, we can obtain $M_0(x,y)$ via FT if (and only if) we can collect the data for all k_x and k_y such that equation *(4-3)* term in brackets, $\Delta \equiv (\omega_0 t + \phi)$, is a linear function of x and y with coefficients k_x and k_y.

The first step to collect k-space (i.e. all of k_x and k_y) is called *frequency* encoding and consists of turning on another linear gradient such that $B_0 \to (B_0 + G_x x)$ where G_x is the gradient 'strength' coefficient, this time along a direction within the slice plane (e.g. the x axis) and *during* the signal acquisition. The Larmor frequency acquires a linearly variant spatial distribution along said direction with,

$$\omega_0(x) = \gamma G_x x + \gamma B_0 \tag{4-7}$$

$$\therefore \Delta = \gamma G_x x t + \gamma B_0 t + \phi$$

or

$$\Delta = k_x x + \Psi(t) + \phi \tag{4-8}$$

$$\rightarrow k_x \equiv \gamma G_x t$$

In this way, the signal is sampled over time t and thus along k_x while the gradient is on, relating spatial information to frequency content. After the sampling, the signal is demodulated and centred at zero frequency, removing the contribution from B_0 and therefore making Δ's other time dependent component, $\Psi(t)$, negligible.

The next spatial encoding uses the phase term ϕ to convey information about another (linearly independent) direction along the slice plane. This *phase* encoding is performed by turning on a linear gradient along said linearly independent direction (e.g. the y axis) after the excitation pulse and before the signal collection, for a limited period of time τ_y. The effect of a linear gradient applied during a free precession period is that the coherence acquired by the ensemble of spins during the excitation is gradually lost. This happens because the resonance frequency varies with spatial location and therefore the spins accumulate phase at different rates while the gradient is played out. For a fixed amount of time τ_y, the accumulated phase as a function of position along the gradient direction y with gradient strength coefficient G_y is

$$\phi(y) = \omega_0(y)\, \tau_y \tag{4-9}$$

and similar to equation (*4-7*),

$$\therefore \phi(y) = \gamma G_y y\, \tau_y$$

or,

$$\phi(y) = k_y y$$

$$\rightarrow k_y \equiv \gamma G_y\, \tau_y$$

Therefore, equation *(4-3)* can take the form of equation *(4-5)* if the steps of frequency and phase encoding are followed, allowing to recover the fully localised net magnetization/spin density function $M_0(x, y)$, i.e. the image, from the MRI signal through FT.

Sampling grid

The k-space is infinite yet it must be sampled during a finite, often very limited, amount of time. For this reason, a k-space sampling strategy must define truncation limits and a (maximum) resolution for each of its dimensions or degrees of freedom. The most widely used sampling strategies are typically Cartesian, which means that the axis of the samples' coordinates are perpendicular and therefore the sampling resolution is isotropic along each dimension. Because the samples are equally spaced, the collection of N samples (along each dimension) is treated as a Fourier series, wherein each sample is the coefficient of a complex sinusoid with a frequency associated to the k coordinate. The associated transformation, i.e. the discrete Fourier Transform (DFT), involves the inversion of a matrix of size N^2 and could be computationally expensive. But well-known fast Fourier Transform (FFT) algorithms which use the sparsity of the DFT matrix to factorize it into its main components can be significantly efficient and accurate [1]. Other non-uniform or non-Cartesian sampling strategies are often re-sampled (e.g. interpolated) into a Cartesian grid in order to apply FFT algorithms [2, 3].

Under-sampling

In Cartesian sampling, the frequency and phase encoding directions represent the k coordinated axes and are perpendicular to each other. But while the data points along the frequency encoding direction are obtained through a train of typically hundreds of samples during a single *echo*, the collection of a single phase encoding sample requires a full cycle of excitation, free precession and echo readout. This makes the length of MRI data acquisition to scale

significantly with the number of phase encoding steps, which may pose significant challenges associated with motion during the data acquisition. This motivates the use of reduced acquisition or under-sampling schemes, however, the properties of the FT also associate the truncation of k-space and/or reduction in the sampling resolution to a number of artefacts in the resulting image, including blurring and "wrapping up" or "folding" of structures (see **Figure 4-1**,for example). Due to these challenges, the following sections discuss several k-space under-sampling schemes joint with advanced image reconstruction models based on parallel imaging, sparsity condition and others, to accelerate the acquisition of data in MRI.

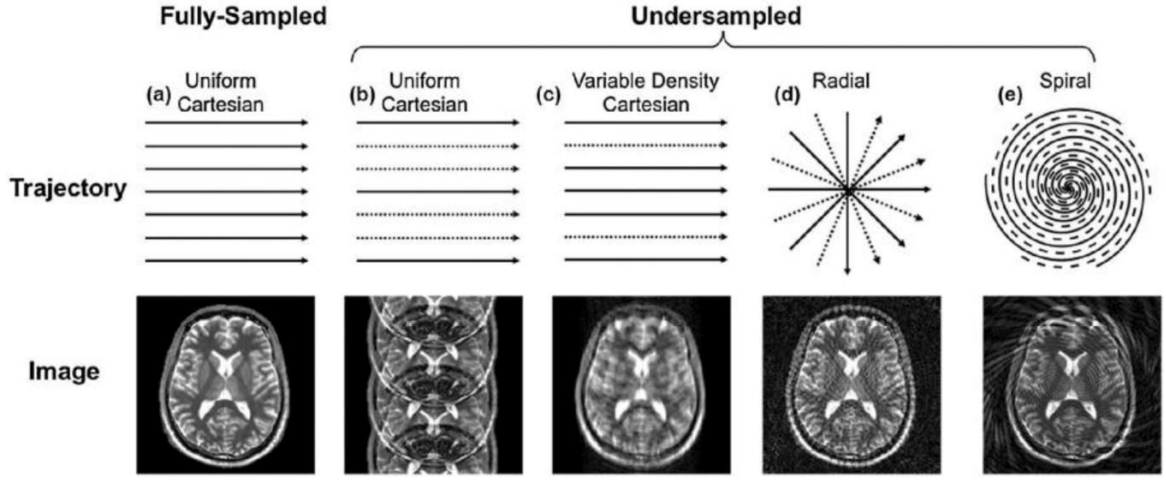

Figure 4-1*. Examples of corrupted images showing multiple artefacts including 'wrapping up' (see b), due to under-sampling with different acquisition trajectories.*

Sensitivity Encoding, SENSE

Multiple RF receiver coils can acquire data and images from the same sample simultaneously, therefore allowing the creation of a composite image with higher SNR at no cost in data acquisition time. Each single coil image, however, is weighted by a different coil sensitivity, which relates to the distance between the signal source and the centre of the coil (following the inverse square law). The obtained signal $S_j(t)$ for a given coil j relates to the net magnetization $M(\vec{r})$ over the volume V,

$$S_j(t) = \iiint_V M(\vec{r})\, c_j(\vec{r}) e^{-2i\pi \vec{k}(t)\vec{r}} d\vec{r} \tag{4-10}$$

With $c_j(\vec{r})$ the spatial distribution of coil j's sensitivity.

Parallel imaging techniques use the underlying spatial encoding from RF coils to replace spatial encoding that might be obtained from gradients i.e. missing or under-sampled k-space data. Sensitivity Encoding (SENSE) was proposed in 1999 [4] as a way to combine corrupted under-sampled coil images using the information from multiple coils to create one 'unwrapped' or artefact-free composite image.

In a typical two-dimensional Cartesian acquisition scheme, one line in k-space (along the readout dimension) is obtained with every echo. A regular under-sampling pattern such as one missing line every other line, that is, an effective reduction of the k-space resolution (in this case a factor of two) in the under-sampling dimension, will have the result of reducing the effective field of view in the image space. However, the sample coverage is only determined by the coil (or coil-array) size, therefore, the resulting image is corrupted or "wrapped up" inside an insufficient field of view (see **Figure 4-2**). This is a form of aliasing due to a violation of the Nyquist sampling theorem.

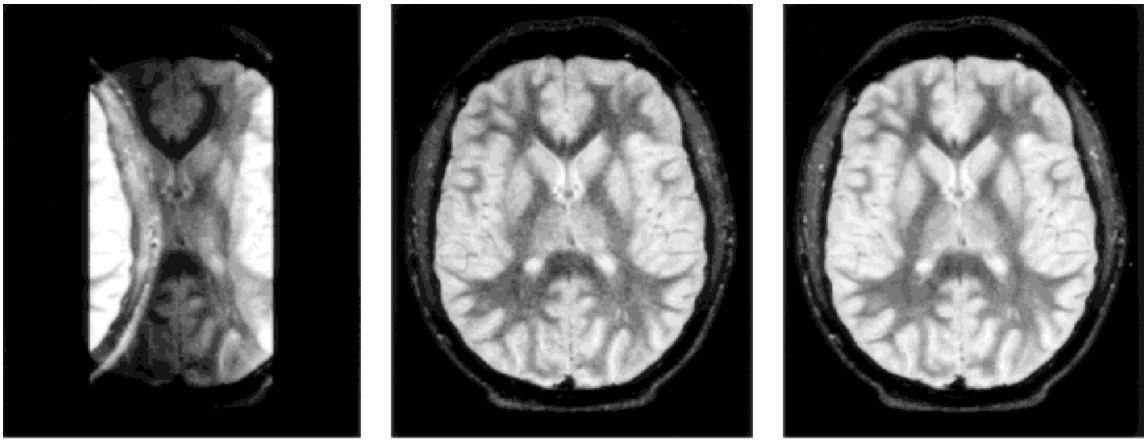

***Figure 4-2**. Turbo spin echo transverse images of healthy volunteer acquired with two coils. A) Reduction factor 2 (one missing line per every acquired line) and conventional sum-of-squares (single-coil) reconstruction. B) Reduction factor 2 and SENSE reconstruction. C) Reduction factor 1 (fully sampled, no reduction) and SENSE reconstruction. Figure obtained from Pruessmann et al. [4], copyright license order number **4677181454080** RightsLink / John Wiley and Sons.*

In an aliased image (i.e. the image that results from under-sampling in a regular pattern), each pixel is considered a linear combination or superposition of a number of pixels from the un-aliased image, i.e., the image that would arise from a fully sampled k-space. In the SENSE method, the weightings for each pixel are determined by each coil sensitivity while the number of pixels is given by the under-sampling factor. In other words, the key of the method is to solve the un-aliased pixels using each coil (aliased) image in a system of equations where the coil sensitivity weights are known (see a scheme in **Figure 4-3**). The number of (linearly independent) coils needed to solve the system of equations must therefore equate or surpass the under-sampling factor. For each single pixel in the aliased images, the matrix form of this system of equations is a linear transformation of vector $\vec{m}$, containing the signal values across each coil,

$$\vec{v} = U\,\vec{m} \tag{4-11}$$

with,

$$U \equiv (S^H \Psi^{-1} S)^{-1} S^H \Psi^{-1}$$

where $\vec{v}$ represents the solution or 'unwrapped' contributions of the superimposed signal pixels and U is the 'unfolding' matrix, determined by the sensitivity matrix S and the receiver noise matrix Ψ.

The sensitivity matrix consists of the coil sensitivity in each superimposed pixel and for each coil. The coil sensitivity maps may be estimated from reference data prior to image acquisition [4], or from the data itself, i.e., using auto-calibrated methods [5, 6]. For example, Pruessmann et al [4] proposed a way to obtain scaled coil sensitivity maps acquiring a lower resolution but full field of view (un-aliased) set of coil images, and then dividing each one of them by the sum of squares of the set. This creates intrinsically noisy maps (as previously observed in **Figure 4-2B**) but since the coil sensitivity varies smoothly a de-noising strategy such as local polynomial fitting may be applied.

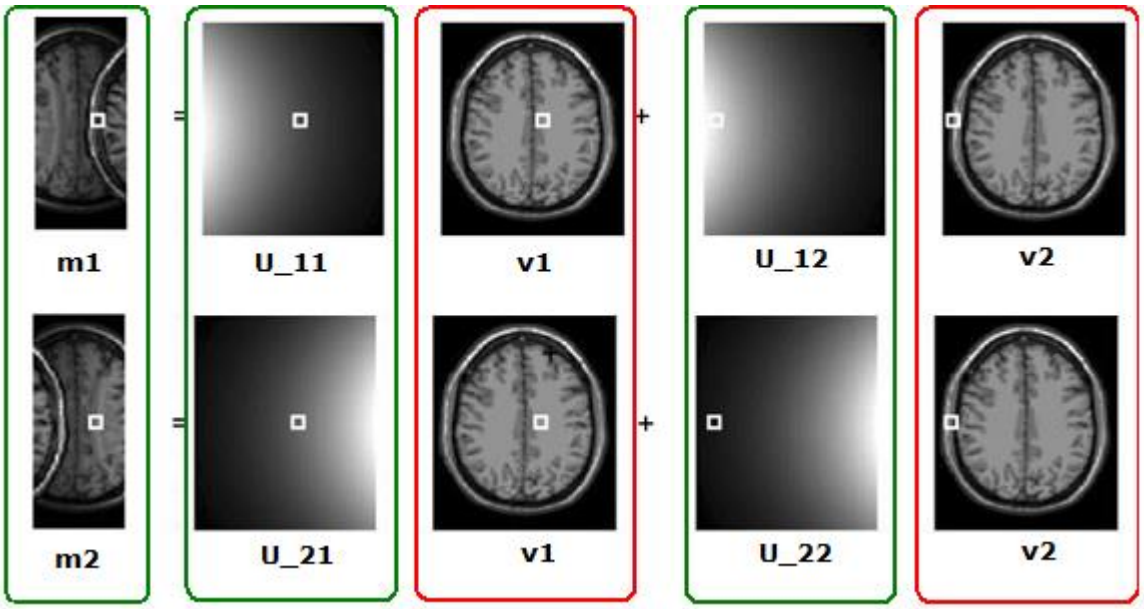

Figure 4-3. *Graphic example of the matrix operation to 'unwrap' the super-imposed signal from pixels in the under-sampled image $\vec{m}$ (where has 'n' pixels $\vec{m} = [m_1, m_2, \ldots, m_n]$), using the unfolding matrix U (see equation (4-11)).*

The previously described approach is a special case of SENSE, where the point spread function of the under-sampling pattern is regular and well known, i.e. the FT of a comb function (the under-sampling) is another comb function (the aliased image) with neat equally-spaced peaks, allowing to unpick the "wrapped up" pixels with minimum computation. In its general case, SENSE can be applied using any type of arbitrary under-sampling trajectory, however the aliasing pattern arising from non-Cartesian or random (or pseudo-random) sampling could be quite complicated, non-isotropic and spread-out leading to a rather massive sensitivity encoding matrix S, thus making equation (*4-11*) very difficult to compute.

Pruessmann *et al.* [3] proposed an efficient approach to solve equation (*4-11*) using the conjugate gradient (CG) method, which starts with a guess or approximate solution and progressively converges to the exact solution $\vec{u}$ after a number of iterations. An encoding matrix E is defined, including the gradient (Fourier) effect and the coils sensitivity weighting, at the same time, the noise matrix Ψ is replaced by a density correction matrix D and an intensity correction matrix I is also introduced, yielding:

$$(IE^H DEI)(I^{-1}\vec{u}) = IE^H D\vec{m}$$

or

$$(IE^H DEI)\vec{b} = \vec{a} \tag{4-12}$$

Where $\vec{a}$ and $\vec{b}$ are the input and output of a linear problem that can be solved with CG. The CG algorithm is based in finding a local minimum of a function through a series of iterations 'following' the function's conjugate gradient direction (assuming the gradient exist, i.e. the function is differentiable at that point). In this case, the unconstrained optimization problem in its *Lagrangian* form may be expressed as:

$$argmin_{\vec{b}} \left\| (IE^H DEI)\vec{b} - \vec{a} \right\|_2^2 \quad (4\text{-}13)$$

Using this method, it has been shown that only a few iteration steps are necessary to converge to an accurate solution [3, 7-9].

Generalized Auto-calibrating Partially Parallel Acquisitions

The Generalized Auto-calibrating Partially Parallel Acquisitions (GRAPPA) was developed in 2002 by Griswold *et al.* [10] and, similar to SENSE, it has been widely adopted in clinical practice because it allows 2-3 times acceleration of the image acquisition and robust SNR.

The GRAPPA scheme proposes a model to interpolate a missing line between acquired lines in a single coil, by using the information from the acquired lines from every coil in addition to a number of calibration lines. The spatial modulation in the signal introduced by the combination of multiple receiver coils can be represented as a sum of harmonics in the same way as the spatial modulation obtained by gradients. In a periodic under-sampling pattern such as missing every other line, e.g. a missing line is $n \times \Delta k_y$ where $n = 2{:}\,2{:}\,k_{max}$ and Δk_y is the original k_y resolution, the MR signal S for such missing line in the absence of coil modulation would be:

$$S(k_y + n\Delta k_y) = \iiint_{FOV_y} M(y)\, e^{-2i\pi(n\Delta k_y\, y)} e^{-2i\pi(k_y\, y)} dy \quad (4\text{-}14)$$

Where, as before, M is the distribution of the magnetization. On the other hand the signal of an acquired line from a single coil j is,

$$S_j(k_y) = \iiint_{FOV_y} M(y)\, c_j(y) e^{-2i\pi(k_y\, y)} dy \quad (4\text{-}15)$$

With c_j the coil sensitivity modulation. From equations (4-14) and (4-15) a missing line $n\Delta k_y$ can be approximated as a linear combination of signals from all the coils for an acquired line k_y with weights w_j^n :

$$S(k_y + n\Delta k_y) = \sum_{j=1}^{n} w_j^n \, S_j(k_y) \tag{4-16}$$

Where,

$$\sum_{j=1}^{n} w_j^n \, c_j(y) \approx e^{-2i\pi(n\Delta k_y \, y)}$$

Therefore, the estimation of a missing k-line becomes a problem of finding the correct w_j^n weights, which is done by acquiring a few calibration lines, e.g. a limited part of (central) k-space is fully sampled, whereby the weights can be found without explicitly calculating the coil sensitivities. Those weights can then be used to estimate the missing lines from all parts of k-space. GRAPPA uses a number of adjacent acquired and non-acquired line pairs, or blocks, as well as all their coil contributions to interpolate a single missing line in each single coil (as seen in a scheme in **Figure 4-4**). In their seminal work, Griswold *et al.* [10] showed that using only a few blocks (between 4 to 6) can provide a robust estimation and improved quality with respect to other k-space interpolation algorithms [11, 12] yet remain computationally efficient.

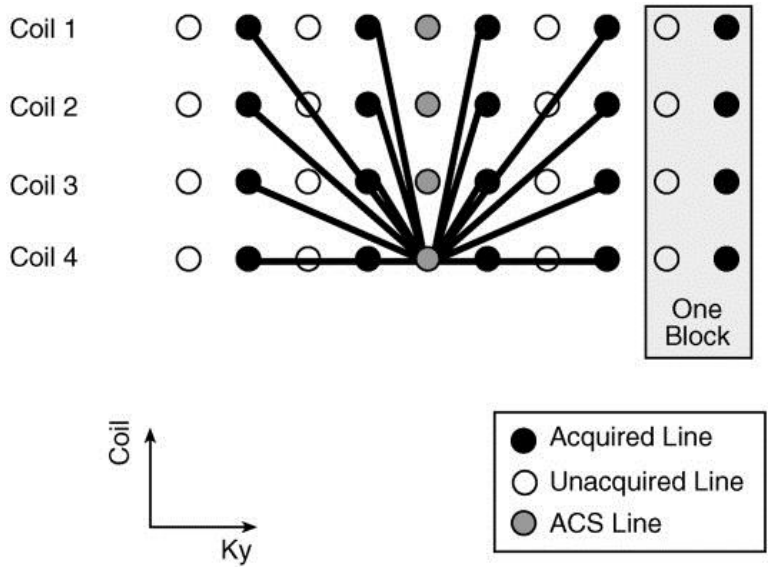

Figure 4-4*. Scheme of the basic GRAPPA algorithm. In this example with reduction factor R=2, four acquired lines in every coil are used to fit one ACS line in coil #4. One block is defined as a single acquired line and R-1 missing lines, therefore, in this case each a four-block reconstruction is performed at a time to recover each missing line from each coil. Figure obtained from Griswold et. al.[10] , copyright license order number* ***4677610694018*** *RightsLink / John Wiley Sons.*

Compressed Sensing

Another approach to reconstruct under-sampled MRI acquisitions is to use the mathematical theory of Compressed Sensing (CS) to take advantage of sparsity in MR images [13]. The sparsity condition means that the image can be faithfully reconstructed from only a portion of the total original information, provided that such portion is chosen appropriately. This is similar to algorithms for image compression such as JPEG, where an image is transformed into a vector of sparse coefficients and then only the main coefficients are stored for later reconstruction while the rest of the information is discarded [14]. In CS MRI, the data acquisition time is reduced by under-sampling the k-space in a way that only those "significant" coefficients are collected in the first place. Importantly, the transform or point spread function of the under-

sampling trajectory must be wide and noise-like so that its contribution to the main coefficients is minimal.

Sparsity is not necessarily required in image space, as long as a linear transformation can be applied that enforces sparsity in the transform domain. MR images often have repetitive features or objects, e.g., modular bones in the spine, fractal-like vessels, nerves or fibrous tissue, which makes them good candidates for sparsity in well-known transform domains such as wavelet or discrete cosine (widely used for image compression [15]). Multiple contrasts or time-series MR images are also highly compressible in the contrast or time dimension because of redundancy [16].

The reconstruction of the image from an under-sampled k-space may be obtained by solving a constrained optimization problem that enforces sparsity in the transform domain and data consistency [13],

$$\min\|\Psi\vec{u}\|_1$$

$$s.t.\ \|\mathcal{F}_u\vec{u} - \vec{m}\|_2 < \mathcal{E} \qquad (4\text{-}17)$$

Where Ψ is the transform operator, $\vec{u}$ is the image vector, $\mathcal{F}_u$ is the operator that transforms the image into the under-sampled Fourier k-space, $\vec{m}$ is the measured (under-sampled) data and $\mathcal{E}$ is the threshold that enforces data consistency. Here, the l_1 norm in the objective function is the main enforcer of sparsity.

High-dimensionality under-sampled patch-based reconstruction

The redundancy in MR images may be used not only to enforce sparsity in a transform domain but also to exploit their low-rank, which means that the number of linearly independent rows or columns in an image is significantly lower than the total number of rows or columns. This

is particularly useful in multiple contrast MRI, e.g. T1 or T2 parameter mapping, where the low-rank nature of the data along the contrast dimension can be used to accelerate the inherently long acquisitions [17]. The high dimensional under-sampled patch-based reconstruction (HD-PROST) technique [18], which exploits low-rank at local and global scale in the contrast domain in combination with parallel imaging, has been shown to accelerate multiple MT-weighted acquisitions up to 5-fold (as shown in an example in **Figure 4-5**).

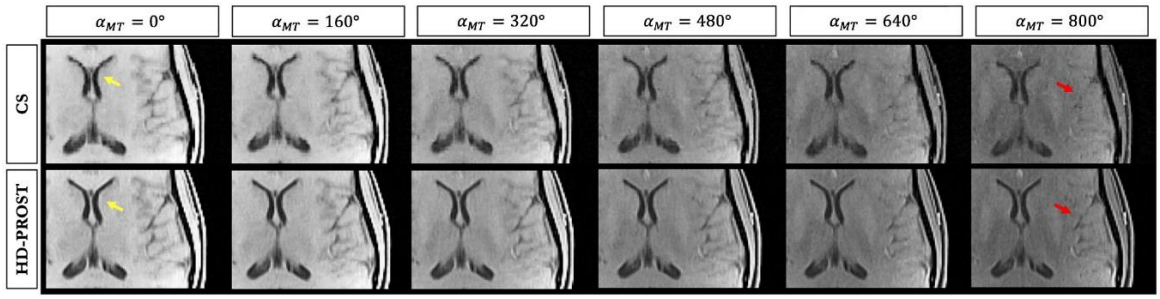

***Figure 4-5**. Comparison of Compressed Sensing (CS) and HD-PROST reconstruction of a multi-contrast 3D brain acquisition in a healthy subject with variable MT flip angle α_{MT} from 0˚ to 800˚. Fine details and anatomic structures can be recovered efficiently with HD-PROST as shown by the arrows. Figure obtained from Bustin et. al. [18].*

In 3D patch-based under-sampled reconstruction (PROST) [19], a group k of similar or neighbouring 3D image patches p_k are stacked in vectorised form in a low-rank 2D matrix so they can be approximated as $p_k \approx D_k \alpha$, where D_k is a fixed dictionary and α is a vector containing a few sparse coefficients obtained by Singular Value Decomposition (SVD). The HD-PROST [18] method is a generalization of PROST where 3D patches from all (multiple contrast) images are stacked in a third order tensor T_p by a path selection operator P_p according to local (within patch), non-local (between patches) and spectral (between contrasts) similarity to create a core tensor of smaller size using high order SVD. In this way, the MR reconstruction can be formulated as a constrained optimization problem,

$$argmin_{\vec{u}} \ \frac{1}{2}\|E\vec{u} - \vec{m}\|_F^2 + \sum_p \lambda_p \ \|T_p\|_* \tag{4-18}$$

$$s.t. \ \ T_p = P_p(\vec{u})$$

Where E is the encoding matrix (including Fourier, under-sampling trajectory and coil sensitivities contributions), $\|\,.\,\|_F$ is the Frobenius norm, λ_p is the sparsity regularization parameter, $\|\,.\,\|_*$ is the nuclear norm, $\vec{u}$ is the solution and $\vec{m}$ the measured data**.** The first term in equation (*4-18*) ensures data consistency, while the second term promotes the sparsity of the tensor. Bustin *et al.* [18] solves this equation using the alternating direction method of multipliers (ADMM) to split the problem into two optimizations: (I) the multi-channel multi-contrast MR reconstruction, which is a regularized iterative SENSE formulation including the tensor within the sparsity promoting term, and (II) the optimization of α (i.e. the dominant components of the core tensor) through the groups of image patches, generating the de-noised tensor that is fed back to (I) as *prior* in every iteration.

Motion in the Heart

Translational Motion Correction

The motion of an object during MR acquisition causes artefacts in the reconstructed image. Significant motion can occur in multi-shot sequences where the acquisition of k-space for a single image is spread over a long period of time e.g. a large number of heartbeats. Multi-shot sequences are common in cardiac imaging, for example, in high resolution and/or 3D acquisitions. Even within a single heartbeat, the motion of a beating heart can be substantive and complex, having two major contributors: (1) the contracting and expanding of the heart muscle itself or cardiac motion; and (2) the bulk displacement of the entire heart by adjacent organs (e.g. diaphragm, lungs) due to breathing, or respiratory motion.

The characterisation of the first contributor of the motion of the heart (i.e. cardiac motion) may often be a focus of MRI examinations, e.g. for calculation of functional parameters such as left ventricle ejection fraction, via time-resolved MRI (or cine) where the acquisition of each image takes place during a window of time (approx. 20-30 ms) short enough that cardiac motion can be neglected [20]. However, other examinations such as coronary artery/vein [21] or scar imaging [22] require high spatial resolution, which is typically incompatible with breath held MRI. In these cases, a common way to avoid cardiac motion in the images is to perform a multi-shot sequence with a short acquisition window which is synchronised with the electrocardiogram and centred in a quiescent period of the cardiac cycle (systole or mid-diastole, such as in Peters *et al*. [22]).

The second contributor to the motion of the heart (i.e. respiratory motion) does not have an obvious prognostic value in cardiac imaging, however, it plays a very important role in the degradation of image quality via motion artefacts and therefore many techniques exist to either minimize, correct or resolve respiratory motion in cardiac MRI. A straight-forward approach to avoid respiratory motion is to ask a patient to hold their breath during data acquisition, however, this imposes a restriction on the length of the acquisition, i.e., a patient cannot typically hold their breath for more than 15 to 20 seconds. For this reason, high resolution and/or 3D acquisitions require different solutions. Navigator-based free-breathing techniques which prospectively accept or reject data acquired during a specific respiratory phase or position (typically end-expiration) are popular for high resolution 3D MRA [21, 23, 24]. These approaches assume that the respiratory-induced motion of the heart is periodic, so the effect of respiratory motion can be minimised by acquiring data at a similar respiratory position over multiple breathing cycles. In order to monitor the breathing cycle, navigators are acquired just before or after the high-resolution data acquisition, by tracking the *head-to-foot* motion of a high-contrast region in the image, such as the position of the lung/liver interface. By defining

a small acceptance window (i.e., *gating*), the navigator-based approaches have been shown to produce high quality images. However, depending on the respiratory pattern of the subject (i.e. the fraction of data that is acquired within the acceptance window) the scan efficiency can be very low (30-50%) leading to prolonged and unpredictable acquisition times. Furthermore, the navigator-based approach does not measure the motion of the heart directly, rather, it assumes a linear correlation between the motion of the diaphragm and the motion of the heart. This simplified model does not consider the effect of respiratory motion in directions other than *head-to-foot* nor non-rigid motion.

To address some of the limitations of diaphragmatic navigator techniques, Henningsson *et al.* [25] developed a beat-to-beat motion correction strategy using 2D image navigators (iNAVs) or low-resolution images acquired during the start-up pulses of a balanced Steady-State Free-Precession (bSSFP) readout. When acquired in coronal orientation, the 2D iNAVs allow to detect the heart's translational motion by template matching in the *head-to-foot* and *left-to-right* directions so the motion can be corrected in every heartbeat using a property of the Fourier Transformation [26]:

$$\vec{v}_t = \vec{m}_t \cdot e^{2i\pi \vec{\mathrm{k}}_t \cdot \mathrm{d}_{t,t_0}} \tag{4-19}$$

Where $\vec{v}_t$ and $\vec{m}_t$ represent acquired and corrected signals for heart-beat t, respectively, $\vec{\mathrm{k}}_t$ is the k-space trajectory vector and during heartbeat t, and d_t is the respiratory motion displacement (or translation) measured in heartbeat t with respect to a reference heartbeat t_0, obtained from the iNAVs' tracking.

Non-Rigid Motion Correction

Compared to diaphragmatic navigator gating, the iNAV approach has the advantage of directly measuring the respiratory motion of the heart. However, it still uses a simplified model for the complex non-rigid deformation of the heart during free breathing. On the other hand, Prieto *et*

al. [7] proposed a solution to the efficiency problem of diaphragmatic navigators with a self-navigated Cartesian golden-step spiral profile acquisition. In this approach, under-sampled images are created from every shot to retrospectively 'bin' the data into respiratory phases (or positions). Then, images of the respiratory phases are registered to yield 3D affine motion fields which are incorporated into the final reconstruction using a formulation for general motion correction (see below, equation *(4-20)*) which uses all the acquired data, i.e., with 100% efficiency. This is possible due to the robustness against under-sampling artefacts of the Cartesian spiral profile acquisition, which samples the centre of k-space in every shot, as shown as an example in **Figure 4-6**.

More advanced motion-compensated reconstruction techniques are needed to address all of the challenges that the motion of the heart poses to cardiac MRI. For example, some of the approaches described above may be used in combination, such as Cruz *et al.* [9] which proposes respiratory phase binning [7] and beat-to-beat translational motion correction [25] to develop a non-rigid motion correction framework for 3D whole-heart cardiac imaging reconstruction. One of the main advantages of this framework is the significant reduction in scan time (due to increased efficiency) at little to no cost in image quality compared to a standard gated acquisition [8, 9]. Another advantage is the modular structure of the acquisition, retrospective reconstruction and motion correction which enables great flexibility for different contrast preparations.

For these reasons, Cruz's framework was adopted in multiple instances throughout this work and its main features are described in detail in the following sections.

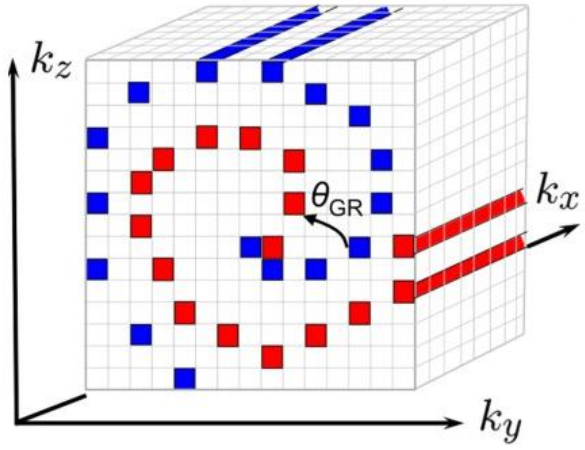

***Figure 4-6**. A scheme of the 3D Cartesian trajectory with spiral profile (CASPR). One spire is obtained in every heartbeat with an angular step difference θ_{GR} given by the golden ratio, as shown here between spire n (red) and spire $n+1$ (blue). Figure extract obtained from Prieto et. al. [7], copyright license order number **4677610448930** RightsLink / John Wiley and Sons.*

Beat-to-beat navigation and binning

A stack of iNAVs acquired in each beat is used to measure the displacement values d_{t,t_0}, from equation (*4-19*), regarding translational motion of the heart in the *foot-to-head* and *left-to-right* directions. The amplitude of the motion is calculated by matching a template or patch cropped around the heart from a reference iNAV (at a given time t_0, typically in end-expiration) to the rest of the INAVs using, for instance, normalized cross correlation.

The displacement vector is used to assign the data into respiratory phases according to the amplitude of the motion in the *foot-tohead* direction. The k-space data is then separately corrected for motion to the centre of each bin using equation (*4-19*).

Non-rigid registration and motion fields

Following the intra-bin translational motion correction, iterative SENSE reconstructed bin images undergo fast 3D non-rigid registration using the NiftyReg package [27] to compute 3D motion fields between respiratory phases.

MR reconstruction

The motion fields U_b for each bin $b = 1..n$, coil sensitivity maps S_c, Fourier transform F, k-space sampling trajectory J_b and bin images I_b are incorporated in a generalized matrix description of MR reconstruction [28], using an iterative SENSE implementation which defines the fully (inter-bin) motion-corrected volume Γ as:

$$\Gamma = argmin_I \{EI - \vec{v}_2^2\} \tag{4-20}$$

with,

$$EI = \sum_{b=1}^{n} J_b F S_c U_b I_b$$

Where E is the *encoding* matrix acting on the uncorrupted image I and $\vec{v}$ is the intra-bin motion-corrected k-space data. The unconstrained optimization problem in equation *(4-20)* may be solved similar to equation *(4-13)* by using a linear CG method and, optionally, including a regularization parameter such as the previously described patched based low-rank reconstructions, PROST [19] or HD-PROST [18].

REFERENCES

1. Nussbaumer, H.J. and P. Quandalle, *Fast Computation of Discrete Fourier-Transforms Using Polynomial Transforms.* Ieee Transactions on Acoustics Speech and Signal Processing, 1979. **27**(2): p. 169-181.
2. Sha, L., H. Guo, and A.W. Song, *An improved gridding method for spiral MRI using nonuniform fast Fourier transform.* J Magn Reson, 2003. **162**(2): p. 250-8.
3. Pruessmann, K.P., et al., *Advances in sensitivity encoding with arbitrary k-space trajectories.* Magn Reson Med, 2001. **46**(4): p. 638-51.
4. Pruessmann, K.P., et al., *SENSE: sensitivity encoding for fast MRI.* Magn Reson Med, 1999. **42**(5): p. 952-62.

5. Uecker, M., et al., *ESPIRiT--an eigenvalue approach to autocalibrating parallel MRI: where SENSE meets GRAPPA.* Magn Reson Med, 2014. **71**(3): p. 990-1001.
6. Griswold, M.A., et al., *Autocalibrated coil sensitivity estimation for parallel imaging.* NMR Biomed, 2006. **19**(3): p. 316-24.
7. Prieto, C., et al., *Highly efficient respiratory motion compensated free-breathing coronary MRA using golden-step Cartesian acquisition.* J Magn Reson Imaging, 2015. **41**(3): p. 738-46.
8. Munoz, C., et al., *Motion-corrected simultaneous cardiac positron emission tomography and coronary MR angiography with high acquisition efficiency.* Magn Reson Med, 2018. **79**(1): p. 339-350.
9. Cruz, G., et al., *Highly efficient nonrigid motion-corrected 3D whole-heart coronary vessel wall imaging.* Magn Reson Med, 2017. **77**(5): p. 1894-1908.
10. Griswold, M.A., et al., *Generalized autocalibrating partially parallel acquisitions (GRAPPA).* Magn Reson Med, 2002. **47**(6): p. 1202-10.
11. Heidemann, R.M., et al., *VD-AUTO-SMASH imaging.* Magn Reson Med, 2001. **45**(6): p. 1066-74.
12. Bydder, M., D.J. Larkman, and J.V. Hajnal, *Generalized SMASH imaging.* Magn Reson Med, 2002. **47**(1): p. 160-70.
13. Lustig, M., D. Donoho, and J.M. Pauly, *Sparse MRI: The application of compressed sensing for rapid MR imaging.* Magn Reson Med, 2007. **58**(6): p. 1182-95.
14. Wallace, G.K., *The JPEG still picture compression standard.* IEEE transactions on consumer electronics, 1992. **38**(1): p. xviii-xxxiv.
15. Starck, J.L., M. Elad, and D.L. Donoho, *Image decomposition via the combination of sparse representations and a variational approach.* IEEE Trans Image Process, 2005. **14**(10): p. 1570-82.
16. Lustig, M., *Sparse mri*. Vol. 69. 2008.
17. Zhao, B., et al., *Accelerated MR parameter mapping with low-rank and sparsity constraints.* Magn Reson Med, 2015. **74**(2): p. 489-98.
18. Bustin, A., et al., *High-dimensionality undersampled patch-based reconstruction (HD-PROST) for accelerated multi-contrast MRI.* Magn Reson Med, 2019. **81**(6): p. 3705-3719.
19. Bustin, A., et al., *Five-minute whole-heart coronary MRA with sub-millimeter isotropic resolution, 100% respiratory scan efficiency, and 3D-PROST reconstruction.* Magn Reson Med, 2019. **81**(1): p. 102-115.
20. Sechtem, U., P. Pflugfelder, and C.B. Higgins, *Quantification of cardiac function by conventional and cine magnetic resonance imaging.* Cardiovasc Intervent Radiol, 1987. **10**(6): p. 365-73.
21. Stuber, M., et al., *Double-oblique free-breathing high resolution three-dimensional coronary magnetic resonance angiography.* J Am Coll Cardiol, 1999. **34**(2): p. 524-31.
22. Peters, D.C., et al., *Left ventricular infarct size, peri-infarct zone, and papillary scar measurements: A comparison of high-resolution 3D and conventional 2D late gadolinium enhancement cardiac MR.* J Magn Reson Imaging, 2009. **30**(4): p. 794-800.
23. Spuentrup, E., et al., *Navigator-gated free-breathing three-dimensional balanced fast field echo (TrueFISP) coronary magnetic resonance angiography.* Invest Radiol, 2002. **37**(11): p. 637-42.
24. Danias, P.G., et al., *Prospective navigator correction of image position for coronary MR angiography.* Radiology, 1997. **203**(3): p. 733-6.

25. Henningsson, M., et al., *Whole-heart coronary MR angiography with 2D self-navigated image reconstruction.* Magn Reson Med, 2012. **67**(2): p. 437-45.
26. Bracewell, R., et al., *Affine theorem for two-dimensional Fourier transform.* ELECTRONICS LETTERS-IEE, 1993. **29**: p. 304-304.
27. Modat, M., et al., *Fast free-form deformation using graphics processing units.* Comput Methods Programs Biomed, 2010. **98**(3): p. 278-84.
28. Batchelor, P.G., et al., *Matrix description of general motion correction applied to multishot images.* Magn Reson Med, 2005. **54**(5): p. 1273-80.

Chapter 5 : Contrast-Free High-Resolution 3D Magnetization Transfer Imaging for Simultaneous Myocardial Scar and Cardiac Vein Visualization

Contrast-free high-resolution 3D magnetization transfer imaging for simultaneous myocardial scar and cardiac vein visualization

Karina López[1], Radhouene Neji[1,2], Rahul K. Mukherjee[1], John Whitaker[1], Alkystis Phinikaridou[1], Reza Razavi[1], Claudia Prieto[1], Sébastien Roujol[1], René Botnar[1]

[1]*School of Biomedical Engineering and Imaging Sciences, King's College London, UK*

[2]*MR Research Collaborations, Siemens Healthcare Limited, Frimley, UK*

Manuscript accepted by *Magnetic Resonance Materials in Physics, Biology and Medicine* on 29 January 2020 (published on 20 February 2020) [1]. Minor layout changes have been made to the submitted manuscript to fit the logical structure of the present report.

Abstract

Object: To develop a three dimensional (3D) high-resolution free-breathing Magnetization Transfer Ratio (MTR) sequence for contrast-free assessment of myocardial infarct and coronary vein anatomy.

Materials and Methods: Two datasets with and without off-resonance magnetization transfer preparation were sequentially acquired to compute MTR. 2D image navigators enabled beat-to-beat translational and bin-to-bin non-rigid motion correction. Two different imaging sequences were explored. MTR scar localization was compared against 3D late gadolinium enhancement (LGE) in a porcine model of myocardial infarction. MTR variability across the left ventricle and vessel sharpness in the coronary veins were evaluated in healthy human subjects.

Results: A decrease in MTR was observed in areas with LGE in all pigs (non-infarct: 25.1±1.7% vs infarct: 16.8±1.9%). The average infarct volume overlap on MTR and LGE was 62.5±19.2%. In humans, mean MTR in myocardium was between 37-40%. Spatial variability was between 15-20% of the mean value. 3D whole heart MT-prepared datasets enabled coronary vein visualization with up to 8% improved vessel sharpness for non-rigid compared to translational motion correction.

Discussion: MTR and LGE showed agreement in infarct detection and localization in a swine model. Free-breathing 3D MTR maps are feasible in humans but high spatial variability was observed. Further clinical studies are warranted.

Author's contributions

Lopez: study design, implementation of MT sequence in Siemens PPE, acquisition of all data related to phantom and human experiments, implementation of some of the reconstruction code, reconstruction, analysis and interpretation of all data and drafting of manuscript.

Neji: study design, acquisition of data and critical revision.

Mukherjee: acquisition of data related to the animal study and critical revision.

Whitaker: acquisition of data related to the animal study and critical revision.

Phinikaridou: acquisition of data related to the phantom experiments and critical revision.

Razavi: critical revision.

Prieto: conception and design of data acquisition and motion correction, acquisition of data and critical revision.

Roujol: design and critical revision.

Botnar: conception and overall study design, data acquisition and motion correction, interpretation of data and critical revision.

In the present study, acquisition of data involves the collection of data itself as well as the development of techniques and/or samples specially tailored for the collection of data in this study.

Introduction

MRI plays an important role for non-invasive assessment of myocardial fibrosis in patients with ischemic and non-ischemic cardiomyopathies. Myocardial scar assessment has been shown to have important prognostic value [2-4]. Furthermore, in patients requiring cardiac resynchronization therapy, detection of focal fibrosis and coronary sinus/vein anatomy may help to guide intervention and implantation of intra cardiac defibrillators [5]. In these applications the accurate discrimination of fibrotic or scarred tissue from surrounding healthy myocardium is crucial.

Late gadolinium enhancement (LGE) MRI is the gold standard for the assessment of myocardial fibrosis [6]. LGE shows enhanced signal intensity by targeting the enlarged extracellular space in fibrotic tissue using gadolinium-based contrast agents [7]. LGE is a qualitative approach where the time point of imaging after the injection of a contrast agent determines the pattern of enhancement. While core infarct regions will enhance strongly and late during the contrast wash-out (> 25 min), the signal from the rim of an infarcted region (area at risk) may enhance very early on (2-3 min), only to return to normal at the late stage of contrast wash-out [8]. Furthermore, the use of gadolinium-based contrast agents may generate accumulation in the neural system [9] and/or adverse contrast reaction. Therefore, the development of a semi-quantitative and gadolinium-free approach for the assessment of myocardial fibrosis may be of great interest.

Magnetization Transfer (MT) is an endogenous MR contrast mechanism, which does not require the injection of a contrast agent. MT has shown to be sensitive to structural changes associated with myocardial fibrosis, such as the increase in collagen content [10-12]. MT was first demonstrated by Wolff and Balaban in kidney and skeletal muscle [13], showing a signal decrease from free water protons, after selectively saturating a pool of protons with restricted motion with an off-resonance preparation. The signal decrease is explained by an exchange of magnetization between the water protons (free pool) and those with restricted motion (bound pool). The characteristics of the exchange are determined by the tissue composition, in particular, the size and distribution of its macromolecular or bound pool component.

A common application of MT contrast has been to suppress signal coming from protein-rich tissue, such as white-matter or muscle [14, 15]. This effect can generate good contrast between myocardium and blood irrespective of blood oxygenation and therefore improve cardiac vein visualization [16]. While T2 preparation is known to be useful in coronary angiography [17], the large reduction in T2 of deoxygenated blood causes difficulty in coronary vein imaging. MT preparation is largely independent of the magnetic susceptibility effect that causes T2 reduction in venous blood and has been shown to generate a contrast enhancement that is superior to T2 based approaches in the cardiac veins [18].

Another application of MT in cardiac MRI is the semi-quantitative Magnetization Transfer Ratio (MTR). In MTR, two images are acquired, with and without MT preparation, and the percentage difference or ratio between them is calculated. A breath-held 2D cine steady state technique has shown reduced MTR values associated with LGE enhancement in acute myocardial infarction (MI) patients [19]. However, breath-holding can be difficult in sick patients, where the length of breath-hold may limit the spatial resolution and different breath-hold positions may lead to misregistration artefacts between slices. Germain *et al.* has recently proposed a diaphragmatic navigated free-breathing 3D on-resonance MT approach [20], where

they show some agreement between LGE enhancement and reduced MT effects in patients with acute or recent MI. However, partial volume effects and likely residual motion seem to have caused significant intra and inter subject variability. We hypothesize that a significant increase in slice resolution and two-dimensional navigation may have a good impact in reproducibility and accuracy.

To address the above challenges, we developed and evaluated a novel free-breathing motion corrected 3D whole-heart MTR sequence for the simultaneous assessment of localized fibrosis and coronary vein anatomy without the administration of a contrast agent.

Methods

Sequence acquisition & reconstruction

A prototype motion corrected free-breathing 3D magnetization transfer contrast imaging sequence was implemented on a 1.5T MR scanner (MAGNETOM Aera, Siemens Healthcare, Erlangen, Germany). The sequence is comprised of two sequentially acquired 3D datasets, one with MT preparation and one without any preparation (hereon dataset REF).

A pulse diagram of the sequence is shown in **Figure 5-1A**. Each acquisition was performed with a Cartesian trajectory with spiral profile order [21] and preceded by a 2D image navigator (iNAV) [22] to enable beat-to-beat translational motion correction in foot-to-head and left-to-right directions. The iNAVs were generated by spatially encoding the first 14 (start-up) pulses of the imaging sequence. The high-resolution 3D datasets were acquired in segmented fashion over multiple heartbeats and imaging started from the 15th pulse in every heartbeat. The spiral-profile Cartesian trajectory was chosen because it produces incoherent and noise-like undersampling artifacts which are beneficial for undersampled reconstruction. In addition, it provides some motion robustness associated with spiral sampling (e.g., k-space centre is

sampled on every heart-beat) while maintaining a Cartesian computationally efficient reconstruction.

Spoiled gradient echo (SPGR) and balanced steady-state free-precession (bSSFP) imaging modules were investigated with the described MT preparation module. Data sampling was made to coincide with the diastolic resting period to minimize the impact of cardiac motion. The subject-specific trigger delay time and data acquisition window were determined using a free-breathing 2D cine (following standard local protocol), acquired in transversal orientation prior to the proposed sequence.

The MT preparation (represented in **Figure 5-1B**) consisted of a train of 20 Sinc-shaped off-resonance RF pulses with individual length of 20.48ms, separated by 1.5ms pause periods. The preparation train was played out immediately before the imaging module in every heartbeat (or segment) of the MT-prepared image. The off-resonance frequency and flip angle of the pulses were optimized as described in the following sections.

Off-line reconstruction and post-processing was done in Matlab (The MathWorks, Inc., Natick, MA, USA). Two types of motion correction approaches were evaluated: (I) Beat-to-beat 2D translational motion correction, and (II) combined beat-to-beat 2D translational plus bin-to-bin non-rigid motion correction [23]. A scheme of the data flow is shown in **Figure 5-2A**.

Beat-to-beat translational motion correction was performed by compensating the displacement in image space with a linear phase shift in k-space, using a property of Fourier transformations [24]:

$$K_{cor} = K_{acq} e^{2i\pi \vec{k}\cdot\vec{d}} \tag{5-1}$$

where K_{acq} and K_{cor} represent the acquired and corrected data, respectively, $\vec{k}$ is the k-space trajectory vector (k_x, k_y) and $\vec{d}$ is the respiratory motion displacement (d_x, d_y) in the left-to-

right and foot-to-head directions, respectively, obtained from the iNAVs by normalized cross-correlation.

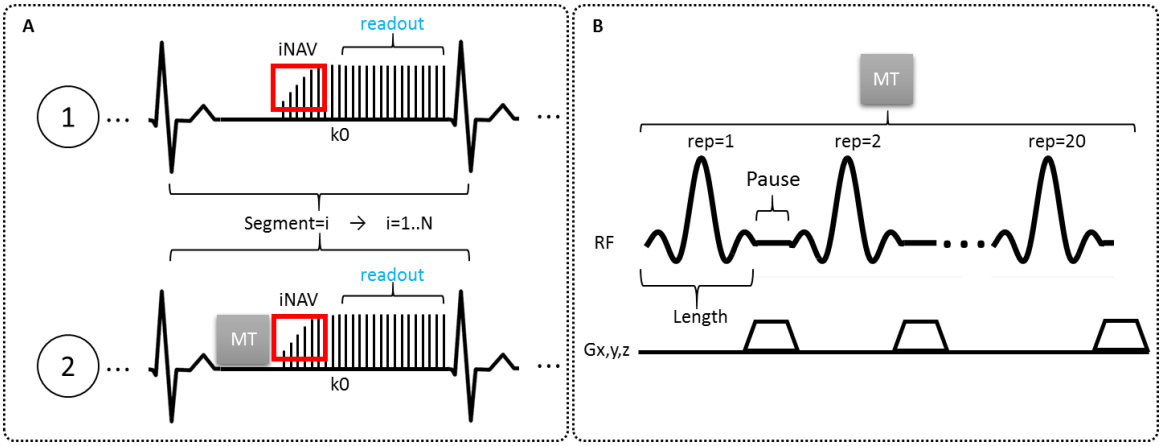

Figure 5-1. *(A) Acquisition scheme for the two 3D segmented (Electrocardiogram-triggered) datasets (with bSSFP), the reference (REF) dataset (without prepration) and the MT-preapred dataset (with MT preparation) are acquired sequentially. Both acquisitions include 2D image navigators (iNAVs) obtained by encoding the first 14 start-up pulses of the imaging module. (B) Scheme of the MT prepration module which consisted of twenty off-resonance pulses (20ms) separated by pause periods (1.5ms) where 3D spoiler gradients were played out.*

In the non-rigid motion correction framework, respiratory motion in the foot-head direction was derived from the iNAVs to assign the data into respiratory phases or bins (3 to 5 bins, maximum bin size 3.5 mm). Then, beat-to-beat 2D translation motion correction in the left-to-right and foot-to-head directions (according to equation (1)) was applied with respect to the centre of each bin, followed by iterative SENSE reconstruction to obtain an intra-bin motion corrected 3D image for image each respiratory phase so that 3D motion fields between respective respiratory phases (i.e. bins) could be obtained via non-rigid registration [25] of the 3D images. The parameters involved in the estimation of 3D motion fields include the weight of the penalty (i.e. in our case the bending energy) for an objective function based on normalized mutual information (using values as proposed by Modat *et al.* [25]) and the spacing

or size of the deformation grid (in each of the three dimensions). Spacing was adjusted according to image resolution with an iterative experimental approach.

The motion fields, coil sensitivity maps, sampling trajectory and measured k-space data were incorporated in a motion-corrected generalized matrix description (GMD) [23, 26], whereby a motion-corrected 3D dataset was then obtained by solving the inverse problem using a conjugate gradient algorithm.

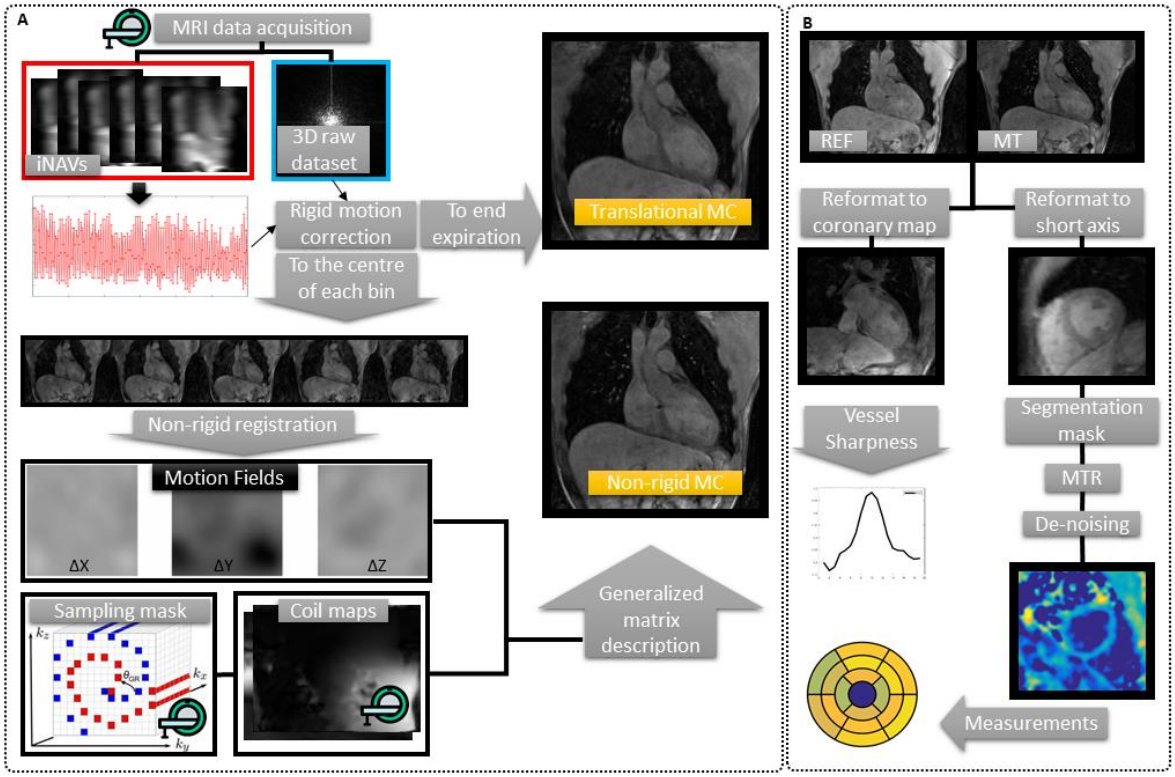

***Figure 5-2**. (A) Data flow during image acquisition and reconstruction. From the top left, raw data and image navigators (iNAVs) were obtained from the scanner; iNAVS were used for translational motion correction in two ways: (1) to the end expiration phase for translational motion correction (MC); (2) to the centre of each respiratory phase (or bin), followed by non-rigid registration of the bins and generation of 3D motion fields. Non-rigid MC was performed using a generalized matrix description that included the calculated motion fields, sampling mask and coil maps. (B) Data flow during image analysis. MT and REF datasets were reformatted to either a 2D coronary projection image for vessel sharpness calculation, or to left-ventricle short axis view for manual segmentation and creation of a mask. MTR maps were calculated from non-reformatted MT and REF datasets. A blurring Gaussian filter was applied in the MTR maps before segmentation measurements.*

Motion correction was applied to the MT-prepared and REF datasets independently. In each, an end-expiration position iNAV was chosen as 'reference' for the cross-correlation procedure After motion corrected reconstruction, the MT-prepared and REF datasets were co-registered to correct any small misalignments [25]. MTR maps were calculated voxel-wise as:

$$MTR = 100 \times \left(1 - \frac{I_{MT}}{I_{Ref}}\right) \quad (5\text{-}2)$$

where I_{MT} and I_{REF} are the signal intensity of the MT and REF datasets, respectively.

Numerical simulations

Bloch simulations with a two-pool model of exchange were used to determine optimal MT preparation parameters. The evolution of the transverse and longitudinal magnetization of the free pool ($M_{x,y}^A$, M_z^A, respectively) and bound pool ($M_{x,y}^B$, M_z^B, respectively) under off-resonance irradiation with frequency ΔF and amplitude ω_1 can be described by a modified set of Bloch equations [27]:

$$\frac{\partial M_x^A}{\partial t} = -2\pi\Delta F M_y^A - \frac{M_x^A}{T_2^A} - \Im(\omega_1) M_z^A \quad (5\text{-}3)$$

$$\frac{\partial M_y^A}{\partial t} = 2\pi\Delta F M_x^A - \frac{M_y^A}{T_2^A} + \mathcal{R}(\omega_1) M_z^A \quad (5\text{-}4)$$

$$\frac{\partial M_z^A}{\partial t} = \Im(\omega_1) M_z^A - \mathcal{R}(\omega_1) M_y^A + R_A(M_0^A - M_z^A) - R M_0^B M_z^A + R M_0^A M_z^B \quad (5\text{-}5)$$

$$\frac{\partial M_z^B}{\partial t} = R_B(M_0^B - M_z^B) - (R_{RFB} + R M_0^A) M_z^B + R M_0^B M_z^A \quad (5\text{-}6)$$

where $\Im$ and $\mathcal{R}$ are the imaginary and real parts of ω_1, respectively. The modification include precession terms associated with the irradiation frequency (ΔF), which are added in equations *(5-3)* and *(5-4)*, while terms dependent of the exchange rate (R) are added in equations *(5-5)* and *(5-6)*. R_A and R_B are the longitudinal relaxation rates of the free (A) and bound (B) pools, respectively.

Under off-resonance irradiation, the bound pool experiences direct saturation of its longitudinal magnetization. This is due to its extremely short T_2, which causes negligible feedback with the transversal components. The saturation rate of the bound pool (R_{RFB}) is calculated as

proportional to the RF power (ω_1^2) and the bound pool's line absorption shape using an experimental super-Lorentzian approximation for semisolid systems [28]. In this model, the bound pool T_2 was fixed at $T_2^B = 14$ μs for all simulations. The equilibrium magnetizations of the bound pool and free pool (M_0^B, M_0^A) represent their size and therefore the ratio $PSR = \frac{M_0^B}{M_0^A + M_0^B}$ is the relative size of the bound pool [29, 30] .

For a series of short and shaped off-resonances pulses, both ω_1 and R_{RFB} are time dependent and no closed-form solution for the resulting magnetization can be found. Portnoy and Stanisz proposed a numerical approach [31] in which the RF pulse is split in small time intervals $dt \approx 50$ μs, whereby its amplitude may be considered constant. The evolution of the net magnetization vector $\vec{M}_{A,B}(t)$ over a time dt is then solved as a linear problem and each transient solution propagates as the initial state for the next interval, until the end of the pulse is reached.

The MTR sequence was simulated using the described model to optimize its sensitivity to the pool size ratio (PSR) in myocardium-like tissue.

Simulated MT preparation parameters included bandwidth=270Hz, Sinc shape, length=20.48ms, delay between pulses=1.5ms, and pulse repetitions n=20. Tissue parameters in myocardial simulations were performed using an exchange rate R of 50 Hz, T_1^A/T_2^A times of 1100/55ms, and PSR of 15%, unless stated otherwise.

Simulations in myocardial-like tissue were performed over a range of ΔF ([200-8000]Hz), MT pulse flip angles ([360-900]˚), B0 inhomogeneity (from -250Hz to 250Hz), free pool relaxation times (T_1^A=[1000-1500]ms, T_2^A=[30-80]ms), and exchange-related parameters (R=[20-70]Hz, PSR=[0-30]%). A simulated constant heartrate of 65 beats per minute (bpm) was used. The signal was measured from the 15th echo (the sampling of the k-space centre) during the 5th

heartbeat, to ensure pseudo steady-state conditions. Two different imaging modules were simulated: (I) SPGR with sequence parameters including TR/TE=3.8/1.6ms and FA=15°, (II) bSSFP with sequence parameters including TR/TE=3.2/1.4ms and FA=70°. A single-pool (no exchange) model was assumed during the pulses of the imaging module.

Phantom study

Agar samples with different concentrations (1%, 2%, 2.5% and 5% agar in water) were prepared and used to validate the signal model and evaluate the performance of the proposed sequence in the presence of different MT exchange parameters and in the absence of motion. The proposed sequence was acquired using SPGR (TR/TE=3.8/1.6ms, FA=15°, BW=401Hz/px, Field of View (FoV) =300×300×112mm3, resolution= 1.4x1.4x4mm3, number of profiles/excitations=30) and bSSFP (TR/TE=3.2/1.4ms, FA=70°, BW=925Hz/px). The MT pulse parameters were the same as described for the simulations. Data were acquired over a wide range of MT pulse flip angles (360-900˚) and off-resonance frequencies (400-8000Hz).

Animal study

Animal experiments were conducted in Landrace pigs (n=3) at the Institut de Chirurgie Guidée par l'image (IHU), Strasbourg, France. The pigs were scanned in-vivo six weeks after undergoing left anterior descending artery occlusion for 3 hours, using the procedure described by Tschabrunn *et al.* [32]. Each animal was scanned with the proposed sequence using the following imaging parameters: coronal orientation, FoV=300×300×108mm3, resolution=1.7x1.7x6mm3, SPGR (TR/TE=3.8/1.76ms, FA=15°, BW=535Hz/px). MT preparation pulses had bandwidth, shape, length, and delay between pulses as described in the Phantom study. MT off-resonance frequency was ΔF =1500Hz, pulse repetitions n=10 and flip angle=720˚.

A 3D bSSFP LGE dataset was obtained following 10-20 minutes after injection of the contrast agent (Gadovist, Bayer, Germany). Imaging parameters included coronal orientation (matching the MTR scan), FoV=200x260x105mm3, acquired/reconstructed resolution= 1.2×1.2×1.2mm3, bSSFP (TR/TE=3.2/1.58ms, FA=90°, BW=930Hz/px).

Respiratory motion was very limited due to ventilation and did not affect the heart position, therefore no motion correction/compensation procedures were applied.

Scar, remote and total myocardium area were manually segmented in LGE images by a single observer (Lopez) with experience in cardiac LGE (approx. 3 years). Automated segmentation was not attempted. MTR scar volume was determined by thresholding in each separate animal, as following: (1) after manually selecting a remote (myocardium) area in the MTR map, mean and standard deviation (σ) were calculated; (2) a mask (*m1*) of the entire myocardium was manually drawn using the MT-weighted dataset (intrinsically co-registered to the MTR map); (3) finally, MTR voxels under the threshold "mean - 2σ" and within *m1* were automatically selected as scar volume. The overlap was defined as the number of coincidences between LGE and MTR scar voxels, divided by the total number of LGE scar voxels:

$$overlap = 100 \times \frac{\#\{LGE_{scar} \cap MTR_{scar}\}}{\#LGE_{scar}} \quad (5\text{-}7)$$

The false positive percentage was calculated using the number of coincidences between MTR scar voxels and LGE remote voxels:

$$false\ positive = 100 \times \left(1 - \frac{\#\{LGE_{remote} \cap MTR_{scar}\}}{\#LGE_{remote}}\right) \quad (5\text{-}8)$$

Healthy subjects study

Ten healthy human subjects (29±3 years, 2 males) were recruited for a proof-of-concept evaluation of the proposed sequence with translational and non-rigid motion corrections. Each

subject was imaged twice, using bSSFP (TR/TE=3.2/1.4ms, FA=70°, BW=925Hz/px) and SPGR (TR/TE=3.8/1.6ms, FA=15°, BW=500 Hz) imaging modules. To avoid artefacts observed at the liver interface, the MT preparation was of equivalent power deposition but higher off resonance frequency than that of the animal study. The modified MT preparation parameters were: MT flip angle=800˚, ΔF=3000Hz and pulse repetitions n=20. Other imaging parameters included: 3D coronal orientation, FoV=300×300×112mm3, acquired resolution= 1.4x1.4x4mm, reconstructed resolution= 1.4mm3, 100% respiratory gating efficiency, and nominal scan time of 9:02 min at 60bpm.

A data flow scheme for the image analysis pipeline is shown in **Figure 5-2B**. All datasets were reformatted to short axis orientation, using tri-linear interpolation. A 2D Gaussian filter was applied (kernel size 5 pixel, σ=3 pixel) on every slice of the MTR maps to reduce the noise and improve visualization.

Manual segmentation was performed for the three left ventricular slices (basal, mid and apical) using the American Heart Association (AHA) 16-segment model of myocardial segmentation [33].

The SPGR and bSSFP variants of the sequence were compared using the following metrics: (I) Average global MTR and average MTR per segment; (II) Spatial variation of MTR in each segment, calculated as the ratio between the standard deviation and the mean MTR (expressed as a percentage); (III) Contrast ratio (CR) between blood MTR and myocardial MTR.

MTR mean values and spatial variability were also calculated in regions of interest (ROIs) in the liver and pectoral muscle to compare with myocardial values and to assess the impact of different types of motion in the spatial variability of MTR

Based on the bSSFP results in simulations and phantom experiments, the quality of coronary vein visualization was evaluated in the SPGR datasets only, using vessel sharpness (VS) and

contrast-to-noise ratio (CNR) measurements. Translational vs non-rigid motion correction approaches were compared using a reformatted 2D representation of the 3D course of the cardiac veins [34]. VS was calculated for the posterior branch of the cardiac vein (PCV) and the great cardiac vein (GCV) from the reformatted images. VS was defined as the average intensity gradient along the edges normalized to the signal intensity of the centre of the vessel. Contrast-to-noise-ratio (CNR) between blood and myocardium was obtained from the reformatted images using:

$$CNR_{MT} = \frac{S_{Blood} - S_{Myo}}{\sigma_{Lungs}} \quad (5\text{-}9)$$

Where S_{Blood} and S_{Myo} are the mean signal intensity in blood and myocardium ROI, respectively, and σ_{Lungs} is the standard deviation in a small region of the lungs with no vessels.

Results

Numerical simulations and phantom study

Bloch simulated MTR sensitivity to B0 inhomogeneity in myocardium-like tissue with both imaging modules (bSSFP vs SPGR) are shown in **Figure 5-3A** and **Figure 5-3B**, respectively. SPGR yielded an almost flat MTR response with less than 3% variation across the studied B0 range. The bSSFP module led to generally higher MTR values but had a strong sensitivity to B0 inhomogeneity with approximately 20% variation towards the 1/2TR bands at ±150 Hz.

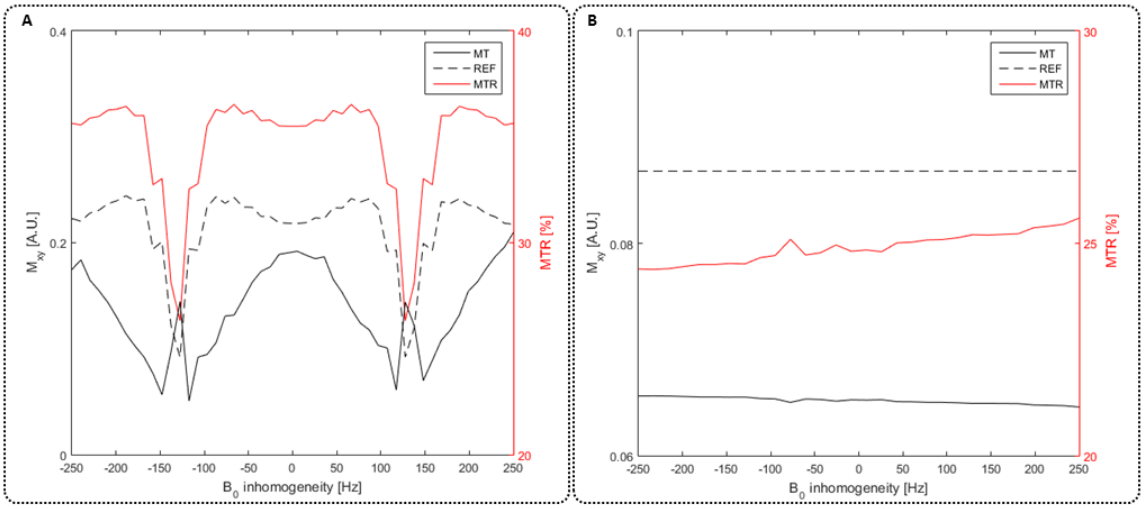

***Figure 5-3**. (A) Simulation of signal (Mxy) of the proposed sequence in myocardium-like tissue with balanced steady-state free-precession, as a function of B0 inhomogeneity. Signal from the MT and REF acquisitions (left axis) showed 'stop' bands (1/2TR) approximately at ±150Hz, while the MTR (right axis) showed a maximum reduction of up to 8% at B0 <±150Hz compared to B0=0. (B) Simulations as described in (A), except with a SPGR imaging module instead. The robustness of SPGR is shown in the flat profile obtained for the REF dataset. MTR signal is only marginally affected (<3%) throughout the B0 inhomogeneity range that was in the range of ±200Hz.*

MTR sensitivity curves with respect to the relaxation rates and exchange-related parameters are shown in **Figure 5-4**, both for SPGR and bSSFP imaging modules. MTR sensitivity to T_1^A and T_2^A using SPGR was lower than bSSFP (T_2^A: <2.3% vs <4.3%; T_1^A: <0.7% vs <2.5%, respectively) within the simulated range of myocardial relaxation rates (**Figure 5-4A**). MTR values were found to increase as a function of PSR and R (**Figure 5-4B**). PSR proved to be the major contributor to MTR, showing a near-linear dependency within the range associated with human muscle (PSR=5 to 15%). MTR dependency of the exchange rate was slowly increasing (less than 7%) within a range of R=20-70 Hz. The imaging module (bSSFP vs. SPGR) was found to have little impact on the shape of MTR as a function of *R* and *PSR*, as observed in **Figure 5-4**.

The effects of ΔF and MT flip angle on MTR values using SPGR on a 2.5% agar sample are shown in **Figure 5-5A** and **Figure 5-5B**, respectively. MTR values showed a strong non-linear frequency dependency for low ΔF (<1 kHz) and a less strong dependency at higher ΔF. The MTR dependency on the flip angle was near-linear for flip angles <800° with a stronger flip angle dependency for lower off-resonance frequencies. The phantom measurements and simulated data were in good agreement over a wide range of ΔF (>0.4 Hz and <8kHz) and MT flip angles (>360° and <800°). MTR maps obtained with bSSFP and SPGR using 3 different flip angles and fixed ΔF=400Hz are shown in **Figure 5-5C**. The MTR maps acquired with bSSFP showed multiple artefacts, likely associated with B0 inhomogeneity. The SPGR-based MTR maps were homogenous throughout but noisier than bSSFP.

Animal study

MTR decrease was found in regions associated with scar and was in good agreement with the presence of LGE in all three animals. MTR maps allowed accurate localization and visualization of scar (see **Figure 5-6**). Mean MTR values in remote myocardium were 25.1±1.7% while mean MTR values in scar were 16.8±1.9%. Voxel-to-voxel comparison with LGE showed a mean overlap of 62.5±19.2% and a mean false positive percentage of 9.6±6.0% over all animals (n=3).

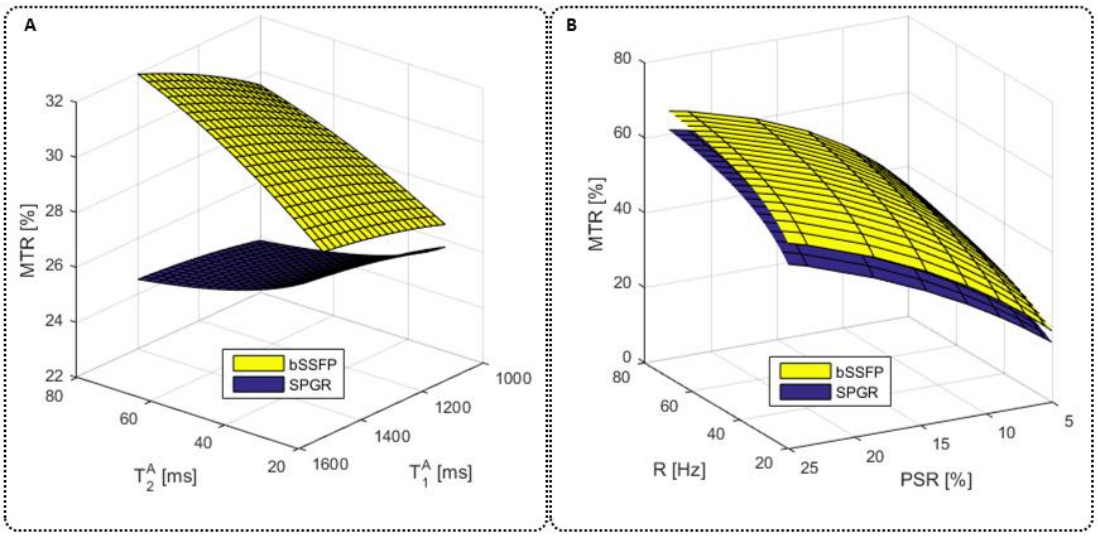

Figure 5-4*. (A) MTR sensitivity to the free pool relaxation rates, T1A and T2A, comparing bSSFP and SPGR imaging modules. SPGR showed a flatter profile with MTR variations less than 2% across a common range of relaxation rates. (B) MTR sensitivity to the exchange rate (R) and the pool size ratio (PSR), for bSSFP and SPGR. Both imaging modules showed similar increase in MTR as a function of PSR, as well as a more moderate increase in MTR as a function of R.*

Healthy subjects

The bSSFP module yielded higher CNR than SPGR (13.9±1.2, vs. 8.1±0.7, $p<0.05$) in the MT prepared datasets. CR measurements in the MTR maps (between blood and myocardium) showed no statistically significant difference between the two imaging modules (bSSFP: 2.50±0.16 vs. SPGR: 2.48±0.32, p=not statistically significant (NS)).

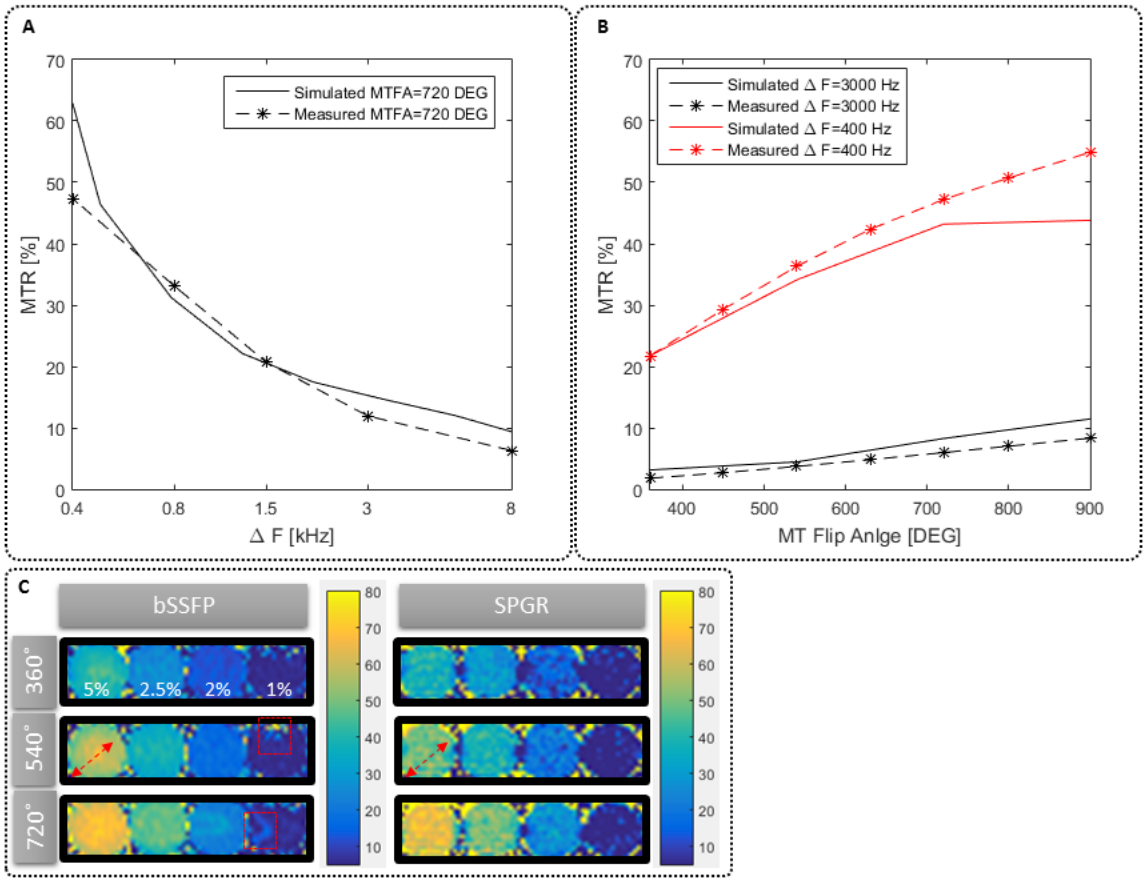

***Figure 5-5**. (A) MTR dependency as a function of the off-resonance frequency (ΔF) showed strong dependency at low ΔF, i.e. ΔF <1.5kHz, for a phantom made of 2.5% concentration of agar. (B) MTR as function of MT flip angle showed steeper slope for low ΔF (400Hz) than that of higher ΔF (3000Hz) with nonlinear dependency at high flip angles (>800˚), for a phantom made of 2.5% concentration of agar. Measured and simulated data were in good agreement in (A) and (B). (C) MTR images of the four agar-based samples (1, 2, 2.5, and 5 % concentration) with bSSFP and SPGR imaging modules using different MT Flip angles and fixed ΔF=400Hz. Red dashed arrows show an intensity gradient from centre to periphery in the bSSFP (not observed in SPGR). Likewise, red dashed squares show other artefacts seen only in the bSSFP acquisition.*

Representative MTR maps and myocardial segment mean values across all subjects using SPGR and bSSFP are shown in **Figure 5-7**. The MTR maps acquired with bSSFP demonstrated increased MTR values towards the lateral and inferior regions. This may be due to B0 inhomogeneity at the lung-myocardium interface. A typical artefact in this region is shown in

Figure 5-7 (middle column). Whole heart myocardium MTR averaged over all subjects and obtained after translational motion correction was 39.2±1.9% using bSSFP and 37.0±2.1% using SPGR. Spatial variation of MTR was 19.3±2.9% vs. 15.7±2.1% (p=0.01) for bSSFP vs. SPGR, respectively. SPGR led to reduced MTR variability between segments compared to bSSFP (8.0±2.3% vs 10.3±1.9%, p=0.07), as seen in **Figure 5-7** (right column). Mean MTR values and spatial variation did not show statistically significant difference between translational and non-rigid motion correction, as shown in ***Table 5-1***.

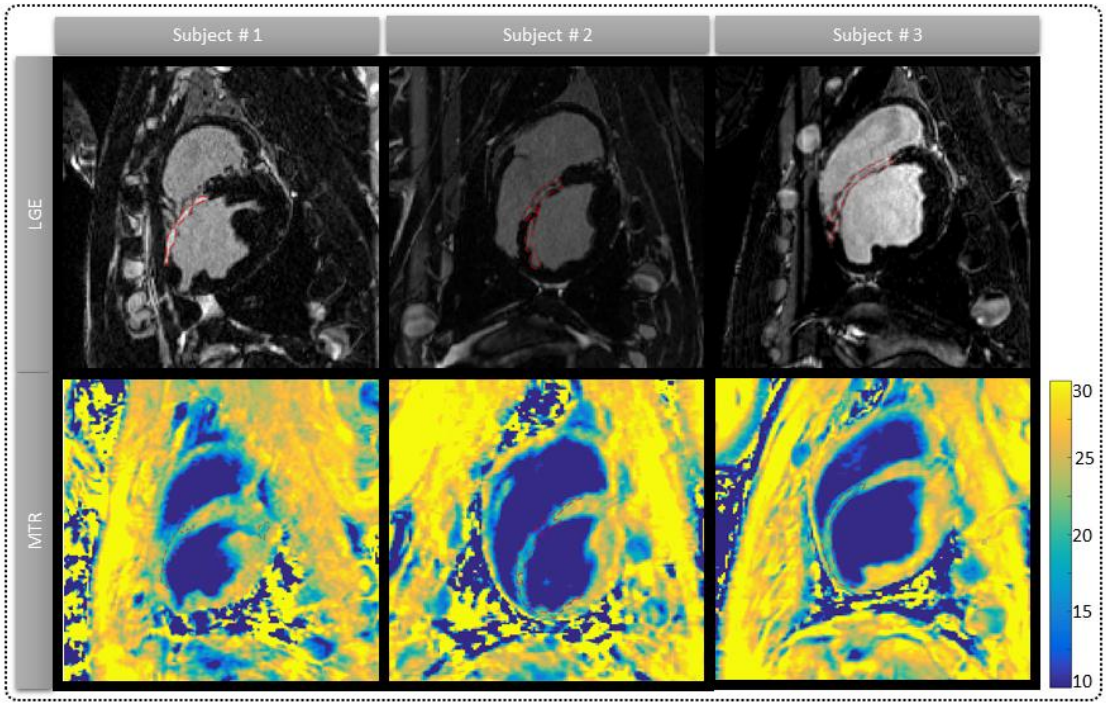

Figure 5-6*. Co-registered coronal slices comparing MTR maps with LGE images in three pigs, 6 weeks after left anterior descending artery occlusion. In all pigs, the MTR maps show significant reduction in areas that overlap with signal enhancement in the LGE images, allowing clear localization of myocardial scar from the contrast-free MTR maps alone.*

Table 5-1. *Myocardium MTR mean values and spatial variation (SD/mean). MC: motion correction; SPGR: spoiled gradient echo; bSSFP: balanced seatdy-state free-precession; ns: non statistically significant.*

Mean MTR [%]			p
Readout/MC	Translational	Non-rigid	
bSSFP	39.2±1.9	39.1±1.5	n.s.
SPGR	37.0±2.1	37.0±1.8	n.s.
p	<0.01	<0.01	

Spatial Variation [%]			p
Readout/MC	Translational	Non-rigid	
bSSFP	19.3±2.9	19.4±3.2	n.s.
SPGR	15.7±2.1	15.7±2.5	n.s.
p	<0.01	<0.01	

MTR values in pectoral muscle showed significantly reduced spatial variability compared to myocardium: MTR=43.8±1.7 (spatial variability: 9.5±3.4%, $p<0.01$) and MTR=41.0±2.4 (spatial variability: 5.8±3.6%, $p<0.01$), for bSSFP and SPGR, respectively. Liver MTR measurements showed similar spatial variability compared to myocardium, with MTR=32.3±2.9 (spatial variability: 18.4±4.3%, $p=0.4$) and MTR=29.6±3.5 (spatial variability: 15.5±0.8%, $p=0.7$), for bSSFP and SPGR, respectively. One reason for this similarity may be that the liver and the heart experience similar extent of respiratory motion.

The use of translational motion correction allowed good depiction of the PCV and GCV. The non-rigid motion correction improved visualization of the entire cardiac anatomy with respect to the translational motion correction. This was observed in an increase in vessel sharpness in the GCV (40.8 ± 2.0% vs 32 ± 2.5%, $p<0.05$) and the PCV (34.1±3.2% vs 30.0±1.7%, $p<0.05$), respectively. Three examples from representative subjects are shown in **Figure 5-8**.

Discussion

A motion corrected free-breathing 3D whole heart MTR mapping sequence was developed and successfully validated in phantoms, healthy subjects and pigs. MTR maps allowed the localization of myocardial fibrosis without the injection of a contrast agent in a pig model of myocardial infarction. Significantly lower MTR values were found in areas that corresponded with hyper intense signal on LGE. In human healthy subjects, MT prepared images reconstructed with non-rigid motion correction enabled the visualisation of the cardiac veins with vessel sharpness between 30-40% along the main cardiac veins.

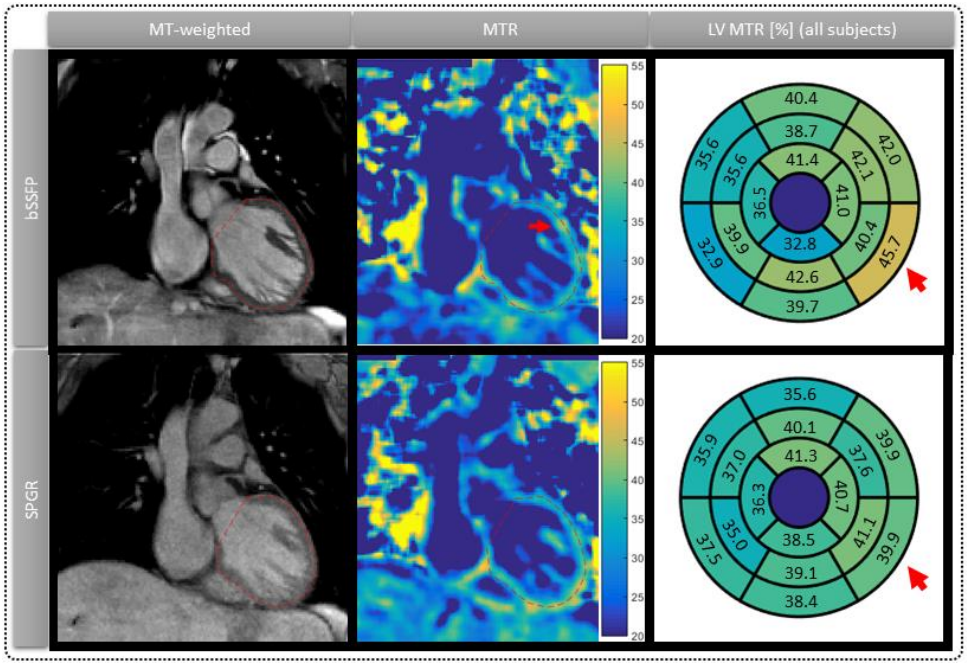

Figure 5-7*. Left and middle columns show a coronal slice in a representative healthy subject, comparing the MT-prepared dataset with the MTR map. bSSFP and SPGR imaging modules are shown in each row. The MTR map looks more homogenous with SPGR than with bSFFP, where there is an artefact in the lateral region (red arrow). The right column shows MTR mean values per segment of the American Heart Association (AHA) 16-segment model, averaged over the entire cohort of healthy subjects (n=10). The SPGR imaging module showed reduced intersegment variation compared to bSSFP (red arrows).*

MTR values found in an agar-based phantom and healthy subjects were overall consistent with Bloch simulations using a two-pool exchange model, which suggested increased MT effects associated with increased pool size ratio. Though a small discrepancy was observed in **Figure 5-5B**, at low off-resonance frequency (Δ=400Hz) and high flip angles, this was likely due to residual on-resonance saturation of the free pool not being included in the model, which seems to "inflate" the measured MTR increasingly as the flip angle raises.

In accordance with the simulations, MTR myocardial values obtained with a SPGR imaging module had less spatial variability compared to those obtained with bSSFP. This result was in agreement with a study of coronary vein imaging [18] that found that SSFP sequences were more prone to artefacts than SPGR, especially in regions surrounding deoxygenated blood (e.g. coronary veins), likely because of the spread of the resonant frequency. A similar effect was discussed in a study of coronary artery imaging [35], which highlights the challenges to find a good shimming solution for the heart due to, at least in part, cardiac and respiratory motion, blood flow, chemical shift, and susceptibility variations at air–tissue interfaces.

In healthy subjects, the spatial variability of myocardial MTR was higher than in static tissues such as pectoral muscle. This suggests that respiratory motion might have an impact on spatial variability of MTR and that residual respiratory motion may have been present in the MTR maps. While non-rigid respiratory motion correction was shown to improve vessel sharpness in the MT prepared dataset, the standard deviation of myocardial MTR was not significantly improved compared to translational motion correction only. The use of more advanced navigation techniques such as 3D iNAVs [36, 37] may help to tackle unaccounted respiratory motion. Error or bias associated with non-rigid motion within a respiratory phase may be reduced upon optimization of the size and number of bins which, in this study, were based on values previously obtained by our research group [21] for the visualization of coronary vessels. The differences between bSSFP and SPGR also suggest that field inhomogeneity may play a

role in increased spatial variability. The individual contributions of residual motion and field inhomogeneity to MTR spatial variability may be assessed with an MT-prepared breath-held single shot sequence in future studies.

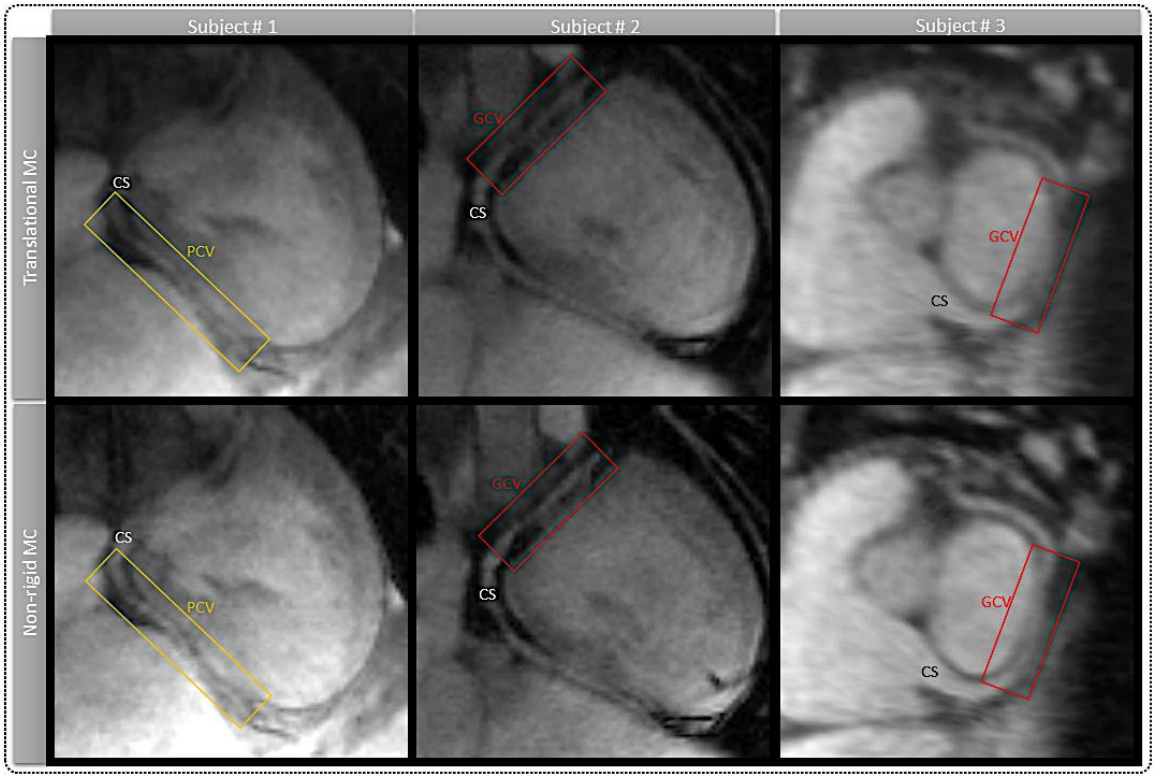

Figure 5-8*. Main coronary veins and structures such as coronary sinus (CS), the great cardiac vein (GCV) and the posterior branch of the cardiac vein (PCV) are shown in three different subjects, comparing the two motion correction (MC) approaches with a SPGR imaging module (TR/TE=3.8/1.6ms, FA=15°, BW=500 Hz). The non-rigid MC improves the visualisation with respect to the translational MC in all cases, recovering blurred features and increasing vessel sharpness.*

Six-week old scar in pigs was easily visualized and was characterized by a decrease in MTR. These results are in good agreement with previous studies which reported decreased MTR values in porcine heart four weeks after MI [38] and acute MI in humans [19, 39]. In the latter setting, it was hypothesized that the presence of oedema leads to an increase in the absolute

size of the free pool and thus a relative decrease in the MT effect and MTR. In a post-mortem study that compared MTR with histology [40], Crooijmans *et al.* found a relationship between increased MTR and fibrotic tissue, as well as a relationship between decreased MTR and inflammatory response, either due to granulocyte infiltration or oedema. In another study in pigs performed 6 weeks after coronary occlusion, Dhanjal *et al.* showed massive cellularity (stromal cells such as fibroblasts and myofibroblasts), vascularity and heterogeneity in the scarred zones [41], which might help to explain the significant decrease in MTR associated with scar in our experiments. A histopathology experiment in conjunction with MTR imaging could help to support this hypothesis in future studies

Another contrast-free approach to probe the spins with restricted motion is the T1-ρ technique, which explores spin-lattice relaxation within the rotating frame. Multiple studies have found increased T1-ρ in knee cartilage in patients with osteoarthritis due to the loss of proteoglycans and collagen (type II) integrity [42, 43], i.e. a decrease in the size of the macromolecular pool. However, 8-weeks post-MI pigs have also shown increased T1-ρ values associated with collagenous (mostly type I and III) scar [44, 45] where the size of the extracellular matrix (and macromolecular pool) is expected to have increased. In a study with acute MI patients, Muthupillai *et al.* suggested that changes in T1-ρ in the infarct zone were also associated with the loss in macromolecular content due to myocyte death [46].

At least two competing processes that may increase or decrease the size of the bound pool are at play in cardiac remodelling after MI, namely, the growth of the extra-cellular matrix and the death of protein-rich cardiomyocytes, respectively. The presence of connective tissue or edema within the fibrotic scar may also increase the size of the free pool. Our results in 6-week old (post MI) scar showed that MTR was significantly decreased, suggesting that the proposed MT preparation might be more sensitive to myocyte death rather than the known increase in collagen content associated with chronic infarct [47].

This interpretation would greatly benefit from data at various stages of the cardiac remodelling process to assess the specificity and utility of the technique in clinical practice. In an experimental mouse model, Vandsburger *et al.* reported increasing MT effects after induced MI from day 7 to 21 with a cine CEST technique [48]. To the best of our knowledge, there are no longitudinal studies in large animals that show the evolution of MTR or MT effects along the time course of the cardiac remodelling process beyond 6-8 weeks after MI.

Limitations

The conflation of bound pool size, free pool size, exchange rate and all the relaxation rates into a single parameter, i.e. the MTR, may hinder the applicability of the technique within clinical settings, where oftentimes the aetiology of the scar may be unknown or multi-pronged. In these cases, a quantitative approach using a multi-parameter MT model could be more appropriate.

The number of off-line post-processing steps and setup parameters may slow down widespread clinical adoption, however, more automated or end-product frameworks that apply many of these same techniques are currently being developed by the present research group and others [49, 50].

The small number of pigs used in this study was a limitation, however, the results showed consistency across all three cases. Other limitations included the relatively long scan time and anisotropic resolution in the human subjects. The anisotropic resolution affected image quality, specifically when reformatting to orientations other than coronal. The resolution was compromised in order to maintain a short scan time (<10 min) that was clinically appealing. Future work might benefit from isotropic resolution paired with an accelerated acquisition framework.

Conclusions

We have developed a non-contrast high-resolution 3D sequence that allows calculation of magnetization transfer ratio (MTR) maps for the assessment of myocardial scar and visualization of cardiac veins across the whole heart. Good agreement was found between MTR and LGE in a small cohort of pigs with six-week-old scar. Further studies are warranted to fully characterize the potential of MT for imaging of myocardial fibrosis.

REFERENCES

1. Lopez, K., et al., *Contrast-free high-resolution 3D magnetization transfer imaging for simultaneous myocardial scar and cardiac vein visualization.* MAGMA, 2020.
2. Bruder, O., et al., *Myocardial scar visualized by cardiovascular magnetic resonance imaging predicts major adverse events in patients with hypertrophic cardiomyopathy.* J Am Coll Cardiol, 2010. **56**(11): p. 875-87.
3. Kelle, S., et al., *Prognostic value of myocardial infarct size and contractile reserve using magnetic resonance imaging.* J Am Coll Cardiol, 2009. **54**(19): p. 1770-7.
4. Klem, I., et al., *Assessment of myocardial scarring improves risk stratification in patients evaluated for cardiac defibrillator implantation.* J Am Coll Cardiol, 2012. **60**(5): p. 408-20.
5. Shetty, A.K., et al., *Cardiac magnetic resonance-derived anatomy, scar, and dyssynchrony fused with fluoroscopy to guide LV lead placement in cardiac resynchronization therapy: a comparison with acute haemodynamic measures and echocardiographic reverse remodelling.* Eur Heart J Cardiovasc Imaging, 2013. **14**(7): p. 692-9.
6. Flett, A.S., et al., *Evaluation of techniques for the quantification of myocardial scar of differing etiology using cardiac magnetic resonance.* JACC Cardiovasc Imaging, 2011. **4**(2): p. 150-6.
7. Mewton, N., et al., *Assessment of myocardial fibrosis with cardiovascular magnetic resonance.* J Am Coll Cardiol, 2011. **57**(8): p. 891-903.
8. Kim, R.J., et al., *Myocardial Gd-DTPA kinetics determine MRI contrast enhancement and reflect the extent and severity of myocardial injury after acute reperfused infarction.* Circulation, 1996. **94**(12): p. 3318-26.
9. Kanda, T., et al., *Gadolinium-based Contrast Agent Accumulates in the Brain Even in Subjects without Severe Renal Dysfunction: Evaluation of Autopsy Brain Specimens with Inductively Coupled Plasma Mass Spectroscopy.* Radiology, 2015. **276**(1): p. 228-32.
10. Laurent, D., et al., *Quantitative and qualitative assessment of articular cartilage in the goat knee with magnetization transfer imaging.* Magn Reson Imaging, 2001. **19**(10): p. 1279-86.
11. Phinikaridou, A., et al., *In vivo magnetization transfer and diffusion-weighted magnetic resonance imaging detects thrombus composition in a mouse model of deep vein thrombosis.* Circ Cardiovasc Imaging, 2013. **6**(3): p. 433-440.
12. Wang, C., et al., *Magnetization transfer ratio mapping of intervertebral disc degeneration.* Magn Reson Med, 2010. **64**(5): p. 1520-8.
13. Wolff, S.D. and R.S. Balaban, *Magnetization transfer contrast (MTC) and tissue water proton relaxation in vivo.* Magn Reson Med, 1989. **10**(1): p. 135-44.
14. Wolff, S.D., J. Eng, and R.S. Balaban, *Magnetization transfer contrast: method for improving contrast in gradient-recalled-echo images.* Radiology, 1991. **179**(1): p. 133-7.
15. McDaniel, J.D., et al., *Magnetization transfer imaging of skeletal muscle in autosomal recessive limb girdle muscular dystrophy.* J Comput Assist Tomogr, 1999. **23**(4): p. 609-14.
16. Stoeck, C.T., et al., *Whole heart magnetization-prepared steady-state free precession coronary vein MRI.* J Magn Reson Imaging, 2009. **29**(6): p. 1293-9.
17. Botnar, R.M., et al., *Improved coronary artery definition with T2-weighted, free-breathing, three-dimensional coronary MRA.* Circulation, 1999. **99**(24): p. 3139-48.

18. Nezafat, R., et al., *Coronary magnetic resonance vein imaging: imaging contrast, sequence, and timing.* Magn Reson Med, 2007. **58**(6): p. 1196-206.
19. Weber, O.M., et al., *Assessment of magnetization transfer effects in myocardial tissue using balanced steady-state free precession (bSSFP) cine MRI.* Magn Reson Med, 2009. **62**(3): p. 699-705.
20. Germain, P., et al., *A dual flip angle 3D bSSFP magnetization transfer-like method to differentiate between recent and old myocardial infarction.* J Magn Reson Imaging, 2018. **47**(3): p. 798-808.
21. Prieto, C., et al., *Highly efficient respiratory motion compensated free-breathing coronary MRA using golden-step Cartesian acquisition.* J Magn Reson Imaging, 2015. **41**(3): p. 738-46.
22. Henningsson, M., et al., *Whole-heart coronary MR angiography with 2D self-navigated image reconstruction.* Magn Reson Med, 2012. **67**(2): p. 437-45.
23. Cruz, G., et al., *Highly efficient nonrigid motion-corrected 3D whole-heart coronary vessel wall imaging.* Magn Reson Med, 2017. **77**(5): p. 1894-1908.
24. Bracewell, R., et al., *Affine theorem for two-dimensional Fourier transform.* ELECTRONICS LETTERS-IEE, 1993. **29**: p. 304-304.
25. Modat, M., et al., *Fast free-form deformation using graphics processing units.* Comput Methods Programs Biomed, 2010. **98**(3): p. 278-84.
26. Batchelor, P.G., et al., *Matrix description of general motion correction applied to multishot images.* Magn Reson Med, 2005. **54**(5): p. 1273-80.
27. Sled, J.G. and G.B. Pike, *Quantitative imaging of magnetization transfer exchange and relaxation properties in vivo using MRI.* Magn Reson Med, 2001. **46**(5): p. 923-31.
28. Morrison, C., G. Stanisz, and R.M. Henkelman, *Modeling magnetization transfer for biological-like systems using a semi-solid pool with a super-Lorentzian lineshape and dipolar reservoir.* J Magn Reson B, 1995. **108**(2): p. 103-13.
29. Ropele, S., et al., *Method for quantitative imaging of the macromolecular 1H fraction in tissues.* Magn Reson Med, 2003. **49**(5): p. 864-71.
30. Stikov, N., et al., *Bound pool fractions complement diffusion measures to describe white matter micro and macrostructure.* Neuroimage, 2011. **54**(2): p. 1112-21.
31. Portnoy, S. and G.J. Stanisz, *Modeling pulsed magnetization transfer.* Magn Reson Med, 2007. **58**(1): p. 144-55.
32. Tschabrunn, C.M., et al., *A swine model of infarct-related reentrant ventricular tachycardia: Electroanatomic, magnetic resonance, and histopathological characterization.* Heart Rhythm, 2016. **13**(1): p. 262-73.
33. Cerqueira, M.D., et al., *Standardized myocardial segmentation and nomenclature for tomographic imaging of the heart. A statement for healthcare professionals from the Cardiac Imaging Committee of the Council on Clinical Cardiology of the American Heart Association.* Circulation, 2002. **105**(4): p. 539-42.
34. Etienne, A., et al., *"Soap-Bubble" visualization and quantitative analysis of 3D coronary magnetic resonance angiograms.* Magn Reson Med, 2002. **48**(4): p. 658-66.
35. Deshpande, V.S., S.M. Shea, and D. Li, *Artifact reduction in true-FISP imaging of the coronary arteries by adjusting imaging frequency.* Magn Reson Med, 2003. **49**(5): p. 803-9.
36. Luo, J., et al., *Nonrigid Motion Correction With 3D Image-Based Navigators for Coronary MR Angiography.* Magn Reson Med, 2017. **77**(5): p. 1884-1893.
37. Powell, J., et al., *CMRA with 100% navigator efficiency with 3D self navigation and interleaved scanning.* Journal of Cardiovascular Magnetic Resonance, 2014. **16**(1): p. O8.

38. van Oorschot, J. *Detection of myocardial infarcts without contrast agent injection: Comparison of spin-lock with magnetization transfer MR imaging*. in *ISMRM 24th Annual Meeting & Exhibition*. 2016. Singapore.
39. Stromp, T.A., et al., *Gadolinium free cardiovascular magnetic resonance with 2-point Cine balanced steady state free precession.* J Cardiovasc Magn Reson, 2015. **17**: p. 90.
40. Crooijmans, H.J., et al., *Cardiovascular magnetization transfer ratio imaging compared with histology: a postmortem study.* J Magn Reson Imaging, 2014. **40**(4): p. 915-9.
41. Dhanjal, T.S., et al., *Massive Accumulation of Myofibroblasts in the Critical Isthmus Is Associated With Ventricular Tachycardia Inducibility in Post-Infarct Swine Heart.* JACC Clin Electrophysiol, 2017. **3**(7): p. 703-714.
42. Li, X., et al., *In vivo T(1rho) and T(2) mapping of articular cartilage in osteoarthritis of the knee using 3 T MRI.* Osteoarthritis Cartilage, 2007. **15**(7): p. 789-97.
43. Witschey, W.R., et al., *T1rho MRI quantification of arthroscopically confirmed cartilage degeneration.* Magn Reson Med, 2010. **63**(5): p. 1376-82.
44. van Oorschot, J.W., et al., *Endogenous assessment of chronic myocardial infarction with T(1rho)-mapping in patients.* J Cardiovasc Magn Reson, 2014. **16**: p. 104.
45. Witschey, W.R., et al., *Rotating frame spin lattice relaxation in a swine model of chronic, left ventricular myocardial infarction.* Magn Reson Med, 2010. **64**(5): p. 1453-60.
46. Muthupillai, R., et al., *Acute myocardial infarction: tissue characterization with T1rho-weighted MR imaging--initial experience.* Radiology, 2004. **232**(2): p. 606-10.
47. Hervas, A., et al., *Inhomogeneity of collagen organization within the fibrotic scar after myocardial infarction: results in a swine model and in human samples.* J Anat, 2016. **228**(1): p. 47-58.
48. Vandsburger, M., et al., *Cardio-chemical exchange saturation transfer magnetic resonance imaging reveals molecular signatures of endogenous fibrosis and exogenous contrast media.* Circ Cardiovasc Imaging, 2015. **8**(1).
49. Usman, M., et al., *Free breathing whole-heart 3D CINE MRI with self-gated Cartesian trajectory.* Magn Reson Imaging, 2017. **38**: p. 129-137.
50. Di Sopra, L., et al., *An automated approach to fully self-gated free-running cardiac and respiratory motion-resolved 5D whole-heart MRI.* Magnetic resonance in medicine, 2019. **82**(6): p. 2118-2132.

Chapter 6 : Quantitative Magnetization Transfer Imaging for Non-Contrast Enhanced Detection of Myocardial Fibrosis

Quantitative Magnetization Transfer Imaging for Non-Contrast Enhanced Detection of Myocardial Fibrosis

Karina López[1], Radhouene Neji[1,2], Aurelien Bustin[1], Imran Rashid[1], Reza Hajhosseiny[1], Shaihan J Malik[1], Rui Pedro AG Teixeira[1], Reza Razavi[1], Claudia Prieto[1], Sébastien Roujol[1], René M Botnar[1]

[1]*School of Biomedical Engineering and Imaging Sciences, King's College London, UK*

[2]*MR Research Collaborations, Siemens Healthcare Limited, Frimley, UK*

Submitted to *Magnetic Resonance in Medicine* as a Full Paper. Minor layout changes have been made to the published manuscript to fit the logical structure of the present report.

Abstract

Purpose: To develop a novel gadolinium-free model-based quantitative magnetization transfer (qMT) technique to assess macromolecular changes associated with myocardial fibrosis.

Methods: The proposed sequence consists of a two-dimensional breath-held dual shot interleaved acquisition of five MT-weighted (MTw) spoiled gradient echo images, with variable MT flip angles and off-resonance frequencies. A two-pool exchange model and dictionary matching were used to quantify the pool size ratio (PSR) and bound pool T2 relaxation (T_2^B). The signal model was developed and validated using 25 MTw images on a Bovine Albumin Serum (BSA) phantom and in-vivo human thigh muscle. A protocol with 5 MTw images was optimized for single breath-hold cardiac qMT imaging. The proposed sequence was tested in 10 healthy subjects and 5 patients with myocardial fibrosis and compared to late gadolinium enhancement (LGE).

Results: PSR values in the BSA phantom were within the confidence interval of previously reported values (concentration 10% BSA=5.9±0.1%, 15% BSA=9.4±0.2%). PSR and T_2^B in thigh muscle were also in agreement with literature (PSR=10.9±0.3%, T_2^B=6.4±0.4us). In ten healthy subjects, global left ventricular PSR was 4.30±0.65%. In patients, PSR was reduced in areas associated with LGE (remote: 4.68±0.70% vs fibrotic: 3.12±0.78 %, n=5, p<0.002).

Conclusion: In vivo model-based qMT mapping of the heart was performed for the first time, with promising results for non-contrast enhanced assessment of myocardial fibrosis.

Keywords: Magnetization transfer, quantitative mapping, cardiac, fibrosis, gadolinium-free.

Author's contributions

Lopez: study design, implementation of MT sequence in Siemens pulse programming environment, acquisition of all data related to phantom and human experiments, implementation of part of the image reconstruction and signal model code, image reconstruction and dictionary matching, analysis and interpretation of all data and drafting of manuscript.

Neji: study design, acquisition of data and critical revision.

Bustin: implementation of part of the image reconstruction code and critical revision.

Rashid: acquisition of data related to patients and critical revision.

Hajhosseiny: acquisition of data related to patients, manual segmentation of ROIs and critical revision.

Malik: implementation of part of the signal model code and critical revision.

Teixeira: acquisition of data related to the phantom experiments and critical revision.

Razavi: critical revision.

Prieto: conception and design of data acquisition and critical revision.

Roujol: design and critical revision.

Botnar: conception and overall study design, data acquisition, interpretation of data and critical revision.

Introduction

The presence of scar following myocardial infarction has been shown to have important prognostic implications for patients with ischemic cardiomyopathy. Late gadolinium enhancement (LGE) MRI is the gold standard [1] for the assessment of myocardial replacement fibrosis, targeting the enlarged extracellular space with gadolinium-based contrast agents, so that an enhanced signal allows the localization of fibrotic tissue [2]. LGE is a highly effective approach for focal scar visualization and quantification, however LGE does not allow diffuse fibrosis quantification as it visualizes contrast differences between normal and diseased myocardium. More recently, there has been an interest in quantification of local and diffuse fibrosis using T1 mapping with [3] or without [4] gadolinium-based contrast agents (GBCAs), yet there remain questions about its sensitivity and specificity [5]. Also, the use of gadolinium-based contrast agents may be associated with an increased risk of nephrogenic systemic fibrosis in patients with pre-existing renal dysfunction [6], and there have been recent reports of long-term retention of some GBCAs in the brain [7]. Therefore, the development of quantitative and gadolinium-free approaches for assessment of myocardial fibrosis may be highly beneficial.

Magnetization Transfer (MT) is an endogenous MR contrast that can be exploited to identify tissue with high macromolecular content. MT has been previously considered as a gadolinium-free alternative to LGE [5], showing to be sensitive to an increase in collagen [8] and thus with a potential for the assessment of myocardial scar [9]. In part due to its increased spin density

and slow molecular motion, dephasing of the transverse magnetization is very efficient within large macromolecules, which typically translates into extremely short T2 relaxation times, on the order of a few microseconds, thus making them impossible to detect by standard MRI techniques. However, in a seminal study, Wolff and Balaban [10] observed a signal loss in the water peak of up to a 30% in the kidney after off-resonance radiofrequency irradiation. Such preparation selectively saturates the extremely short T2 species of macromolecules while sparing the free-water spins, because of the broader resonance spectrum of macromolecules. Thus, the observed signal loss is due to the magnetization transfer (or exchange) that occurs between water spins bound to macromolecules and those that can move more freely.

One approach to quantify the MT effect is to obtain a ratio of the MT contrast change, by acquiring one image with MT contrast and one without it. Previous studies have explored the use of magnetization transfer ratio (MTR) for gadolinium-free assessment of chronic or acute myocardial fibrosis. In-vivo studies have shown reductions of the MT effects associated with both acute [11, 12] and over 10-month old myocardial infarction (MI) [13]. A post-mortem study [9] found correlation between increased MTR and fibrous tissue in histology, while some areas of decreased MTR were associated with inflammatory granulocyte infiltration at a microscopic level. This shows that MTR results can be complex to interpret without knowledge of the dynamics of the free pool, as it can also be affected by edema and inflammation [14]. A quantitative approach to MT that separately factors in the contributions of the free pool and the bound pool, using an exchange signal model, is therefore highly desirable in the assessment of patients with acute, subacute or chronic cardiac remodeling and without the need for contrast injection.

In this study, we developed a cardiac model-based quantitative MT mapping approach (qMT) that seeks to study the contribution of the free pool and the bound pool in myocardial scar. This is achieved by using off-resonance preparation pulses and a two-pool exchange signal model

to quantify the myocardial pool size ratio (PSR) and bound pool T2 (T_2^B). The pool size ratio accounts for most of the signal but it relates to both the free and the bound pools, however, in combination with T_2^B (only bound pool) it may be possible to separately characterize the role of the bound and free pools in the cardiac remodeling process.

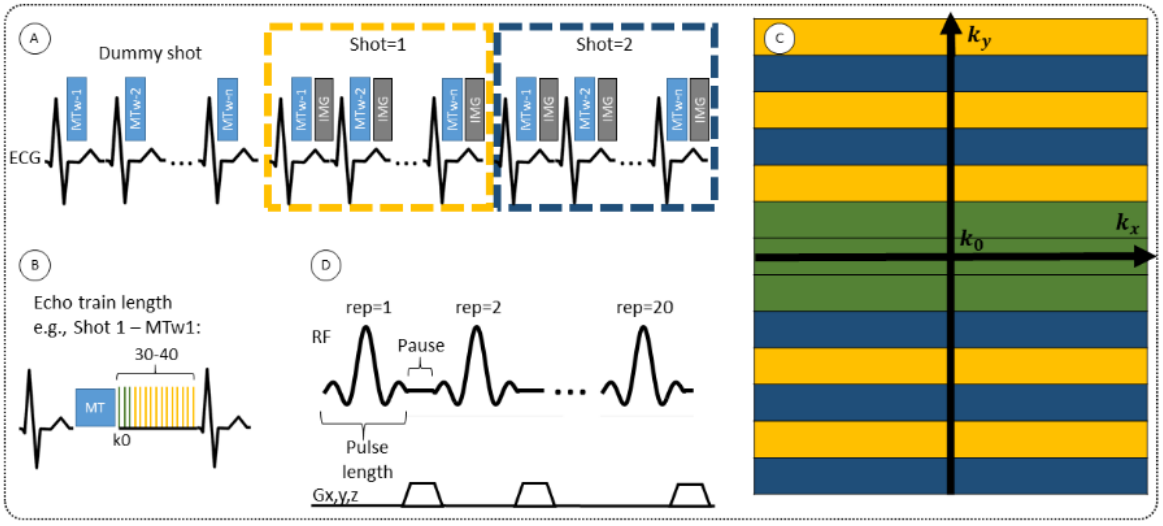

Figure 6-1. *(A) A scheme of the acquisition of "n" (e.g, n=5) interleaved MT-weighted 2D slices in 2 shots (i.e. each MT-weighted k-space dataset is acquired in two heartbeats), including a 'dummy' shot made up of "n" heartbeats. A train of MT preparation pulse and an imaging module are played out in every heartbeat. (B) A scheme of the imaging module applied for each image on each shot, consisting of 30-40 profiles (echo train length). (C) A scheme of the acquisition of k-space in two shots (yellow/blue) with a centric profile, the center of k-space being sampled on every shot. (D) A scheme of the MT preparation module, consisting of a train of 20 identical Sinc-shaped pulses at a given ΔF offset frequency and flip angle, with spoiler gradients played out during a brief pause period between each pulse.*

Methods

A sequence for contrast-free quantitative 2D myocardial scar imaging is proposed, consisting of five MT-weighted (MTw) spoiled gradient echo (SPGR) images, with variable MT

preparations (flip angle and off-resonance frequency), as shown in **Figure 6-1** and **Table 6-1**. To enable data acquisition in a single breath-hold with an acquisition window of <140ms to minimize cardiac motion the five MT contrasts are acquired in one dummy shot and two imaging shots (i.e. in fifteen heartbeats). Novel model-based MT mapping (qMT) is performed using a two-pool exchange signal model and dictionary matching to quantify the pool size ratio and bound pool T2. The signal model was developed and first validated using 25 MTw images on a Bovine Albumin Serum (BSA) phantom and in-vivo human thigh muscle, which was considered the reference standard. A protocol with only 5 MTw images was later designed to allow for breath-held cardiac imaging, using an optimization algorithm to determine the sequence parameters (MT flip angle and off-resonance frequency) that maximized the determination coefficient of the match (see equation (6-4)). The proposed myocardial qMT was tested in 10 healthy subjects and 5 patients with myocardial fibrosis. The study was approved by our local research ethics committee and written informed consent was obtained from all subjects. An overview of the proposed framework is shown in **Figure 6-2**, including image acquisition, reconstruction and post processing, dictionary generation and matching, and image analysis. Each of these steps is described hereafter.

***Table 6-1**. Main sequence parameters for the MT preparation and imaging modules. SPGR: spoiled gradient echo, ΔF: frequency offset*

MT Prep pulses			SPGR Readout	
MTw1	ΔF offset	1.5 kHz	Echo Train Length	36
	MT flipangle	540 °	# Shots	2
MTw2	ΔF offset	4.0 kHz	Bandwidth	500 Hz
	MT flipangle	360 °	TE/TR	1.9/3.8 ms
MTw3	ΔF offset	0.9 kHz	Resolution	2.0x2.0 mm2
	MT flipangle	630 °	Slice Thick.	8 mm
MTw4	ΔF offset	2.9 kHz	Flip Angle	15 °
	MT flipangle	450 °	Accel.	GRAPPA
MTw5	ΔF offset	2.1 kHz	Accel. Factor	2
	MT flipangle	800 °		
All	Bandwidth	268 Hz		
	Length	20.48 ms		
	Repetitions	20		

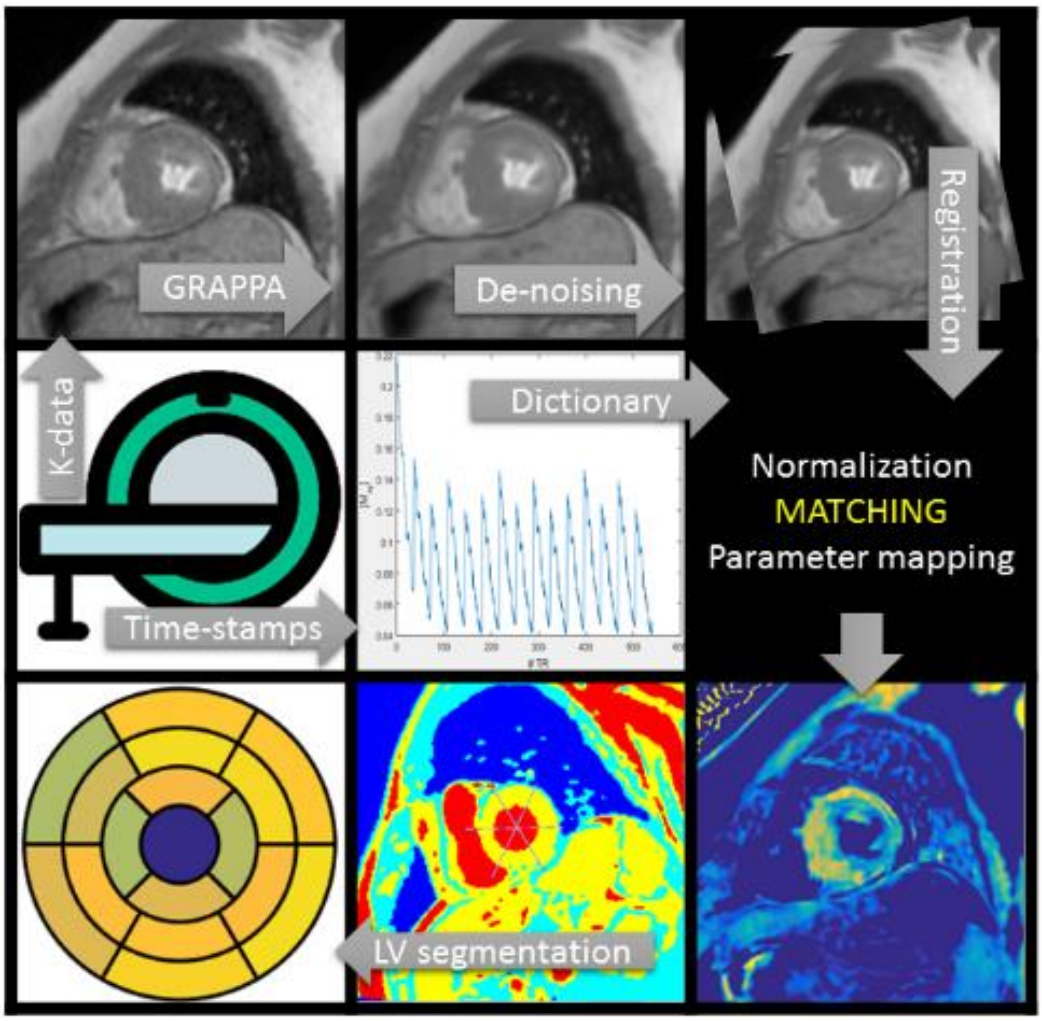

***Figure 6-2**. A diagram or data flow chart of the present study is shown. Acquired MR data is reconstructed with GRAPPA, followed by low-rank based denoising and registration to align the different MT-weighted images. A dictionary is generated informed by literature free pool relaxation rates, the MR sequence (read-out) time stamps and other fundamental sequence parameters (TR, TE, flip angle, number of segments, etc.). After MR data and dictionary entries are self-normalized, a least-squares matching is performed (on a pixel-wise basis) to obtain the qMT parameter maps. Manual segmentation of the left-ventricle (LV) is performed on subjects for comparison and analysis.*

Signal model

Let us consider a system where most spins have generally free motion (pool: A) and are at thermal equilibrium with a net magnetization M_0^A, while a small fraction of them is bound to macromolecules (pool: B) and have net magnetization M_0^B. It has been shown that for such system, the magnetization exchange between both pools can be represented by the so-called binary spin-bath model [15], a specific case of the Bloch-McConnell equations [16] where the size of pool $A \gg B$. A steady-state solution to this set of coupled differential equations requires typically long RF preparation (> few seconds), however, a transient approach using Extended Phase Graphs (EPG) simulation has been recently proposed [17].

The EPG framework analyses the system's magnetization response in terms of its configuration states [18], which can be described as Fourier Transforms (FT) of the spatial magnetization components. In this space, the net magnetization dephasing caused by spatially-variant gradients over an entire ensemble of spins within a volume V is uniquely described by k, making computation much more efficient. The interactions with RF pulses, gradients, and the effects of relaxation and exchange are all represented by simple matrix operators. The EPG-X method extends the classic framework, to include a fourth configuration state [17], i.e. $[\tilde{F}_+, \tilde{F}_-, \tilde{Z}_A, \tilde{Z}_B]^T$, where $\tilde{Z}_B$ is as a FT of the bound pool's longitudinal magnetization, M_Z^B. The evolution of $\tilde{Z}_B$ is coupled to $\tilde{Z}_A$ via first order forward and backward exchange rates: k_f (or kf) and k_B. Because the time scale of the decay of transverse magnetization in the bound pool is very short (<20μs), it is assumed to decay instantaneously. For this reason, only the exchange between longitudinal magnetizations is considered into the model. Another consequence of this instantaneous decay is that for the bound pool, RF excitation can be totally described as an instant saturation of the longitudinal magnetization at a certain rate W, proportional to RF power deposition, ω_1^2, and the bound pool's line absorption profile, g_B,

$$W(2\pi\Delta) = \pi\,{\omega_1}^2 g_B(2\pi\Delta, T_2^B) \tag{6-1}$$

where Δ is the offset frequency of the irradiation. In the case of a shaped RF pulse, equation *(6-1)* can be generalized [19], integrating over time for the duration of the pulse so that a time average of the saturation rate is obtained: $\bar{W}$. The absorption profile g_B depends on Δ with a super-Lorentzian form, typical of partially ordered materials and semi-solids where the dipolar Hamiltonian does not average to zero over time. The width of the super-Lorentzian form is characterized by the T2 of the bound pool, T_2^B, and can be obtained as [20]:

$$g_B(2\pi\Delta, T_2^B) = \sqrt{2/\pi}\; T_2^B \int_0^{\pi/2} \frac{e^{-2\frac{(2\pi\Delta\, T_2^B)^2}{(3cos^2\theta-1)^2}}}{|3cos^2\theta - 1|}\, sin\theta d\theta \tag{6-2}$$

To further simplify the calculation of $\bar{W}$, the time-variant amplitude of the RF pulse in Eq. *(6-1)* can be approximated by a time-constant value using Ramani's continuous wave power-equivalent formula [21].

In our ECG-triggered cardiac implementation, each MT preparation pulse is simulated by the RF transition operator $\boldsymbol{T}$ acting onto the longitudinal states $Z_n = [\tilde{Z}_A, \tilde{Z}_B]$ as,

$$\boldsymbol{T} = \begin{bmatrix} 1 & 0 \\ 0 & e^{-\bar{W}\,\tau_{RF}} \end{bmatrix} \tag{6-3}$$

That is, the effect on the bound pool is modelled by the average of the RF saturation rate $\bar{W}$ times the length of the RF pulse τ_{RF}, while the longitudinal magnetization of the free water pool is not disturbed. This assumption is based on the use of low bandwidth Sinc shaped MT pulses, high off-resonance frequencies (>900 Hz) and simulation data reported in Supporting Information (Figure S1).

After the transition operator, the evolution along the entire length of the pulse (plus any waiting/pause time between pulses) is governed by exchange and relaxation [17]:

$$\dot{F}_n = \begin{bmatrix} -\frac{1}{T_2^A} & 0 \\ 0 & -\frac{1}{T_2^A} \end{bmatrix} F_n \tag{6-4}$$

$$\dot{Z}_n = \begin{bmatrix} -\frac{1}{T_1^A} - k_f & k_B \\ k_f & -\frac{1}{T_2^B} - k_B \end{bmatrix} Z_n$$

Where $F_n = [\tilde{F}_+, \tilde{F}_-]$ represents the free pool's transverse configuration states. A spoiled gradient echo (SPGR) acquisition immediately follows a train of MT preparation RF pulses, as described in [17]. Exchange and relaxation operators are applied again during waiting time between heartbeats.

MRI sequence

A number of n MT-weighted images are acquired with an interleaved acquisition in 3xn consecutive heartbeats (as shown in **Figure 6-1A**, for n=5) on a 1.5T scanner (Magnetom Aera, Siemens Healthcare, Erlangen, Germany). During the first n dummy heartbeats, MT preparation pulses are played out without any imaging readout, to achieve a (pseudo) steady state at the beginning the following 2xn heartbeats, when the dual shot image acquisition is performed. Each shot is made up of two modules performed in one heartbeat: (1) an MT preparation train of off-resonance RF pulses, and (2) a spoiled gradient echo (SPGR) imaging module which collects only half of the entire k-space data. The interleaved acquisition aims at reducing (respiratory motion induced) mis-alignment between the MT weighted images. The MT preparation module consists of a train of 20 identical Sinc-shaped RF pulses with a given frequency offset and flip angle. The imaging module consists of a SPGR sequence with

Cartesian k-space sampling, centric reordering and 2-fold accelerated GRAPPA acquisition [22].

In a BSA phantom and in-vivo human thigh muscle the sequence was applied with n=25 different MT-weighted images. An acquisition protocol with n=5 was used for cardiac in-vivo imaging, due to the time restriction imposed by subjects' ability to hold their breath. Different combinations of off-resonance frequencies and flip angles were investigated for the 5 MT pre-pulses and the combination that resembled best the results obtained with 25 MT pre-pulses was used for all subsequent experiments.

Image reconstruction and post-processing

The MTw images are reconstructed inline using the scanner software (Syngo E11C, Siemens Healthcare, Erlangen, Germany). In order to reduce noise, correct for motion misalignment between images due to variable heartrate and imperfect breath-holding, and generate a normalized input for the dictionary matching, we performed three off-line (MATLAB v. R2017b) post-processing steps:

I. De-noising : all MTw images are jointly de-noised using a multi-contrast patch-based low-rank de-noising technique [23], which has been recently proposed to accelerate quantitative mapping without significant loss in accuracy. This technique exploits the redundancy of local and non-local features within the images and along the contrast dimension in order to build a high-order, low-rank tensor made of similar image patches, which can then be de-noised using singular value decomposition and truncation.
II. Registration: all MTw images are motion aligned using an affine image registration procedure [24].

III. Normalization: each (magnitude) MTw image is divided by the pixel-wise overall mean signal value along the contrast (MTw) dimension. This process generates a normalized input for the dictionary matching.

Dictionary matching

A dictionary of possible signal evolutions is created using the model described before. Subject-specific ECG time stamps are incorporated in the signal simulation to to make the model less sensitive to heart-rate variations.

Each entry in the dictionary is a vector of as many elements as MTw images. After computation, magnitude entries are normalized by the mean of all its elements. The maximum size of a single dictionary (with 3-free parameters: k_f, T_2^B and PSR) was about 42k entries.

The vector difference between measured data and every dictionary entry is computed, for every pixel, to compute the parametric maps. The entry with highest determination coefficient R^2 is matched,

$$R^2 = 1 - \frac{\sum_{i=1}^{n}(m_i - f_i)^2}{\sum_{i=1}^{n}(m_i - \bar{m})^2} \quad (6\text{-}5)$$

where m_i is measured data point for the i-th MT weighting (for a given pixel), f_i is the corresponding i-th fitted value, $\bar{m}$ is the mean of all MT weighted data points (for a given pixel) and n is number of MTw acquisitions.

Optimization and Validation in phantoms

First, a BSA phantom consisting of 4 samples of different albumin concentrations (5%, 8%, 10% & 15%) was made following the description by Koenig *et al.* [25]. The goal of this BSA study was to optimize a sequence with 5 MT weightings for in-vivo myocardial applications. The optimization algorithm had the following steps:

I. First, a *reference* protocol was implemented (protocol 25-MTw hereon) with readout and MT preparation modules as described in Table 1, except for the number of images and MT weightings: 25 images were obtained with MT weightings at 5 different frequency Δ offsets log-spaced between 1 and 7.7 kHz, and 5 different MT flip angles (FA), linearly spaced between 360 and 800 deg.

II. A high-resolution (free pool) T1 map was obtained using balanced steady state free precession (bSSFP) MOLLI [26] (scheme 5(3)3, resolution= 0.75x0.75x4 mm^3, BW=770Hz, GRAPPA acceleration factor=2, FA=35˚, TE/TR=1.76/2.7ms) and a corresponding high-resolution (free pool) T2 map was obtained with a T2-prepared bSSFP sequence (TE_{T2prep} = 0, 25 and 50 ms, resolution=0.78x0.78x4 mm^3, BW=778 Hz, GRAPPA acceleration factor=2, FA=70˚, TE/TR=1.59/2.7ms) using a 2-parameter fitting model [27].

III. *Reference* PSR (range=0-15, step=0.1, [%]),T_2^B (range=5-20, step=0.5, [us]) and k_f (range=2-10, step=1, [Hz]) parameter maps were estimated using all 25 MTw images. The exchange rate k_f was then fixed at its mean fitted value and a second dictionary match was created with only two degrees of freedom: PSR and T_2^B (ranges and steps as before).

IV. Using only two degrees of freedom, PSR and T_2^B mean (ROI) values were calculated for all possible combinations of only 5 MT weightings. The combinations that produced PSR and T_2^B values within one standard deviation of the previously obtained *reference* values were shortlisted.

V. The best combination of 5 MT weightings was selected from the shortlist by maximizing the coefficient of determination of the match, as defined in equation *(6-5*). Mean values and standard deviation were calculated from a sample of eighty random 5 MTw combinations to assess robustness against FA and Δ variation.

In-vivo validation in human thigh muscle

In the second part of this study, a validation of the model in-vivo in human thigh muscle was performed in order to test the sequence in a molecular environment closer to that of the myocardium, i.e., collagen and other proteins present in human muscle, to obtain qMT parameters that could be used to guide our target cardiac study. The 25-MTw protocol (as described above) was acquired in a healthy subject and compared to the prospective acquisition of the proposed 5-MTw protocol. The parameter k_f (k_f=4.2Hz) was estimated from the 25-MTw protocol selecting a muscle ROI and using a dictionary with 3 degrees of freedom: PSR (range=0-15, step=0.1, [%]),T_2^B (range=5-20, step=0.5, [us]) and k_f (range=1-5, step=0.5, [Hz]). PSR and T_2^B parameter maps were then created using a dictionary with two degrees of freedom (k_f fixed to the obtained value): PSR (range=0-15, step=0.1, [%]), T_2^B (range=2-20, step=2, [us]). The parameters maps from the 5-MTw protocol were obtained with the same parameter ranges, fixed inputs and degrees of freedom.

In-vivo cardiac imaging study: healthy subjects and patients

Ten healthy subjects (age: 30±3 y, 7 female) and five patients with myocardial fibrosis (age: 62±10, all male) underwent MRI with the 5-MTw protocol (prior to contrast administration in patients). MT preparation pulse parameters and imaging parameters are described in **Table 6-1** and were derived from the optimization described before.

Patients undergoing a clinically indicated cardiac MR (CMR) at our institution were selected based on the likelihood of having ischemic or non-ischemic myocardial scar (including previous imaging findings, clinical history and age). The only exclusion criterion was the presence of a pacemaker (due to the associated likelihood of imaging artefacts). All patients followed the standard Cardiac MR (CMR) protocol at our institution, including cine, T1 mapping, early gadolinium enhancement (EGE) and LGE imaging, in addition to the proposed

sequence. T2 mapping was additionally performed in two patients (P1 and P4). The characterization of the patients' heart disease/etiology in this study were obtained from the CMR report, based on the entirety of the imaging findings and additional information made available by the referring clinician.

The proposed sequence was acquired in short axis, in patients prior to contrast agent injection, with the following relevant parameters: ECG-triggered acquisition with mid-diastolic data acquisition of <140ms, number of slices=10-14, spatial resolution=2x2mm (interpolated to 1.4x1.4mm), slice thickness=8mm, and scanning time approximately 15s per slice. In patients, phase sensitive inversion recovery (PSIR) LGE acquisition was performed 12-15 minutes after injection of Gadovist contrast agent for comparison purposes. LGE imaging parameters included a bSSFP sequence with TE/TR=1.2/3.0, flip angle=45˚, short-axis stack, variable field of view, in plane spatial resolution=1.4x1.4 mm2, slice thickness 8 mm and number of slices=10-14.

Parameter maps were created using a dictionary with one degree of freedom: PSR (range=0-15, step=0.02, [%]). Free pool relaxation rates were fixed to mean reported values for healthy myocardium: T_2^A=53ms [28, 29], and T_1^A=950ms [30]. Exchange rate k_f was fixed to the value found for human thigh muscle (**Table 6-2**). A fixed value of T_2^B was used in parameter mapping (from human thigh muscle, **Table 6-2**) and a dictionary of T_2^B (range=2-20, step=2, [us]) was used in ROI-based calculations.

The 5-MTw protocol was repeated three separate times over four mid-ventricular slices in one non-scar patient to assess reproducibility of measurements.

Statistics

Manual segmentation of the myocardium was performed over one basal, one mid and one apical slices in healthy subjects, using one of the denoised MTw images (MTw #3, Δ=0.9kHz,

FA=630°) to create a mask, following the American Heart Association (AHA) 16-segment model [31]. The mask was then applied onto the parameter maps and measurements of mean and standard deviation were taken for each AHA segment and for every subject.

Delineation of scar and remote ROIs in patients (in PSR and LGE slices) was performed by two independent readers (one blinded to LGE) with experience in CMR. A third experienced reader provided qualitative assessment and advice. PSR mean and standard deviation values per ROI were measured for each patient and averaged between readers. Total ROI areas were also recorded and percentage area differences (Δarea) between corresponding LGE and PSR slices are reported. Co-registration of PSR and LGE slices was done manually/visually since the number of slices and the field of view did not always coincide. MT/PSR and LGE images were acquired with a delay of up to 20 minutes (due to contrast injection), often causing patient mis-alignment, movement of arms, or the need to increase the LGE's field of view beyond the limits of the MT acquisition.

PSR measurements in pectoral muscle ROIs within the field of view (FOV) of every apical slice were obtained both in healthy subjects and patients.

Results

Phantom and in-vivo model validation

Using the 25-MTw protocol, mean values of PSR for the BSA 15% and BSA 10% phantom vials were comparable with previous reports [32, 33], at PSR=9.4±0.2% and PSR=5.9±0.7, respectively (**Table 6-2**). There was good agreement between PSR and T_2^B mean values measured with the 25-MTw and the 5-MTw protocols, except for a small reduction (BSA15%: 25pt=9.4±0.2% vs 5pt=8.0±1.5%) in the PSR value for the BSA 15% vial with the 5-MTw acquisition. T_2^B values were similar for all vials and both protocols. **Table 6-2** shows parameter

measurements for all phantom vials and protocols. For the 25-MTw protocol, k_f was almost constant across all samples, with a mean value k_f=3.0±1.2Hz.

***Table 6-2**. MT parameter measurements in BSA phantom and human thigh muscle (muscle ROI). PSR: pool size ratio, T2B: T2 of the bound pool, KF: forward exchange rate, T1A: T1 of the free pool, T2A: T2 of the free pool, BSA: Bovine Serum Albumin*

	BSA 15%		**BSA 10%**		**BSA 8%**		**BSA 5%**		**Thigh Muscle**		**unit**
	25pt	5pt	25pt	5pt	25pt	5pt	25pt	5pt	25pt	5pt	
Fixed parameters											
T1A	848	848	1052	1052	1251	1251	1503	1503	1022	1022	ms
T2A	77	77	112	112	157	157	238	238	52	52	ms
KF	3.0	3.0	3.0	3.0	3.0	3.0	3.0	3.0	4.2	4.2	Hz
Free parameters											
PSR	9.4±0.2*	8.0±1.5*	5.9±0.1	5.9±0.7	4.5±0.1	4.4±0.7	2.9±0.1	3.0±0.4	10.9±0.3	10.8±0.8	%
T2B	6.7±0.7	6.8±0.5	6.5±0.9	6.8±0.5	6.6±0.5	6.8±0.4	6.7±0.4	6.8±0.5	6.4±0.4	6.5±0.7	µs

*p<0.05

PSR and T_2^B thigh muscle parameter maps generated with protocol 25-MTw and 5-MTw are shown in **Figure 6-3**A. Mean values of PSR (PSR=10.9±0.3%), T_2^B (T_2^B=6.4±0.4us) and k_f (k_f=4.2±1.2Hz) estimated from the 25-MTw protocol were found within the range of previously reported in-vivo thigh muscle studies [34]. No statistical significance between mean PSR and T_2^B values was found when comparing the 25-MTw and the 5–MTw protocols, as shown in **Table 6-2**.

PSR estimation was robust against the choice of MT flip angle (FA=0-800˚) and ΔF (0-7.7kHz) with mean PSR=10.9±0.1 [%] at 95% confidence interval (CI), median 11.1 [%] and range 10.0 to 11.4 [%], as shown in **Figure 6-3**B. The estimation of $T_2^B$was found slightly more dependent on variation of MT flip angle and ΔF, with mean T_2^B=6.5±0.2 [us] at 95% CI, median 6.0 [us] and range 4.0 to 8.0 [us].

The number of free and fixed parameters for the model-based dictionary was determined based on simulations. The sensitivity to free pool relaxation rates (T_1^A, T_2^A) of the proposed sequence is shown in a simulated matching experiment in **Figure 6-4**A, where a (fixed) typical

myocardial signal vector (PSR=4%, T_2^B=8.4us, k_f=4Hz, T_1^A=1050ms, T_2^A=50ms) was matched with a range of fixed T_1^A/T_2^A combinations ($T_1^A = 900 - 1300$ ms, $T_2^A = 40 - 60$ ms), resulting in a PSR match error under 4% for the entire range of combinations. The same myocardial signal vector was also matched with a range of fixed T_2^B/k_f combinations, as shown in **Figure 6-4**B. The error in PSR match was up to ≈12% for ±1us error in T_2^B. On the other hand, the error in PSR match was below 5% for any k_f values similar and above those found in muscle (e.g. k_f=4.9 Hz[33]).

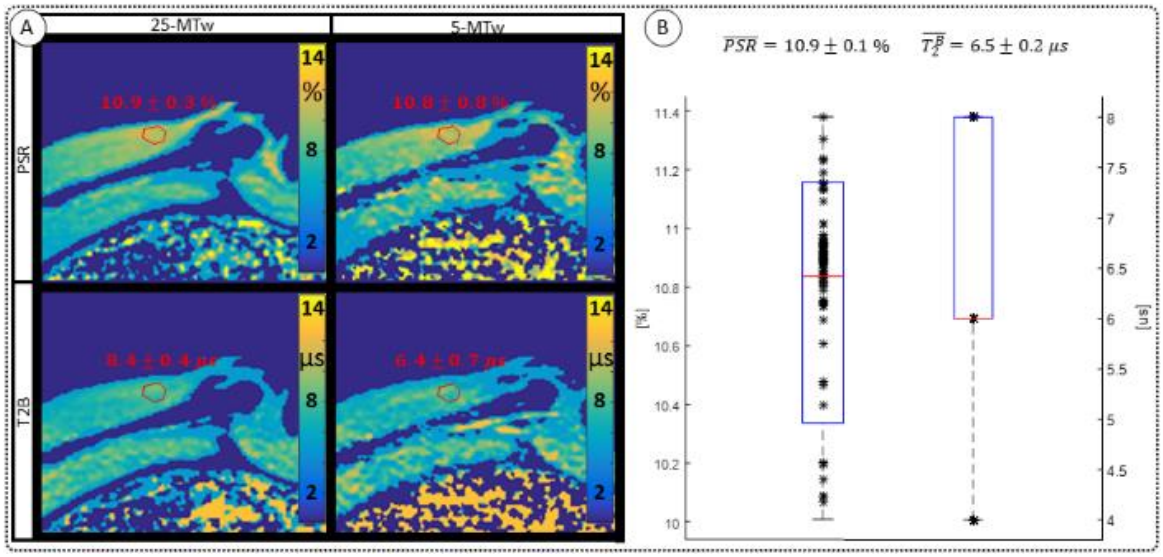

Figure 6-3*. (A) Comparison of PSR and T_2^B maps obtained in thigh muscle of a healthy subject using two qMT protocols with either 25 images or 5 images (sagittal view). Good agreement is observed between the 25-MTw and 5-MTw measurements for both phantom and in-vivo scans. (B) Assessment of robustness of estimation of PSR (left) and T_2^B (right) against variation of flip angle (FA=0-800˚) and off-resonance frequency (ΔF=0-7.7kHz) for 80 random 5MTw combinations in a thigh muscle ROI. Box plots show median (red), interquartile range (blue) and full range (black) statistics.*

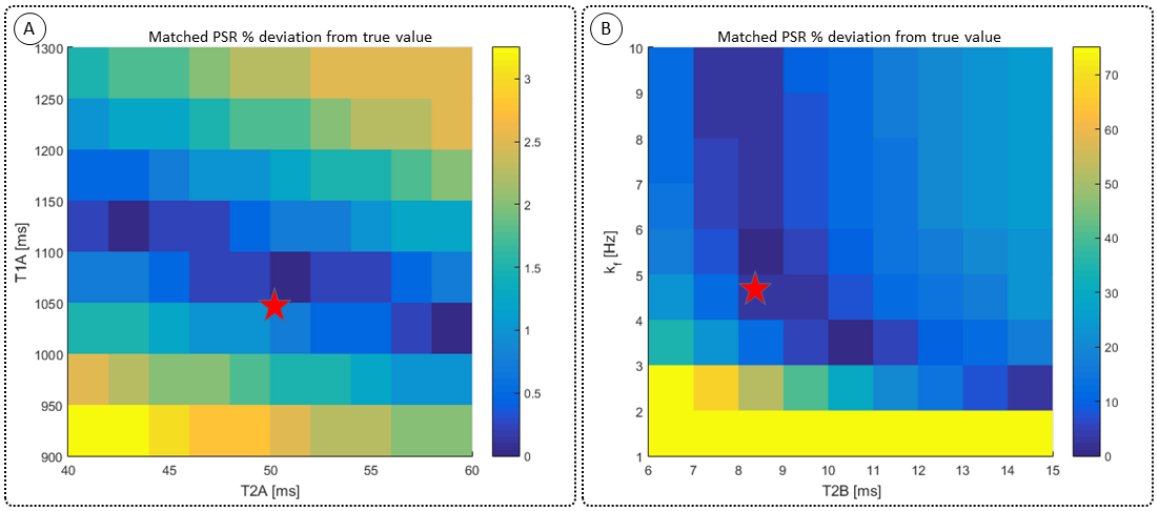

***Figure 6-4**. A (fixed) simulated signal vector (PSR=4%, T_2^B=8.4us, k_f=4Hz, T_1^A=1050ms, T_2^A=50ms) is matched with a range of fixed T_1^A/T_2^A combinations ($T_1^A = 900 - 1300$ ms, $T_2^A = 40 - 60$ ms), showing extremely low sensitivity (<3%) to changes in both T_1^A and T_2^A. (B) The same signal vector is matched with a range of k_f/ T_2^B combinations, showing moderate sensitivity to T_2^B, while k_f sensitivity is limited to k_f<4Hz (here, the true value).*

Cardiac study: healthy subjects

Mapping of myocardial T_2^B showed large and non-smooth spatial variation, at times outside the expected range for muscle, 5-15 us [15, 35]. However, matching the average signal of a mid-septum myocardial ROI resulted in $T_2^B = 6.6 \pm 1.3\ us$ (n=10), which is within the expected range and comparable to other muscle tissue, e.g., thigh muscle (see above). For this reason, PSR parameter maps were calculated with a fixed T_2^B (and k_f) using the values that were validated in thigh muscle (see above).

Denoised images showed an average difference of 1.2% in the mean value of the signal in a mid-ventricular septal region of interest (ROI) compared with original (non-denoised) images. The regularization parameter (σ) was set at $\sigma = 4 \cdot 10^{-3}$ to obtain the best compromise between accuracy and precision (see **Figure 6-5A**). This resulted in an average difference in the

estimation of PSR of 0.6 [PSR %] while the standard deviation was reduced from 2.6 to 0.4 [PSR %] in the same ROI (see **Figure 6-5B-E**). All images presented hereon were denoised following the procedure described earlier and all parameter measurements presented are derived from denoised images.

In healthy subjects, global left ventricular PSR was 4.30±0.65%. Average intra-segment PSR standard deviation was 0.65 [%] and inter-segment standard deviation was 0.54 [%]. Average pectoral muscle PSR was 6.92±0.21% (**Table 6-3**). PSR maps generally had spatially uniform appearance with a small tendency of reduced PSR towards anterior and antero-septal regions. One basal slice and one apical slice are shown for two representative healthy subjects in **Figure 6-6A** myocardial segment bull's eye plot of PSR mean values and standard deviation (respectively) averaged across all subjects is also shown in **Figure 6-6(E,F)**.

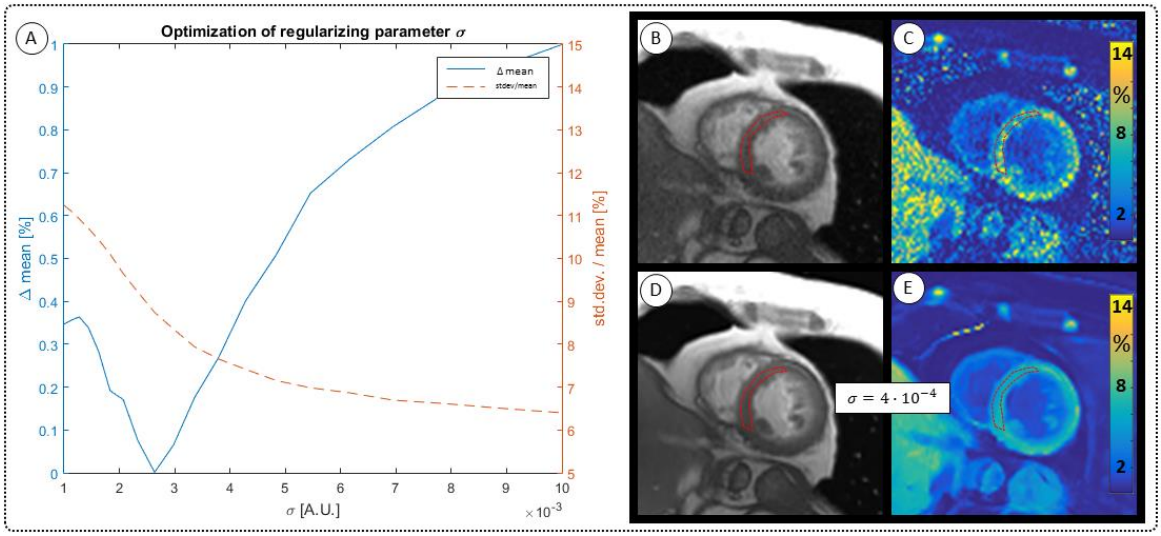

Figure 6-5*. Optimization of image de-noising and impact on PSR estimation. (A) Left axis shows the difference between the mean values of original and de-noised images ('accuracy' line) for a myocardial ROI with varying regularization level σ, while the right axis shows the ratio between the mean value and standard deviation of the same ROI ('precision' line) for each regularized image. (B-C) Example mid-ventricular slice showing an original (non-denoised) MT weighted image and the obtained PSR parameter map, respectively. (D-E) Denoised MT weighted image and its respective PSR parameter map, at optimal regularization level σ=4x10^{-3}.*

In the reproducibility experiment, the standard deviation of mean PSR from mid-ventricular septum over all measurements (n=12) was 0.33 [PSR %], a deviation of 5.4% from the mean value.

Eight out of ten healthy subjects had stable heartrate under 62 bpm. Two healthy subjects had stable heartrate between 71 and 82 bpm. The PSR maps of the latter did not show a statistically significant difference from the global (all-subjects) average.

Whole body Specific Absorption Rate (SAR) estimation was below 0.15 W/kg or 10% of the normal controlled standard in all volunteers.

***Table 6-3**. PSR measurements in pectoral muscle, remote and scar myocardium in patients and remote myocardium in healthy subjects*

	slice #	Gender	Age	Remote PSR [%]	Core scar PSR [%]	LGE/PSR Δarea [%]	Pectoral muscle PSR [%]	Scar transmurality
Healthy subjects, n=10								
Mean			30±3	4.30± 0.65			6.92±0.21	
Patients P1-P3								
P1	1	M	65	4.84±0.15	2.78±0.16	11.61±0.79	6.52±0.66	near transmural
	2			4.03±0.92	1.78±0.07	6.74±1.16		
	3			3.44±0.71	2.66±0.09	10.41±1.09		
P2	1	M	64	4.75±0.30	3.19±0.17	45.65±4.57	6.88±0.16	75% subendocardial
	2			4.93±0.45	3.13±0.12	19.20±15.56		
P3	1	M	59	5.85±0.59	3.93±0.09	41.17±5.75	7.08±0.07	transmural
Mean			**63±3**	**4.64±0.82***	**2.91±0.71***	**22.47±16.78**	**6.83±0.28**	
Patients P4-P5								
P4	1	M	48	4.91±0.22	3.11±0.69	12.70±6.83	5.18±0.09	50-75% subendocardial
P5	1	M	75	4.72±0.81	4.35±0.56	39.82±1.97	7.45±0.31	focal area
Mean (all patients)			**62±10**	**4.68±0.70***	**3.12±0.78***		**6.62±0.87**	

*p<0.002

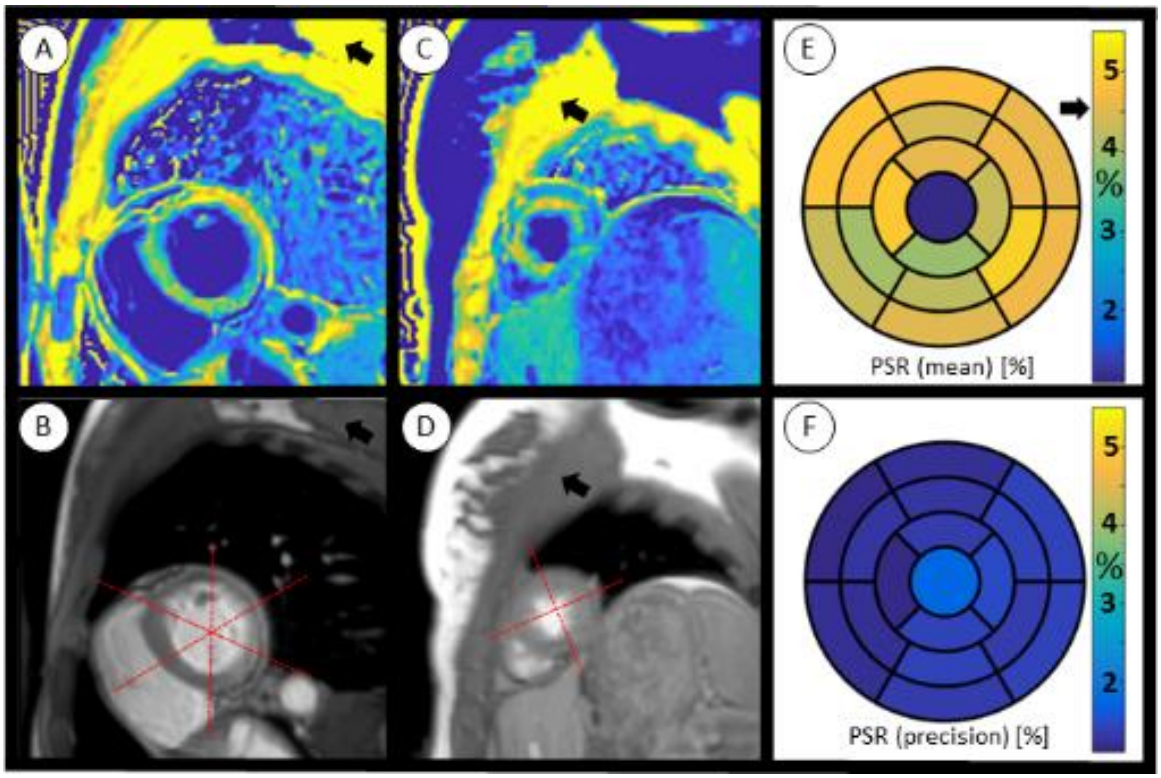

***Figure 6-6**. (A-B) PSR map and one of the corresponding MTw images (Δ=0.9kHz, FA=630˚) of a myocardial (short-axis) basal slice of healthy subject (H1, female, 28 years). (C-D) PSR map and one of the corresponding MTw images (Δ=0.9kHz, FA=630˚) of a myocardial (short-axis) apical slice of healthy subject (H2, female, 37 years). Some areas of skeletal muscle used for measurements are shown (black arrows). (E,F) Mean and standard deviation of PSR across the myocardium, respectively, averaged across all healthy subjects (n=10), measured using manual segmentation based on the American Heart Association model (29). Overall mean left ventricle PSR was 4.30± 0.65 %, see black arrow in (E).*

Cardiac study: patients

Four patients (P1-P4) showed myocardial enhancement on LGE images, with findings indicative of previous myocardial infarction. One patient, P5, showed a focal area of epicardial

to mid-wall myocardial enhancement consistent with a non-ischemic scar distribution, possibly due to prior myocarditis.

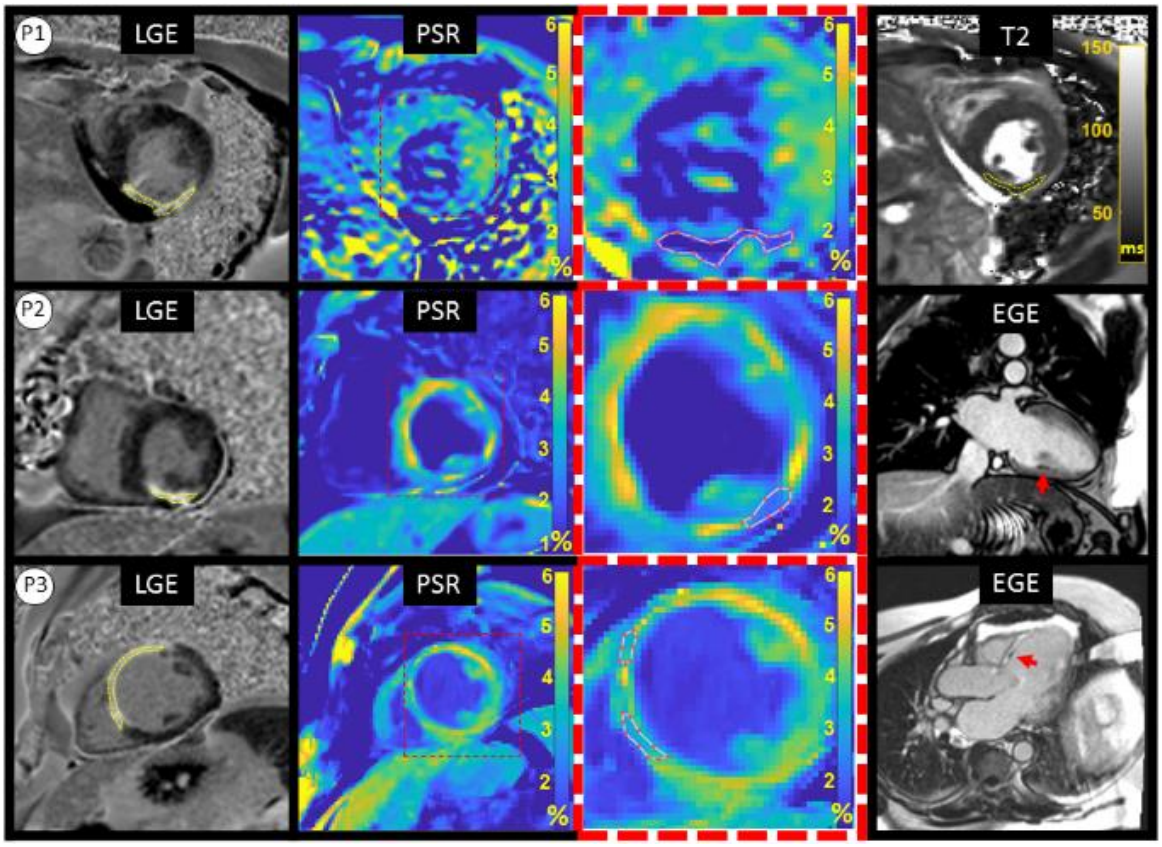

***Figure 6-7**. The left and left-middle columns show LGE and PSR co-registered short-axis slices for each patient, the middle right column represents a zoomed PSR frame centered in the left ventricle and the far right column represents additional imaging related to inflammation or micro-vascular obstruction. (Upper row) Patient P1 mid-ventricle slice with near transmural LGE enhancement (yellow dashed line) of the inferior and lateral walls and normal T2 (far right). (Middle Row) Patient P2 basal slice with sub-endocardial LGE enhancement (yellow dashed line) in the basal infero-septal, inferior and infero-lateral segments. Micro-vascular obstruction observed in (two-chamber view) early gadolinium enhancement (EGE), far right. (Bottom row) Patient P3 mid-ventricular slice with transmural LGE enhancement in mid-distal anterior and anterior septal segments, local micro-vascular obstruction observed in EGE (three-chamber view, far right). All patients present clear reduction in PSR values in correlation with LGE.*

P1 showed evidence of lipomatous metaplasia in the lateral wall and previous transmural myocardial infarction of the inferolateral wall (left circumflex coronary artery territory) of unknown age (**Figure 6-7**, P1), however, T2 maps demonstrated non-elevated myocardial T2 values within the region of scar (infarct ROI: T2=48.6±4.3, remote T2=49.2±2.7) suggesting that the infarct is not acute/subacute.

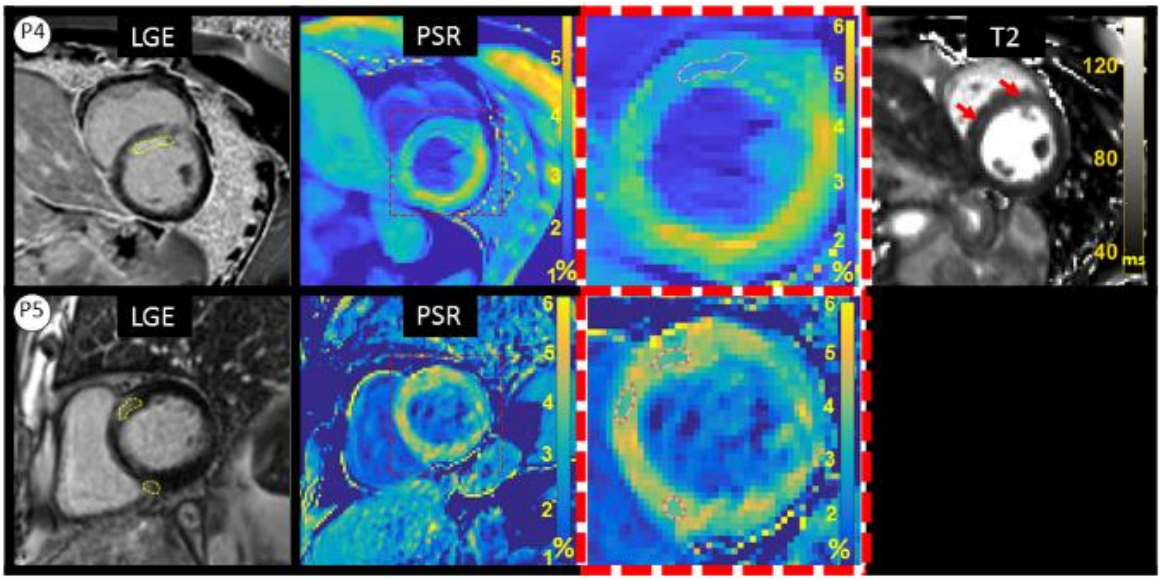

Figure 6-8*. Far left and left-middle columns show LGE and PSR co-registered short-axis slices for each patient, the right middle column represents a zoomed PSR frame centered in the left ventricle and the far right column represents additional imaging related to inflammation. (Upper row) Patient P4 with sub-endocardial LGE enhancement (yellow dashed line) in mid antero-septal, anterior and infero-septal segments. T2 values were increased in ROI associated with LGE enhancement (T2 map, short-axis slice, far right). (Bottom row) Patient P5 basal slice with mid-myocardial focal LGE enhancement in anterior and inferior segments (yellow dashed line). Both patients present moderate reduction in PSR values in correlation with LGE.*

P2 showed evidence of transmural myocardial infarction in the right coronary artery (RCA) territory on LGE (**Figure 6-7**, P2) and stress-induced perfusion abnormalities with preserved viability in the left anterior descending (LAD) territory (not shown in Figure). Also, the early phase (i.e., early gadolinium enhancement, EGE) showed evidence of microvascular

obstruction (MVO) in the inferior wall. P2 had had coronary artery bypass grafting (CABG) with saphenous vein graft to RCA approximately 8 years earlier. T2 weighted images were not available.

P3 showed evidence of previous transmural myocardial infarction in the LAD (**Figure 6-7Figure 6-7**, P3, far left) and localized microvascular obstruction at basal anterior septum in the early phase (**Figure 6-7**, P3, far right). T2 weighted images were not available.

P4 had a subacute presentation with a near transmural infarct in the territory of the first diagonal (D1) coronary artery with corresponding signal increase in T2 maps (infarct ROI: T2=59.6±3.4, remote T2=46.2±2.3), on a background of a prior chronic infarct in the LAD territory.

P5 showed evidence of a non-ischemic distribution of LGE (mid-wall, septal) in a patient with sarcoidosis. T2 weighted images were not available.

ROIs likely to correspond with scar in PSR maps were identified by both readers in 3 patients (P1-P3) and ROIs drawn by the blinded reader are shown in **Figure 6-7**. One reader also identified ROIs likely to correspond with scar in patients P4 and P5, shown in **Figure 6-8**. Small areas of slightly reduced or increased PSR were also observed, which did not correlate with LGE.

PSR measurements and LGE/PSR area differences for each patient are reported in **Table 6-3**. All patients showed reduced PSR in myocardial regions likely to be scar tissue that corresponded with location and extent of LGE enhancement. Average remote myocardium PSR in patients P1-P3 was 4.64±0.82% and average core scar PSR was 2.91±0.35% ($p<0.002$), giving an average difference of 1.7% PSR. Similar results were found when including all patients P1-P5 (4.68±0.70% vs 3.12±0.78%, for remote and core scar, respectively). Average LGE/PSR scar area difference in patients P1-P3 was 22.47±16.78% (range 6.74 to 45.65%), while values for P4-P5 fell within a similar range (12.7%-39.8%).

Average pectoral muscle PSR in all patients was similar to the same measurement in healthy subjects (6.62±0.87% vs. 6.92±0.21%, p=NS).

Discussion

PSR values obtained from multiple measurements within a single subject were reproducible and heartrate differences among healthy subjects did not appear to affect the PSR maps. To the best of our knowledge, this is the first time model-based quantitative MT mapping has been performed in the human heart. Furthermore, the PSR variations among healthy subjects (i.e., 0.65% PSR) were less than half the average difference between core scar and remote measurements in patients (i.e., 1.7% PSR), which showed that the precision for measuring remote myocardium in-vivo with the proposed sequence may be sufficient for identifying at least some types of fibrosis.

In our cardiac study, ROIs were identified by two readers in patients with strong likelihood of having ischemic scar (P1-P3). On the other hand, in patients with a likelihood of recent infarction or non-ischemic scar (P4-P5), ROIs were identified by only one of the readers (not blinded to LGE). Despite moderate dispersion or heterogeneity of the signal in the myocardium in all subjects, the findings showed evidence of reduced MT saturation effects in infarct areas in all patients. It is possible that some of the PSR differences (within the infarcted myocardium) in P1 vs P2-P4 can be explained by chronicity, since the evidence of MVO (in P2 and P3) or increased T2 (in P4) is suggestive of at least subacute presentation. However, additional studies may be needed to determine all the physical/physiological factors driving the imaging contrast.

Our results did not show evidence of an increase of the bound pool in the presence of replacement fibrosis/collagen, i.e., in the chronic MI patients. On the contrary, a reduction of the MT effects was observed, which is consistent with findings in chronic myocardial infarction in rats by Scholz *et al.* [36], findings of fibrosis in end stage renal disease (ESRD) patients by

Stromp *et al.* [37], and reports from Duan *et al.* [13] in 15-month (average) post MI patients using a hybrid T1/MT –weighted sequence. The proposed sequence may present advantages over Duan *et al.* and Stromp *et al.* in terms of quantification of the bound pool and potential specificity to fibrosis, since the cited approaches rely on combining the MT contrast with T1 and/or T2 weighting.

The observed reduction of the MT effects may be due to cardiac re-modelling factors, other than collagen deposition, having a more substantial effect in the MT signal, such as necrosis and the associated loss of mitochondrial protein content [38], or an increase in water mobility within collagenous scar [39]. Other tissue characterization techniques based on the excitation of the bound pool, such as T1ρ, have found similar results in chronic MI, with reported increased relaxation times in 8-week old scar in swine [39] and diffuse myocardial fibrosis in patients [40]. In the T1ρ model used for articular cartilage degeneration studies, an increase in relaxation time is interpreted as a consequence of loss in collagen concentration [41-43] which would correspond to a reduction in PSR. Although changes in T1ρ within protein solutions or soft tissue are typically attributed to chemical exchange and dipolar coupling between water and bound protons, Witschey *et al.* [39] hypothesizes that an increase in matrix's water mobility may also be responsible for T1ρ changes in the case of collagenous scar.

One of the main challenges of a cardiac MRI study is to find the right compromise between spatial resolution, SNR and motion. In this study, we decided to minimize the cardiac motion by keeping the acquisition window relatively short (<140ms), thereby resulting in a dual shot sequence (each MT weighted image is acquired in two heartbeats) with 5 MT weightings with an acceptable breath-hold duration of 15 consecutive heartbeats, which was tolerated by most patients. However, other sources of patient motion during the acquisition and/or errors in the co-registration of the MT weighted images may have been associated with areas of slightly increased or reduced PSR which did not correlate with LGE findings in patients. Also, a low

SNR may have hindered pixel-wise estimation of T_2^B in the myocardium, given that the weight of T_2^B effects on the signal is far more subtle than the weight of PSR. This is supported by the fact that ROI-based estimation, with intrinsically higher SNR, gave results within the expected range. This led us to choose a fixed value for T_2^B to estimate PSR in the myocardium. It is to note, however, that giving a fixed (non-myocardium) value to T_2^B may have introduced a bias in the PSR measurements, as shown in our simulations. Further studies are needed to enable reproducible mapping of T_2^B in the myocardium. Specifically, since the estimation of T_2^B in our thigh muscle model was also found to depend moderately on variations of MT flip angle and ΔF.

It is possible that T_2^B maps of the heart may be obtained by reducing the weight of noise and motion artefacts in the fitting. This may be approached in two different ways: increasing the number of images (weightings) and/or significantly increasing the SNR. The SPGR readout that was used in this study is relatively robust against B0 and B1 inhomogeneity at 1.5T and was therefore our choice to avoid bias in parameter fitting, however the TR is long and was not practical to pursue a single shot acquisition that would have allowed more MT weightings within a single breath-hold, as it would have led to an acquisition window of ≈280ms. Lower spatial resolution or high acceleration factors may enable single shot qMT mapping and are subject to future investigations. Alternatively, a 3D approach with short acquisition window and the proposed 5 MT weightings may be feasible in a short scan time [44], providing a significant increase in SNR that may enable the estimation of PSR and T_2^B, however respiratory motion during a free-breathing acquisition would need to be carefully addressed.

Other limitations of this study may be the use of fixed T_1^A and T_2^A rates measured with techniques that do not model the effects of two pools (e.g. MOLLI or T2-prep bSSFP). However, simulations showed that the maximum error introduced into the calculation of PSR

due to this effect is likely to be less than 3%. Similarly, simulations showed that B1 variations affect matched PSR values at a proportional rate of close to 2:1 (see Supporting Information, Figure S4). Moreover, Chow *et al.* [45] has reported B1 deviations of up to 20-30% across the chest (including the lungs) but only smooth variations of approximately 5-10% across left ventricle ROIs at 1.5T. Thus, B1 inhomogeneity could potentially generate inaccurate or biased PSR values, however, it is unlikely to explain or correlate with the observed regional variations of PSR (associated with scar) in post MI patients.

Regarding the patient study, the relatively large age difference between healthy subjects and patients constitutes another limitation, as well as the small size of the patient cohort. In terms of accuracy necessary to identify clinical fibrosis, a larger number of clinically well-defined patients with infarcts of defined chronicity may be needed to establish a "true" PSR value for infarcted myocardium. Furthermore, other factors that may affect the MT effects should be also taken into account when assessing diseased myocardium, such as large increases in pH which have been shown to affect the MT exchange rate [46] .

Conclusion

We have demonstrated that human myocardial qMT mapping is feasible and can be done with a 15 heartbeat qMT imaging protocol in a single breath-hold. Furthermore, PSR variations among healthy subjects (i.e., 0.65% PSR) were less than 50% the average PSR difference between core scar and remote myocardium in patients (i.e., 1.7% PSR). Thus, the results showed that the precision for measuring PSR in remote myocardium in-vivo with the proposed sequence may be sufficient for identifying focal fibrosis.

Supporting Information

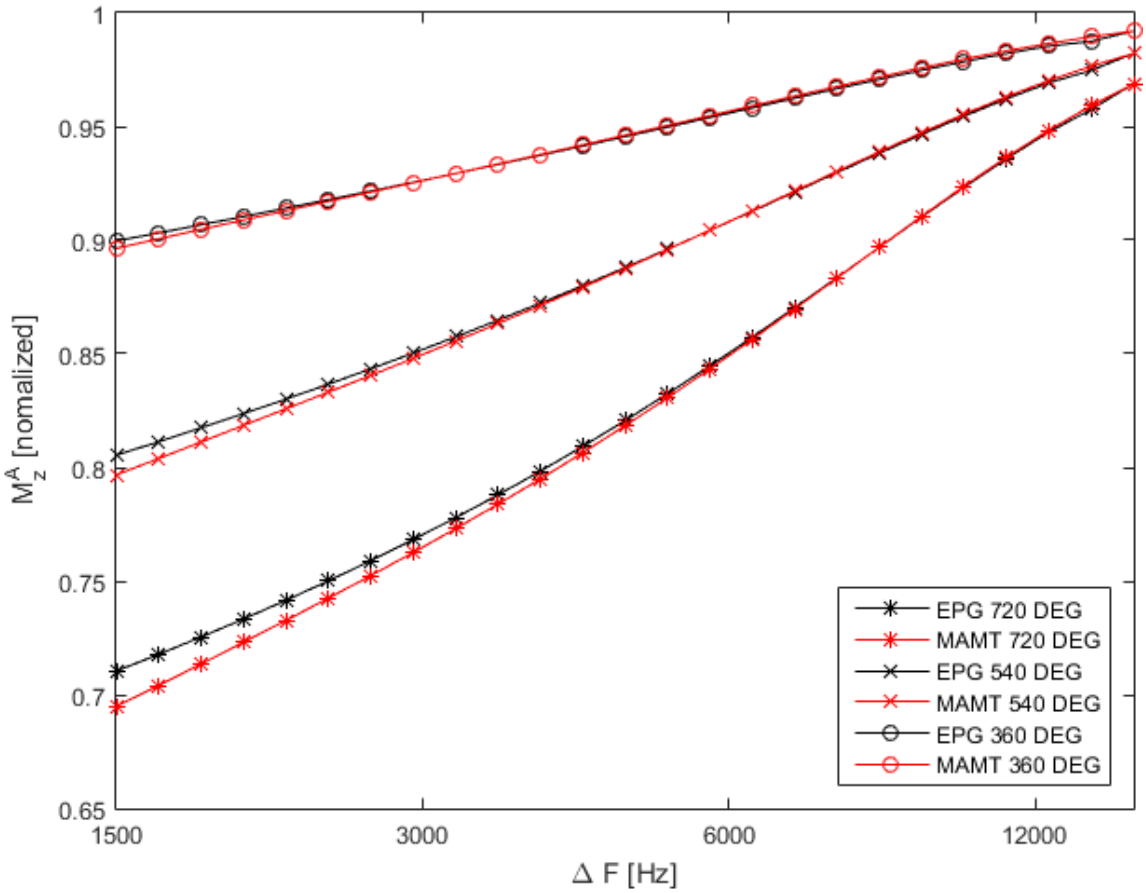

Figure S1. Comparison of comparison of EPGX-MT vs MAMT models for using flip angles 360˚, 540˚ and 720˚ as a function of frequency offset Δf. Small discrepancies between the methods increase at lower frequencies and higher flip angles.

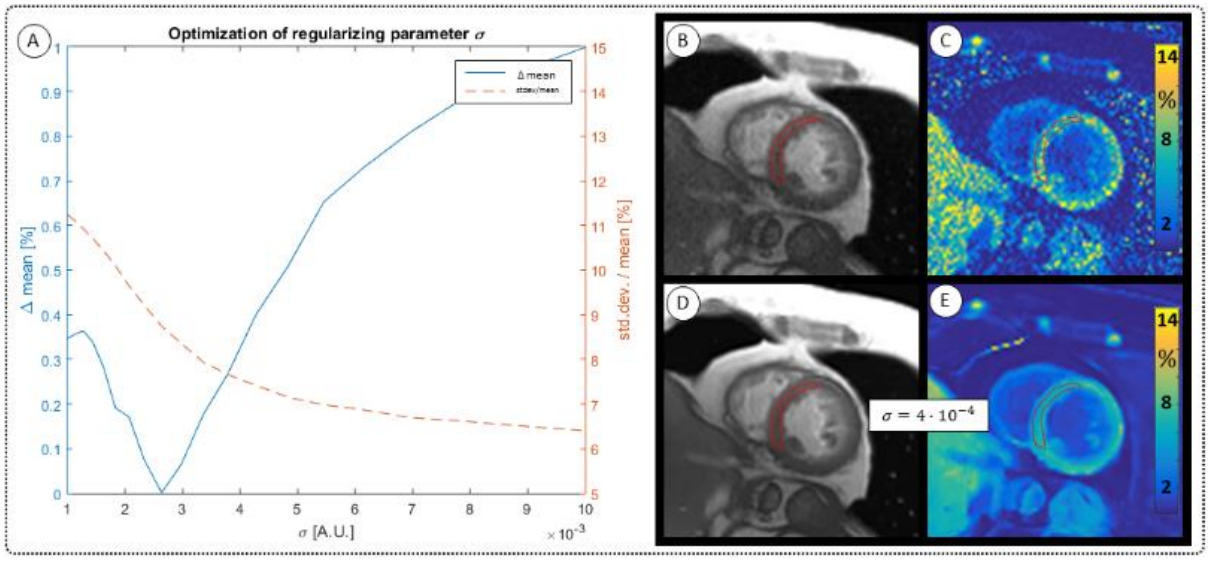

Figure S3 Optimization of image de-noising and impact on PSR estimation. (A) Left axis shows the difference between the mean values of original and denoised images ("Δ mean" line) for a myocardial ROI with varying regularization level σ, while the right axis shows the ratio between the mean value and standard deviation of the same ROI for each regularized image. (B-C) Example mid-ventricular slice showing an original (non-denoised) MT weighted image and the obtained PSR

parameter map, respectively. (D-E) Denoised MT weighted image and its respective PSR parameter map, at optimal regularization level σ=4e-4.

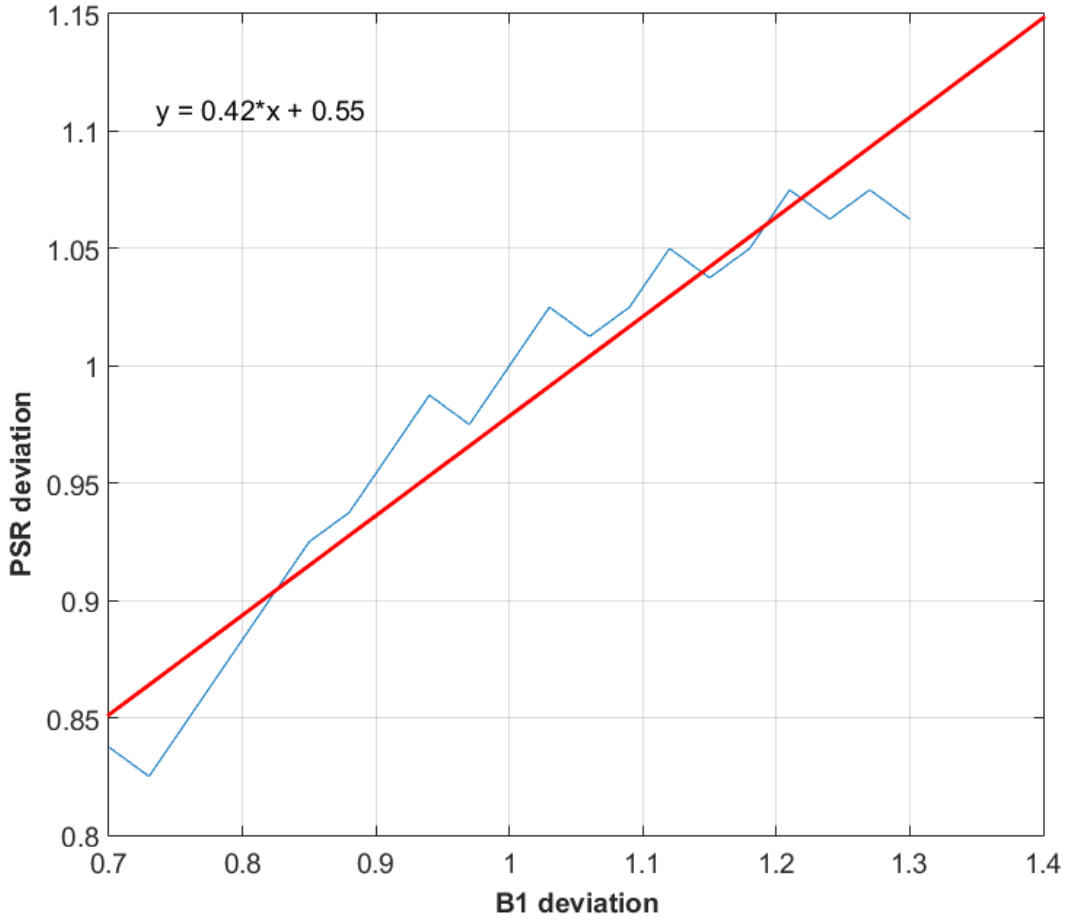

*Figure S4. Simulated PSR matches (blue line) showing 'PSR deviation' from the true value as a function of 'B1 deviation' or inhomogeneity for a 5-MTw protocol. The relationship between B1 and PSR deviation appears proportional approximately 2:1, as reflected by the best fit line (red) with equation "y = 0.42*x + 0.55".*

REFERENCES

1. Flett, A.S., et al., *Evaluation of techniques for the quantification of myocardial scar of differing etiology using cardiac magnetic resonance.* JACC Cardiovasc Imaging, 2011. **4**(2): p. 150-6.
2. Mewton, N., et al., *Assessment of myocardial fibrosis with cardiovascular magnetic resonance.* J Am Coll Cardiol, 2011. **57**(8): p. 891-903.
3. Kellman, P., et al., *Extracellular volume fraction mapping in the myocardium, part 1: evaluation of an automated method.* J Cardiovasc Magn Reson, 2012. **14**: p. 63.
4. Bull, S., et al., *Human non-contrast T1 values and correlation with histology in diffuse fibrosis.* Heart, 2013. **99**(13): p. 932-7.

5. van Oorschot, J.W., et al., *Endogenous contrast MRI of cardiac fibrosis: beyond late gadolinium enhancement.* J Magn Reson Imaging, 2015. **41**(5): p. 1181-9.
6. Kuo, P.H., et al., *Gadolinium-based MR contrast agents and nephrogenic systemic fibrosis.* Radiology, 2007. **242**(3): p. 647-9.
7. Robert, P., et al., *One-year Retention of Gadolinium in the Brain: Comparison of Gadodiamide and Gadoterate Meglumine in a Rodent Model.* Radiology, 2018. **288**(2): p. 424-433.
8. Phinikaridou, A., et al., *In vivo magnetization transfer and diffusion-weighted magnetic resonance imaging detects thrombus composition in a mouse model of deep vein thrombosis.* Circ Cardiovasc Imaging, 2013. **6**(3): p. 433-440.
9. Crooijmans, H.J., et al., *Cardiovascular magnetization transfer ratio imaging compared with histology: a postmortem study.* J Magn Reson Imaging, 2014. **40**(4): p. 915-9.
10. Wolff, S.D. and R.S. Balaban, *Magnetization transfer contrast (MTC) and tissue water proton relaxation in vivo.* Magn Reson Med, 1989. **10**(1): p. 135-44.
11. Stromp, T.A., et al., *Gadolinium free cardiovascular magnetic resonance with 2-point Cine balanced steady state free precession.* J Cardiovasc Magn Reson, 2015. **17**: p. 90.
12. Weber, O.M., et al., *Assessment of magnetization transfer effects in myocardial tissue using balanced steady-state free precession (bSSFP) cine MRI.* Magn Reson Med, 2009. **62**(3): p. 699-705.
13. Duan, C., et al., *Non-contrast myocardial infarct scar assessment using a hybrid native T1 and magnetization transfer imaging sequence at 1.5T.* Magn Reson Med, 2019. **81**(5): p. 3192-3201.
14. Vavasour, I.M., et al., *Is the magnetization transfer ratio a marker for myelin in multiple sclerosis?* J Magn Reson Imaging, 2011. **33**(3): p. 713-8.
15. Sled, J.G. and G.B. Pike, *Quantitative imaging of magnetization transfer exchange and relaxation properties in vivo using MRI.* Magn Reson Med, 2001. **46**(5): p. 923-31.
16. Henkelman, R.M., et al., *Quantitative interpretation of magnetization transfer.* Magn Reson Med, 1993. **29**(6): p. 759-66.
17. Malik, S.J., R. Teixeira, and J.V. Hajnal, *Extended phase graph formalism for systems with magnetization transfer and exchange.* Magn Reson Med, 2018. **80**(2): p. 767-779.
18. Weigel, M., *Extended phase graphs: dephasing, RF pulses, and echoes - pure and simple.* J Magn Reson Imaging, 2015. **41**(2): p. 266-95.
19. Graham, S.J. and R.M. Henkelman, *Understanding pulsed magnetization transfer.* J Magn Reson Imaging, 1997. **7**(5): p. 903-12.
20. Morrison, C., G. Stanisz, and R.M. Henkelman, *Modeling magnetization transfer for biological-like systems using a semi-solid pool with a super-Lorentzian lineshape and dipolar reservoir.* J Magn Reson B, 1995. **108**(2): p. 103-13.
21. Ramani, A., et al., *Precise estimate of fundamental in-vivo MT parameters in human brain in clinically feasible times.* Magn Reson Imaging, 2002. **20**(10): p. 721-31.
22. Griswold, M.A., et al., *Generalized autocalibrating partially parallel acquisitions (GRAPPA).* Magn Reson Med, 2002. **47**(6): p. 1202-10.
23. Bustin, A., et al., *Five-minute whole-heart coronary MRA with sub-millimeter isotropic resolution, 100% respiratory scan efficiency, and 3D-PROST reconstruction.* Magn Reson Med, 2019. **81**(1): p. 102-115.
24. Modat, M., et al., *Fast free-form deformation using graphics processing units.* Comput Methods Programs Biomed, 2010. **98**(3): p. 278-84.

25. Koenig, S.H., R.D. Brown, 3rd, and R. Ugolini, *Magnetization transfer in cross-linked bovine serum albumin solutions at 200 MHz: a model for tissue.* Magn Reson Med, 1993. **29**(3): p. 311-6.
26. Messroghli, D.R., et al., *Modified Look-Locker inversion recovery (MOLLI) for high-resolution T1 mapping of the heart.* Magn Reson Med, 2004. **52**(1): p. 141-6.
27. Akcakaya, M., et al., *Improved quantitative myocardial T2 mapping: Impact of the fitting model.* Magn Reson Med, 2015. **74**(1): p. 93-105.
28. Giri, S., et al., *T2 quantification for improved detection of myocardial edema.* J Cardiovasc Magn Reson, 2009. **11**: p. 56.
29. Huang, T.Y., et al., *T2 measurement of the human myocardium using a T2-prepared transient-state TrueFISP sequence.* Magn Reson Med, 2007. **57**(5): p. 960-6.
30. Dabir, D., et al., *Reference values for healthy human myocardium using a T1 mapping methodology: results from the International T1 Multicenter cardiovascular magnetic resonance study.* J Cardiovasc Magn Reson, 2014. **16**: p. 69.
31. Cerqueira, M.D., et al., *Standardized myocardial segmentation and nomenclature for tomographic imaging of the heart. A statement for healthcare professionals from the Cardiac Imaging Committee of the Council on Clinical Cardiology of the American Heart Association.* Circulation, 2002. **105**(4): p. 539-42.
32. Dortch, R.D., et al., *Quantitative magnetization transfer imaging in human brain at 3 T via selective inversion recovery.* Magn Reson Med, 2011. **66**(5): p. 1346-52.
33. Gochberg, D.F. and J.C. Gore, *Quantitative magnetization transfer imaging via selective inversion recovery with short repetition times.* Magn Reson Med, 2007. **57**(2): p. 437-41.
34. Li, K., et al., *A rapid approach for quantitative magnetization transfer imaging in thigh muscles using the pulsed saturation method.* Magn Reson Imaging, 2015. **33**(6): p. 709-17.
35. Sinclair, C.D., et al., *Quantitative magnetization transfer in in vivo healthy human skeletal muscle at 3 T.* Magn Reson Med, 2010. **64**(6): p. 1739-48.
36. Scholz, T.D., et al., *Water-macromolecular proton magnetization transfer in infarcted myocardium: a method to enhance magnetic resonance image contrast.* Magn Reson Med, 1995. **33**(2): p. 178-84.
37. Stromp, T.A., et al., *Quantitative Gadolinium-Free Cardiac Fibrosis Imaging in End Stage Renal Disease Patients Reveals A Longitudinal Correlation with Structural and Functional Decline.* Sci Rep, 2018. **8**(1): p. 16972.
38. Ward, K., A.E. Schussheim, and R.S. Balaban, *Contribution of mitochondria to cardiac muscle water/macromolecule proton magnetization transfer.* Magn Reson Med, 2003. **50**(6): p. 1312-6.
39. Witschey, W.R., et al., *In vivo chronic myocardial infarction characterization by spin locked cardiovascular magnetic resonance.* J Cardiovasc Magn Reson, 2012. **14**: p. 37.
40. van Oorschot, J.W., et al., *Endogenous assessment of diffuse myocardial fibrosis in patients with T1rho -mapping.* J Magn Reson Imaging, 2017. **45**(1): p. 132-138.
41. Duvvuri, U., et al., *T1rho-relaxation in articular cartilage: effects of enzymatic degradation.* Magn Reson Med, 1997. **38**(6): p. 863-7.
42. Li, X., et al., *In vivo T(1rho) and T(2) mapping of articular cartilage in osteoarthritis of the knee using 3 T MRI.* Osteoarthritis Cartilage, 2007. **15**(7): p. 789-97.
43. Witschey, W.R., et al., *T1rho MRI quantification of arthroscopically confirmed cartilage degeneration.* Magn Reson Med, 2010. **63**(5): p. 1376-82.

44. Bustin, A., et al., *High-dimensionality undersampled patch-based reconstruction (HD-PROST) for accelerated multi-contrast MRI.* Magn Reson Med, 2019. **81**(6): p. 3705-3719.
45. Chow, K., I. Paterson, and R. Thompson, *1136 Cardiovascular radiofrequency (B1) field maps using HASTE.* Journal of Cardiovascular Magnetic Resonance, 2008. **10**(1): p. A261.
46. Kennan, R.P., et al., *The effects of cross-link density and chemical exchange on magnetization transfer in polyacrylamide gels.* J Magn Reson B, 1996. **110**(3): p. 267-77.

Chapter 7 : Three-Dimensional Motion-Compensated Quantitative Magnetization Transfer MRI for Myocardial Tissue Characterization

Three-Dimensional Motion-Compensated Quantitative Magnetization Transfer MRI for Myocardial Tissue Characterization

Karina López[1], Radhouene Neji[1,2], Aurelien Bustin[1], Shaihan J Malik[1], Reza Razavi[1], Claudia Prieto[1], Sébastien Roujol[1], René M Botnar[1]

[1]*School of Biomedical Engineering and Imaging Sciences, King's College London, UK*

[2]*MR Research Collaborations, Siemens Healthcare Limited, Frimley, UK*

Work not previously submitted to external peer-review.

Abstract

A 3D free-breathing motion-corrected sequence for myocardial tissue characterization using quantitative magnetization transfer imaging is presented. An imaging sequence for in-vivo cardiac imaging acquires 8 MT-prepared datasets in approximately 9 minutes during the diastolic resting phase and is preceded by image navigators for retrospective beat-to-beat translational motion correction. The 8 undersampled datasets are jointly reconstructed using a high-dimensionality patch based low-rank reconstruction method that exploits the redundancy within and along the contrast dimension. The reconstructed images are compared with standard (non-denoised and denoised) iterative SENSE reconstruction for validation. A spin-bath model of exchange with Extended Phase Graph simulation is used to model the transient MT weighted signal of the measured datasets to generate pool size ratio (PSR) and bound T2 (T2B) parameter maps based on dictionary matching. The sequence was evaluated in ex-vivo porcine myocardial tissue and in a healthy human subject. The ex-vivo measurements showed mean PSR value of 5.6±1.4%, mean T2B of 21.9±4.7μs and mean R of 36±11Hz, in accordance with previous studies in the literature. PSR and T2B mapping in the human subject showed promising results

with respect to spatial variability of mean parameter values (PSR lateral wall 7.3±1.6% *vs* septal wall 8.2±1.1%, T2B: lateral wall 14.1±1.7μs *vs* septal wall 10.8±1.1μs) and clinical feasibility. Exchange rate mapping failed to converge in-vivo, while PSR and T2B maps appeared sensitive to noise and unwanted free-pool saturation. Hence, further studies are necessary to address the issues observed in this work and to realise the full potential of free-breathing 3D quantitative MT imaging for non-contrast myocardial tissue characterization.

Author's contributions

Lopez: study design, implementation of MT sequence in Siemens pulse programming environment, acquisition of all data related to phantom and human experiments, implementation of part of the image reconstruction and signal model code, image reconstruction and dictionary matching, analysis and interpretation of all data and drafting of manuscript.

Neji: study design, acquisition of data.

Bustin: implementation of part of the image reconstruction code.

Malik: implementation of part of the signal model code and critical revision.

Razavi: study design.

Prieto: conception and design of data acquisition.

Roujol: study design.

Botnar: conception and overall study design, data acquisition, interpretation of data and critical revision.

Introduction

Characterization of myocardial fibrosis has prognostic value in a number of cardiomyopathies including myocarditis, myocardial infarction, arrhythmia and ultimately heart failure [1, 2]. Late gadolinium enhancement (LGE) MRI is the gold standard for the localization and characterization of the extent of focal myocardial fibrosis but cannot reliably detect diffuse fibrosis [3] and requires the injection of a contrast injection. Typical LGE acquisition protocols require multiple breathholds (12-15) to cover the entire left ventricle in short and long axis views and thus can be long (5-10 minutes) and exhausting especially for sick patients. Signal enhancement is dependent upon focal changes of the contrast concentration and thus is well suited for detection of myocardial infarction due to the increased extracellular space related to cell death but is generally unable to visualise diffuse or reactive fibrosis. While LGE MRI remains the gold-standard for myocardial tissue characterization there is growing concern about gadolinium deposition in the brain and nephrogenic systemic fibrosis (NSF) in patients with compromised kidney function. Hence, there is a need for a non-contrast quantitative MRI technique that can successfully identify and characterize both focal and diffuse myocardial fibrosis.

Qualitative non-contrast cardiac MRI techniques typically focus on characterization of macroscopic or structural changes which are, naturally, associated with changes in the bulk magnetic properties of the tissue in question. Although qualitative MRI techniques appear sensitive to some pathological changes, such as T2 weighted imaging for oedema [4] or magnetization transfer ratio for myocardial infarction detection [5], they often lack the necessary specificity to biological markers of pathology. Quantitative MRI techniques may help modelling some of the physiological processes associated with cardiac pathology and increase the specificity of non-contrast cardiac MRI. Moreover, quantitative cardiac MRI

enables detection of diffuse pathologies, which is challenging on qualitative weighted images and are better suited for serial imaging and standardization of normal values.

Magnetization transfer is a technique that exploits the contribution of protons bound to large macromolecules on the MRI signal loss from off-resonance saturation. A preparation module comprising off-resonance pulses can selectively saturate the bound pool, which is characterized by a broad resonance spectrum and an extremely short T2 relaxation time. Protein-rich tissue such as myocardial muscle has a large bound pool which primarily includes the extracellular matrix, as well as cell membrane and mitochondria proteins [6]. Magnetization transfer models are (magnetization) exchange models between spin pools with markedly different T2 relaxation rates, e.g., the bound pool and the free (water) pool. However, other pools may be included to account for complex processes/tissue where multiple components of T2 relaxation times exist [7, 8]. The free parameters of a two-pool magnetization transfer model can range from 6 to 8, including T1 and T2 relaxation times of each pool, size of each pool and reciprocal exchange rates. This is a challenge for pixel-wise model fitting techniques both in terms of signal-to-noise ratio (SNR) and computing processing requirements.

Quantitative magnetization transfer has been used to characterize pathological changes in cerebral white matter associated with changes in the semisolid pool, such as myelin loss [8]. Dortch *et al.* has shown that quantitative magnetization transfer can assess changes in protein loss in thigh muscle associated with atrophy [9]. In Chapter 6 (also published here [10]), we showed promising results for the characterization of chronic myocardial scar using a spin bath quantitative magnetization transfer model based on extended phase graph simulation and dictionary matching, however, SNR remains a challenge .

In this study we propose a novel 3D multi-contrast sequence for quantitative in-vivo cardiac MT imaging using the spin bath EPG-X model of exchange [11] and an HD-PROST reconstruction [12] to achieve increased SNR in a clinically feasible acquisition time.

Methods

MRI sequence

A prototype sequence implemented on a 1.5T scanner (Magnetom Aera, Siemens Healthcare, Erlangen, Germany) is proposed for contrast-free quantitative 3D whole-heart in-vivo magnetization transfer imaging. The sequence comprises several sequentially acquired MT-weighted (MTw) segmented spoiled gradient echo (SPGR) images acquired over a few hundred heartbeats with varying MT preparation parameters, as shown in **Figure 7-1**. Each MTw image is acquired in free-breathing with beat-to-beat translational motion correction via estimated image navigators (iNAVs) that preced the SPGR imaging sequence. To allow for magnetization recovery, the MT prepared image acquisition is followed by a 5-seconds pause period. The short GRE imaging readout module (<100 ms) is played out during the mid-diastolic resting period to minimise cardiac motion artifacts. To speed up data acquisition and ensure incoherent undersampling artefacts a variable density Cartesian trajectory with spiral like profile order (VD-CASPR) is employed, which enables higher sampling density towards the centre of k-space (see **Figure 7-1C**). Imaging parameters included: isotropic resolution 1.7 mm^3, field of view: 350x300 mm^2 (coronal orientation), slices: 25 and 52 (phantom and human subject), SPGR flip angle 15˚, TE/TR=3.2/6.9ms, receiver Bandwidth=250 Hz.

Two consecutive modules or building blocks of the MRI sequence are played out every heartbeat (see **Figure 7-1A**), namely, (1) the MT preparation module followed and (2) the imaging readout module.

The MT preparation module consists of a train of 20 identical Sinc-shaped RF pulses of 20.48ms length (bandwidth 268 Hz) and configurable frequency offset and flip angle. In-between the MT pulses there is a "pause" period of 1.5ms during which spoiler gradients dephase any residual tranverse magentisation. The pause period is required due to SAR limitations. **Figure 7-1B** shows a pulse diagram of the MT preparation module.

The imaging module comprises two parts; (I) the image navigator (iNAV) consisting of 14 start-up pulses preceding (II) the SPGR imaging sequence. The flip angle of the image navigator pulses increases linearly from ~0 to 15 degrees, the value employed for the imaging sequence. Each 2D image navigator (performed every heart beat) is obtained in coronal orientation with a standard Cartesian acquisition which has low spatial resolution in the left-to-right direction but high resolution corresponding to the imaging sequence in the foot-head direction. A coronal orientation (FH + LR motion correction) was selected over, e.g., sagittal orientation (FH + anterior–posterior), because it may give a better interface between the lung and left ventricle leding to improved motion estimation [13].

Phantom experiments were carried out using three different protocols N25, N8 and N5 with n=25, 8 and 5 MT-weighted images, respectively, and with no acceleration/under-sampling. In-vivo cardiac imaging in humans was carried out using N8 only with under-sampling factors 3 and 5 to maintain a short and clinically feasible acquisition time.

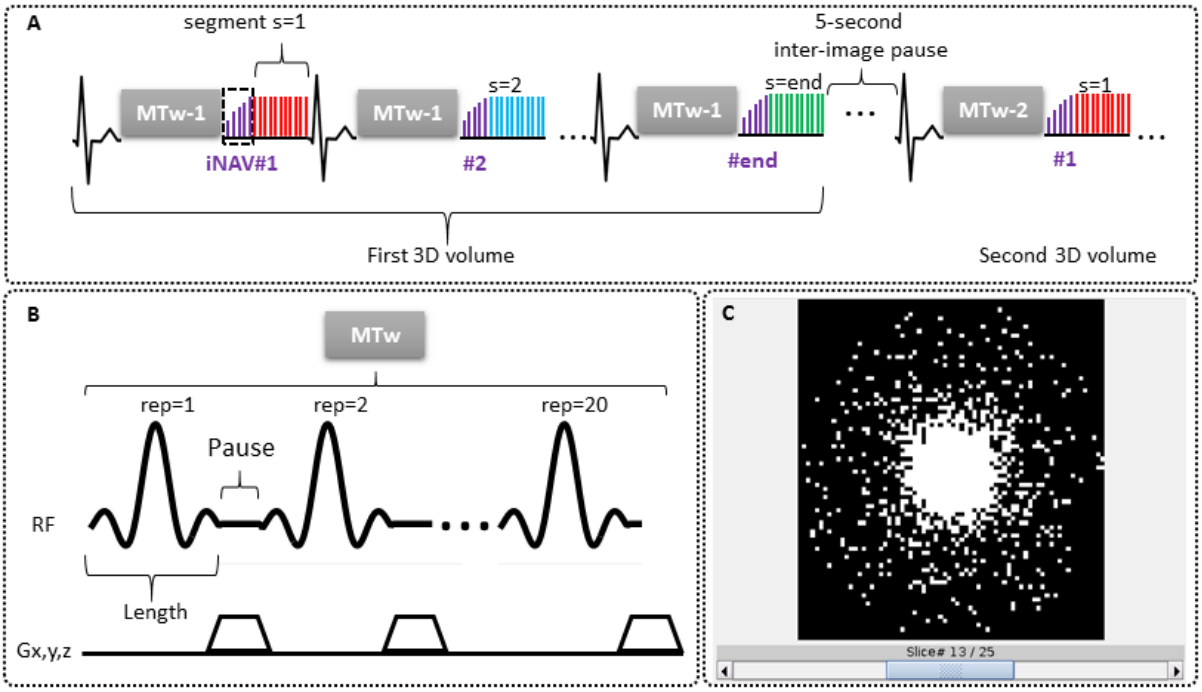

***Figure 7-1**. MRI sequence diagram. (A) Acquisition scheme of the first two MT-weighted volumes. In each heartbeat, an MT preparation module is performed, followed by an image navigator (iNAV), which precedes a spoiled gradient echo (SPGR) imaging readout made to coincide with the diastolic quiescent period. After all segments of the first 3D volume are acquired, a 5-seconds waiting period is performed to allow Mz magnetization recovery before acquisition of the second 3D volume and thereon the scheme is repeated for the remaining MT contrasts. (B) Pulse sequence diagram of an MT preparation module comprising 20 identical MT pulses separated by "pause" periods, during which spoiler gradients are perfomed in all three spatial directions to dephase any remaining transverse magnetization. The flip angle and frequency of the MT pulses varies between the sequentially acquired 3D volumes. (C) Example of the k-space trajectory (k_y - k_z plane) for one volume after all segments have been obtained (i.e., white spots) using the variable density CASPR (VD-CASPR) method with an acceleration factor 5.*

Image reconstruction

The MTw images were reconstructed off-line (MATLAB v. R2017b) employing three different approaches for comparison. Method I (SENSE), which was used as a "ground truth" or reference, consisted of an iterative SENSE reconstruction of each 3D MT-weighted volume (individually). Method II (DENOISED) was an iterative SENSE reconstruction of each volume (individually) followed by 3D patch-based denoising (i.e., optimization problem #2 in Bustin

et al. [12]) applied on all (image-space) reconstructed volumes (i.e., along the contrast dimension). Finally, method III (HD-PROST) was a joint iterative SENSE and 3D patch-based reconstruction performed simultaneously on all 3D (k-space) volumes [12].

Translational motion correction was performed prior to reconstruction (with each method) using the iNAVs as described above.

The SENSE reconstruction (of methods I and II) was performed iteratively using Walsh's 3D method [14] for estimating coil sensitivity maps and the conjugate gradient algorithm. A maximum of 3 iterations and 30 coils were used.

The denoising method (i.e., method II) exploits the redundancy of local and non-local features within the images and along the contrast dimension in order to build a high-order, low-rank tensor made of similar image patches. The patches are then de-noised using singular value decomposition (SVD) and truncation. A full denoised image can then be recreated from the image patches. The denoising parameters included image patch size, number of iterations and sigma value (i.e., the SVD threshold) and were optimized empirically to obtain the best compromise between increased precision *vs* loss in accuracy by comparing the results (across a range of parameters) against a non-denoised (i.e., method I) dataset, as shown in **Figure 7-2**. Square image patches of size 6 px and σ=0.4 were used in both the phantom and the in-vivo datasets. The number of iterations was 3 based on previous experiments [12, 15] and to minimize the computation time.

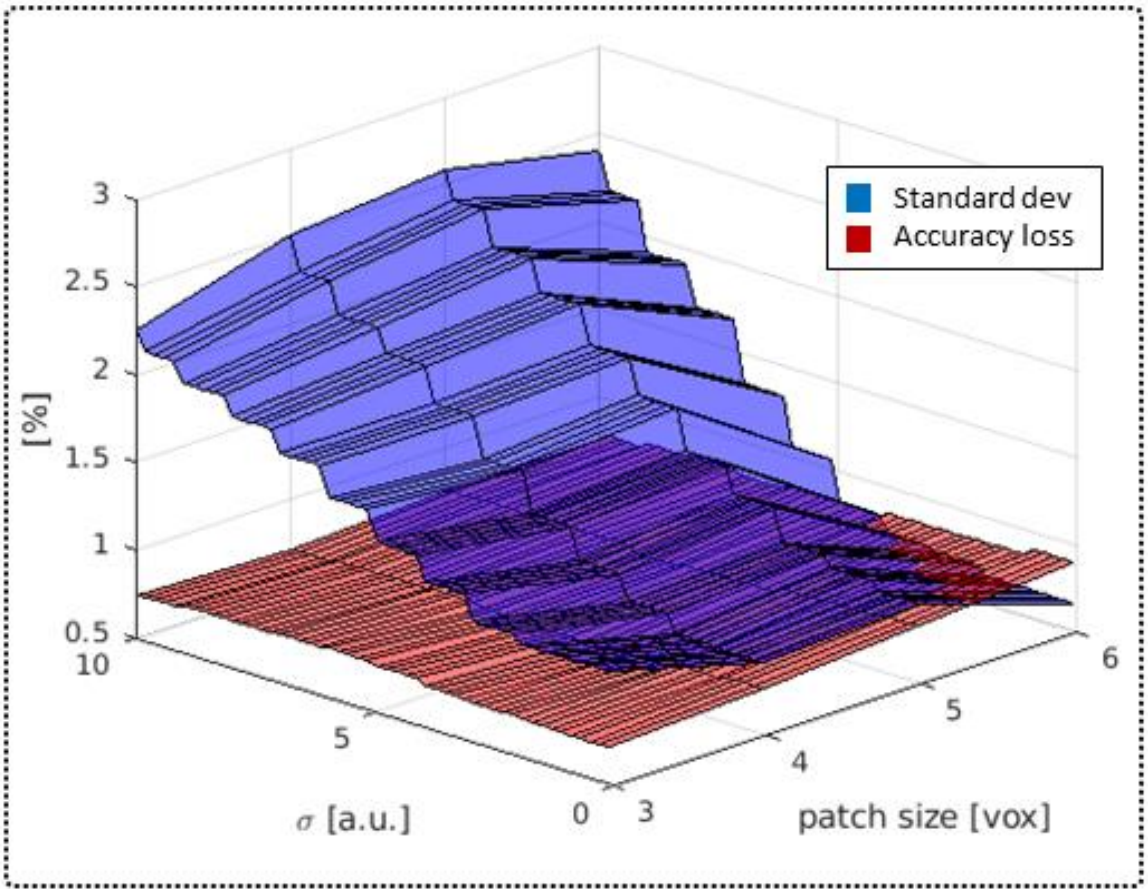

Figure 7-2*. Empirical optimization of denoising parameters image patch size and σ using mean and standard deviation values for a region of interest (ROI) in myocardial tissue of a phantom MT dataset. In the plot, the percentage standard deviation with respect to the mean value of a denoised dataset and difference between the mean values of the denoised and non-denoised datasets are seen as a function of image patch size and σ. As the σ increases the standard deviation significantly decreases while the loss in accuracy only slightly increases (implicitly showing the robustness of the method). Although a small patch size seems beneficial to accuracy it also increase the computation time (not shown in Figure).*

The HD-PROST method (i.e., method III) is a generalization of the PROST method [15] and integrates the denoising of method II into the image reconstruction. HD-PROST formulates the MR reconstruction as a two-part constrained optimization problem. On each iteration, the first part of the problem consists of a multi-channel multi-contrast MR reconstruction solved with a regularized iterative SENSE formulation and including a 3D patch-based denoising "update"

(i.e. method II) in the sparsity promoting term. In the *second part* of the problem, the dominant components of the (high-order low-rank) tensor are optimised through the groups of image patches to generate a de-noised tensor that is fed back to the the *first part* as the "update".

In method III, the iterative SENSE regularization parameter was set to λ=0.1, the image patch size to 6px and the SVD threshold to σ=0.4.

After reconstruction (with all methods), each MTw image was pixel-wise divided by the mean signal value of all MTw images to generate a normalized input for the next stage of image processing.

Quantitative magnetization transfer mapping

Signal Model

A binary spin bath model of exchange is considered for the magnetization of free-water protons, M_0^A, and the magnetization of macromolecule-bound protons, M_0^B, using an Extended Phase Graphs (EPG) approach that finds a transient solution [11] suitable for an in-vivo MT preparation scheme.

The EPG framework analyses the system's magnetization response in terms of its configuration states [16], which can be described as Fourier Transforms (FT) of the spatial magnetization components. In this space, the net magnetization dephasing caused by spatially-variant gradients over an entire ensemble of spins within a volume V is uniquely described by the "*spatial frequency*" number, *k*, making computation much more efficient. The interactions with RF pulses, gradients, and the effects of relaxation and exchange are all represented by simple matrix operators.

The framework used in this study is based on the EPG-X method proposed by Malik *et al.* [11]. The EPG-X method extends the classic EPG framework to include a fourth configuration state, i.e., $[\tilde{F}_+, \tilde{F}_-, \tilde{Z}_A, \tilde{Z}_B]^T$, where $\tilde{Z}_B$ is as a FT of the bound pool's longitudinal magnetization,

M_Z^B. The evolution of $\tilde{Z}_B$ is coupled to $\tilde{Z}_A$ via first order forward and backward exchange rates: k_f (or kf) and k_b . Because the time scale of the decay of the transverse magnetization in the bound pool is very short (<20μs), it is assumed to decay instantaneously. For this reason, only the exchange between the longitudinal magnetization is considered in this model. Another consequence of this instantaneous decay is that the RF excitation for the bound pool can be completely described as an instant saturation of the longitudinal magnetization at a certain rate W, proportional to RF power deposition, ω_1^2, and the bound pool's line absorption profile, g_B,

$$W(2\pi\Delta) = \pi\,{\omega_1}^2 g_B(2\pi\Delta, T_2^B) \tag{7-1}$$

where Δ is the offset frequency of the irradiation. In the case of a shaped RF pulse, equation (6-1) can be generalized [17], integrating over time for the duration of the pulse so that a time average of the saturation rate is obtained: $\bar{W}$. The absorption profile g_B depends on Δ with a super-Lorentzian form, typical of partially ordered materials and semi-solids where the dipolar Hamiltonian does not average to zero over time. The width of the super-Lorentzian form is characterized by the T2 of the bound pool, T_2^B, and can be obtained as [18]:

$$g_B(2\pi\Delta, T_2^B) = \sqrt{2/\pi}\; T_2^B \int_0^{\pi/2} \frac{e^{-2\frac{(2\pi\Delta\, T_2^B)^2}{(3cos^2\theta-1)^2}}}{|3cos^2\theta - 1|}\, sin\theta d\theta \tag{7-2}$$

To further simplify the calculation of $\bar{W}$, the time-variant amplitude of the RF pulse $\omega_1 \rightarrow \omega_1(t)$ in equation *(7-1)* is approximated by a time-constant value using Ramani's continuous wave power-equivalent formula [19].

In our ECG-triggered cardiac implementation, each MT preparation pulse is simulated by the RF transition operator $\boldsymbol{T}$ acting onto the longitudinal states $Z_n = [\tilde{Z}_A, \tilde{Z}_B]$ as,

$$\boldsymbol{T} = \begin{bmatrix} 1 & 0 \\ 0 & e^{-\bar{W}\,\tau_{RF}} \end{bmatrix} \tag{7-3}$$

The effect on the bound pool is modelled by the average of the RF saturation rate $\bar{W}$ times the length of the RF pulse τ_{RF}, while the longitudinal magnetization of the free water pool is not disturbed. After application of the transition operator, the evolution along the entire length of the pulse (plus any waiting/pause time between pulses) is governed by exchange and relaxation [11]:

$$\dot{F_n} = \begin{bmatrix} -\frac{1}{T_2^A} & 0 \\ 0 & -\frac{1}{T_2^A} \end{bmatrix} F_n \tag{7-4}$$

$$\dot{Z_n} = \begin{bmatrix} -\frac{1}{T_1^A} - k_f & k_B \\ k_f & -\frac{1}{T_2^B} - k_B \end{bmatrix} Z_n$$

Where $F_n = [\tilde{F}_+, \tilde{F}_-]$ represents the free pool's transverse configuration states. A spoiled gradient echo (SPGR) acquisition immediately follows a train of MT preparation RF pulses, as described in [11]. Exchange and relaxation operators are applied again during waiting time between heartbeats.

A simulation of the sequence was also implemented using the MAMT method [20], which as described on page 50, and which provides a numerical solution for the exchange equations without discarding free pool saturation. The performance of the EPG-X was evaluated against the MAMT method (considered "ground truth") to optimize the selection of the MT preparation parameters including flip angle and frequency offset, as shown in **Figure 7-3**.

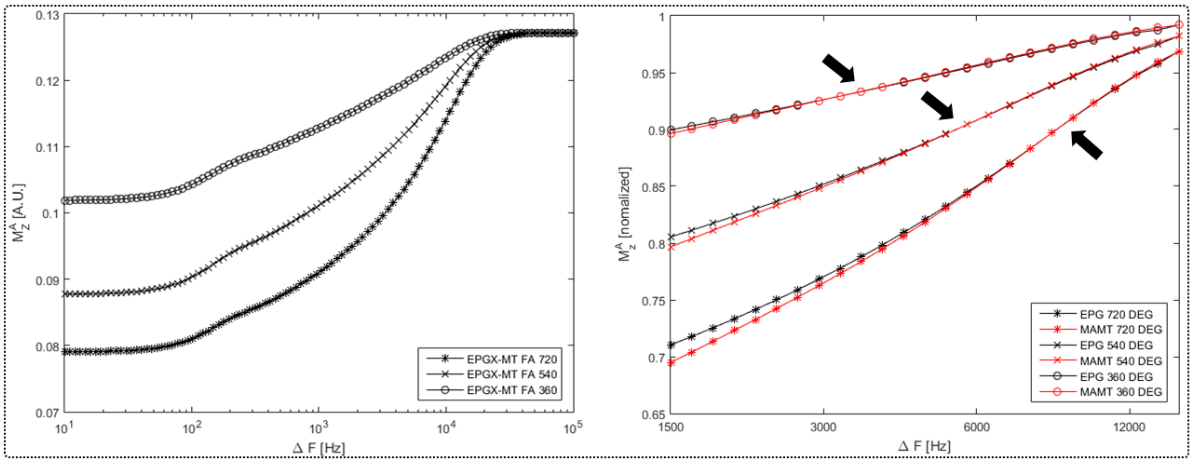

Figure 7-3. *Left, simulation of free pool longitudinal magnetization saturation as a function of frequency offset (10 to 100,000 Hz) using EPGX-MT with three different MT flip angles (360, 540 and 720). Right, comparison of EPGX-MT vs MAMT with the same filp angles (offset=1500-15000Hz). Discrepancies between the methods increase at lower frequencies and higher flip angles. Black arrows indicate regions with better agreement between the methods.*

Dictionary matching

A dictionary of possible signal evolutions was created using the model described before. Each entry in the dictionary is a vector of as many elements as MTw images. After computation, magnitude entries are normalized by the mean of all its elements.

The vector difference between measured data and every dictionary entry was computed, for every pixel, to match the entry with highest determination coefficient R^2,

$$R^2 = 1 - \frac{\sum_{i=1}^{n}(m_i - f_i)^2}{\sum_{i=1}^{n}(m_i - \bar{m})^2} \qquad (7\text{-}5)$$

where m_i is measured data point for the i-th MT weighting (for a given pixel), f_i is the corresponding i-th fitted value, $\bar{m}$ is the mean of all MT weighted data points (for a given pixel) and n is number of MTw acquisitions.

Phantom experiments

A butcher's pig heart, i.e., ex-vivo porcine myocardial tissue, was placed in saline solution and was used to evaluate the performance of the reconstruction approaches and the signal model.

The reconstruction approaches (see above) were compared by making ROI measurements on each reconstructed dataset using an acquisition protocol with n=25 MTw images. Two other acquisition protocols with 8 and 5 MTw images (N8 and N5, respectively) were evaluated against N25 to assess the robustness of the model and to explore the potential for clinical translation.

MT preparation parameters for the three protocols N25, N8 and N5 are shown in **Table 7-1**. N25 was considered the reference or "ground truth", comprising the broadest spectrum of frequency offsets from 1.5 to 8.5 kHz and with a single flip angle of 540˚ (due to scanner time constraints associated with acquiring 25 consecutive 3D high-resolution images). N8 and N5 comprise 8 and 5 contrasts characterized by flip angle/frequency offset pairings selected based on the results of the comparison of EPG-X vs MAMT simulations (see **Figure 7-3** above) to provide the broadest range of frequencies (for better bound pool T2 estimation) with the least amount of free pool saturation.

Table 7-1. *MT preparation parameters for protocols N25, N8 and N5. The frequency offset values of N25 comprise 25 values logarithmically spaced between 1.5 and 8.5 kHz (including 1.5 and 8.5 kHz).*

	Flip angle [˚]	***Frequency offset [kHz]***
N25	540	1.5 – 8.5 (log spaced)
N8	720, 720, 540, 720, 360, 540, 360, 540	3.9, 5.7, 4.3, 8.5, 2.0, 3.5, 2.9, 5.0
N5	720, 720, 540, 720, 360	3.9, 5.7, 4.3, 8.5, 2.0

Independent (free pool) T1 maps were obtained using MOLLI [21] (scheme 5(3)3, resolution= 1.7x1.7x2 mm^3, BW=770Hz, GRAPPA acceleration factor=2, FA=35˚, TE/TR=1.76/2.7ms). Independent (free pool) T2 maps were obtained with a T2-prepared bSSFP (TET2prep = 0, 25 and 50 ms, resolution=1.7x1.7x2 mm^3, BW=778 Hz, GRAPPA acceleration factor=2, FA=70˚,

TE/TR=1.59/2.7ms) using a 2-parameter fitting model [22]. Independent T1 and T2 mean ROI measurements were used as input parameters for the model referred to as T_1^A and T_2^A, respectively.

The matching dictionary comprised three free parameters, namely, pool size ratio *PSR* [%] (1:0.2:15, brackets indicate the parameter vector characterized by a starting value, step size and final value, respectively), exchange rate *R* [Hz] (10:0.5:60) and bound pool transverse relaxation time T_2^B [us] (1:2:35).

Human subjects

Two healthy human subjects were scanned in-vivo as proof-of-concept using protocol N8 (see above) with an acceleration/under-sampling factor of 5 and reconstruction methods I and III (for comparison). The data was motion corrected prior to reconstruction using the translation motion correction procedure based on iNAVs as described before (page 70).

The acquisition time was approximately 9 minutes. The study was approved by our local research ethics committee and written informed consent was obtained from all subjects.

Results

Phantom experiments

The three reconstruction methods yielded consistent results in terms of saturation of the free pool (represented by images' normalized signal), which showed a decreasing trend towards high offset frequencies (from 1 to 10 kHz), as shown in **Figure 7-4**.

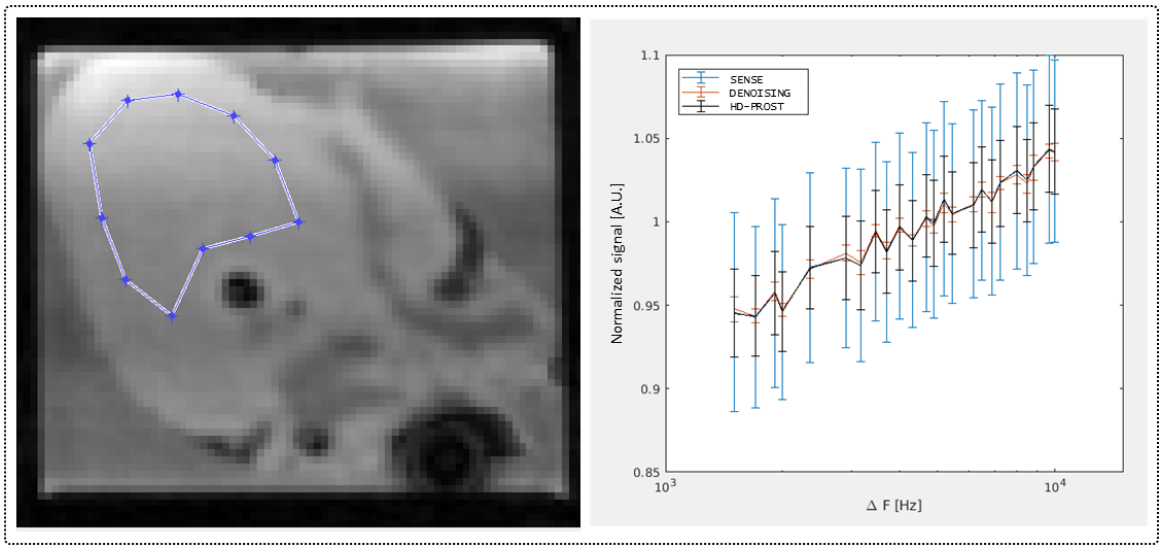

***Figure 7-4**. Left, myocardial region of interest (ROI) drawn in a slice of an MTw dataset from butcher's pig heart reconstructed using HD-PROST. Right, comparison of normalized MTw signal over the myocardial ROI (see Left) using three reconstruction methods. Error bars indicate standard deviation over the ROI.*

Dictionary matching of the measured data was successful, yielding determination coefficients R^2>0.937 in all matches. Two example matches are shown in **Figure 7-5** using HD-PROST and acquisition protocols N25 and N8.

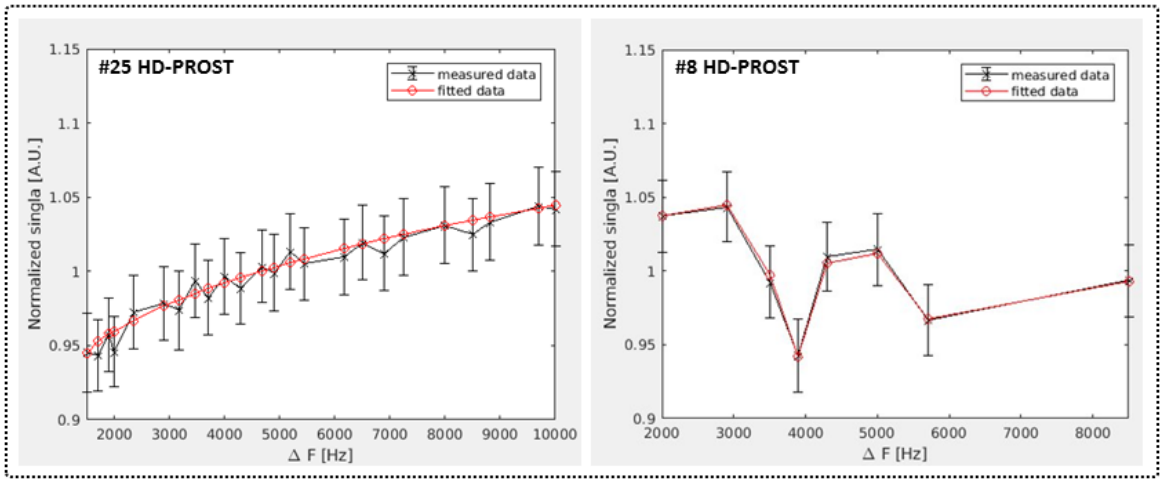

***Figure 7-5**. Measured data vs fitted data "matching" for protocols N25 (left) with determination coefficient R^2=0.96 and N8 (right) with R^2=0.99, both using HD-PROST.*

ROI measurements of MT parameters PSR, R and T2B for each protocol and reconstruction method are shown in **Table 7-2**. In all protocols, reconstruction method I showed the highest amount of standard deviation of PSR in a myocardial ROI, while reconstruction method II showed the least amount of standard deviation. Using protocol N25, methods I and III did not show statistically significant differences in terms of PSR or T2B mean values, while method II showed slightly decreased PSR values ($p=0.02$) and increased T2B ($P<0.01$) with respect to method I. PSR values showed an increase with protocols N8 and N5 with respect to protocol N25 in both methods I and III, while T2B values were found to decrease for the same reconstruction methods. Method II did not show significant changes in PSR values for the different protocols, however, T2B values were found to increase in N8 and N5 with respect to N25. Exchange rate R values did not show significant changes with respect to the acquisition protocol, however, mean values using method II were slightly lower than both methods I and III.

***Table 7-2**. MT parameter mean values for a pig myocardial region of interest using acquisition protocols N25, N8 and N5 (number of MTw images equals 25, 8, and 5, respectively) and reconstruction methods I, II and III.*

	PSR [%]	*T2B [us]*	*R [Hz]*
Method 1: SENSE			
N25	5.7 ± 1.7 *†	21.6 ± 4.9	42 ± 8
N8	8.2 ± 2.1	16.9 ± 6.9	45 ± 25
N5	8.4 ± 2.2	15.4 ± 7.3	44 ± 21
Method 2: DENOISING			
N25	5.2 ± 1.1*	29.6 ± 2.9	30 ± 12
N8	4.9 ± 1.0	35.9 ± 2.7	28 ± 15
N5	4.8 ± 0.7	37.8 ± 3.7	35 ± 13
Method 3: HD-PROST			
N25	5.7 ± 1.4†	21.9 ± 4.7	36 ± 11
N8	8.0 ± 1.8	17.9 ± 7.0	31 ± 19
N5	8.4 ± 1.3	15.5 ± 7.0	40 ± 18

*p=0.02, †n.s.s.

T2B and PSR maps with corresponding MTw slice obtained with HD-PROST are shown in **Figure 7-6**. Both maps appear homogenous in the myocardial region despite an apparent artefact across the phantom (below the ROI drawn in black dashed line).

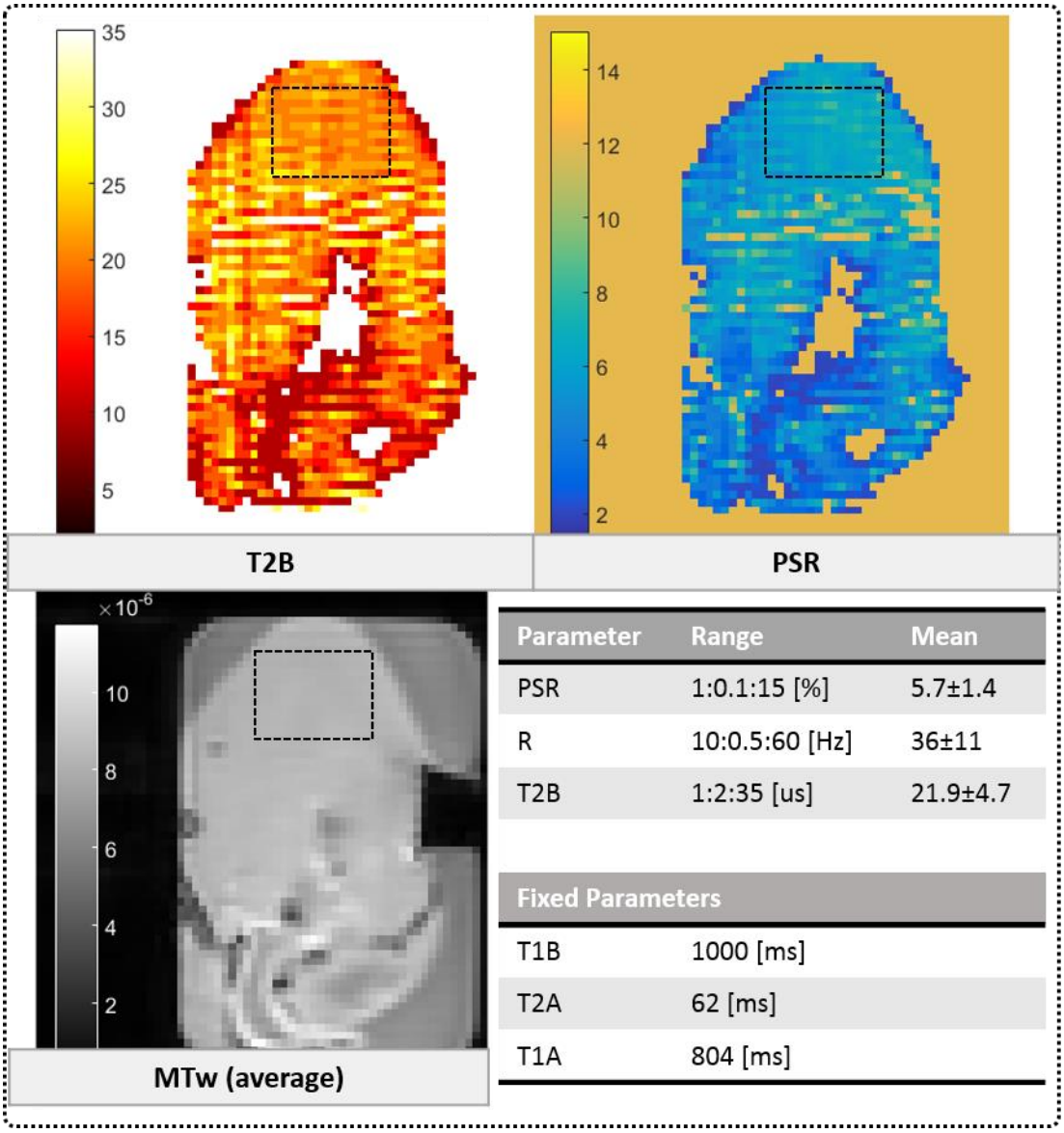

Parameter	Range	Mean
PSR	1:0.1:15 [%]	5.7±1.4
R	10:0.5:60 [Hz]	36±11
T2B	1:2:35 [us]	21.9±4.7

Fixed Parameters	
T1B	1000 [ms]
T2A	62 [ms]
T1A	804 [ms]

***Figure 7-6**. Above, T2B and PSR maps of a butcher's pig heart. Bottom left, average of MT-weighted slices obtained with HD-PROST reconstruction and N25 acquisition protocol, corresponding to the maps above. Bottom right, MT measured parameters PSR, R and T2B, and MT input parameters T1B (fixed), T2A (independently measured) and T1A (independently measured).*

Volunteers

A comparison of non-motion corrected and motion-corrected SENSE slices (MT preparation: flip angle 720 and frequency offset 3.9 kHz) is shown in **Figure 7-7A-B**. The same slice is also shown for a motion-corrected HD-PROST reconstruction in **Figure 7-7C**. The HD-PROST

motion-corrected datasets showed good image quality relative to SENSE and non-motion corrected datasets, as also observed in **Figure 7-8**.

Figure 7-8 shows slices of the motion-corrected "arithmetic" mean of the 8 MTw HD-PROST datasets acquired in the human subject in coronal view. The image quality appears good as features of the papillary muscle in the left ventricle can be easily identified. Other small features such as vessels in the liver and coronary arteries are also visible, despite the relatively low spatial resolution (1.8 mm3).

PSR maps were fairly homogenous but T2B maps showed an increased difference between septal and lateral ROIs (as seen in **Figure 7-9**). Nonetheless, mean values in septal and lateral ROIs were within generally expected ranges (e.g., bovine muscle [23]) in both maps, namely, lateral PSR=7.25±1.6 %, septal PSR=8.2±1.1 %, lateral T2B=14.1±1.7 μs and septal T2B=10.8±1.1 μs . Exchange rate (*R*) maps did not converge so a fixed value of R=36 Hz was used instead, obtained from the mean value of the HD-PROST phantom dataset using N25.

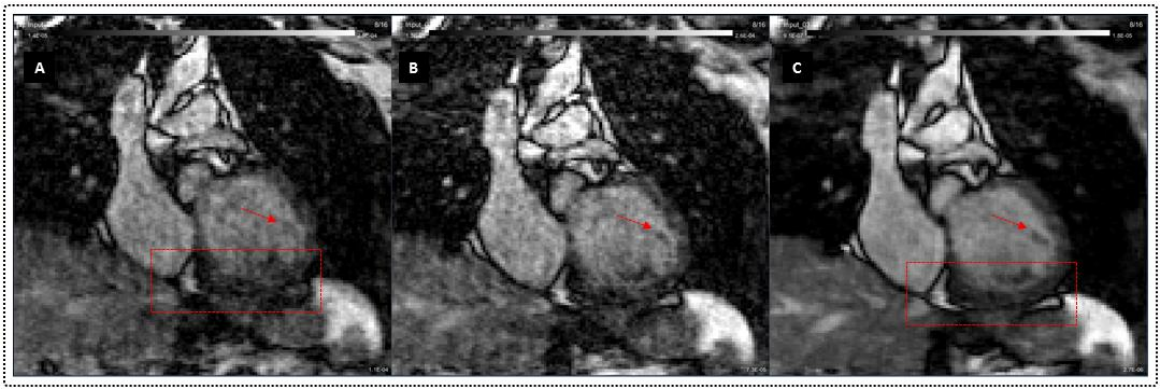

Figure 7-7*. (A) Non-motion corrected iterative SENSE reconstruction of an MT weighted dataset (flip angle 720 and frequency offset 3.9 kHz) acquired in a human subject. (B) Motion corrected iterative SENSE slice corresponding to that of (A). (C) Motion-corrected HD-PROST slice corresponding to that of (A) and (B). B shows better delineation of small features than A (see red arrow), however, C shows the best image quality in both delineation of small features and lack of motion artefacts at the myocardium/liver interface (see red square).*

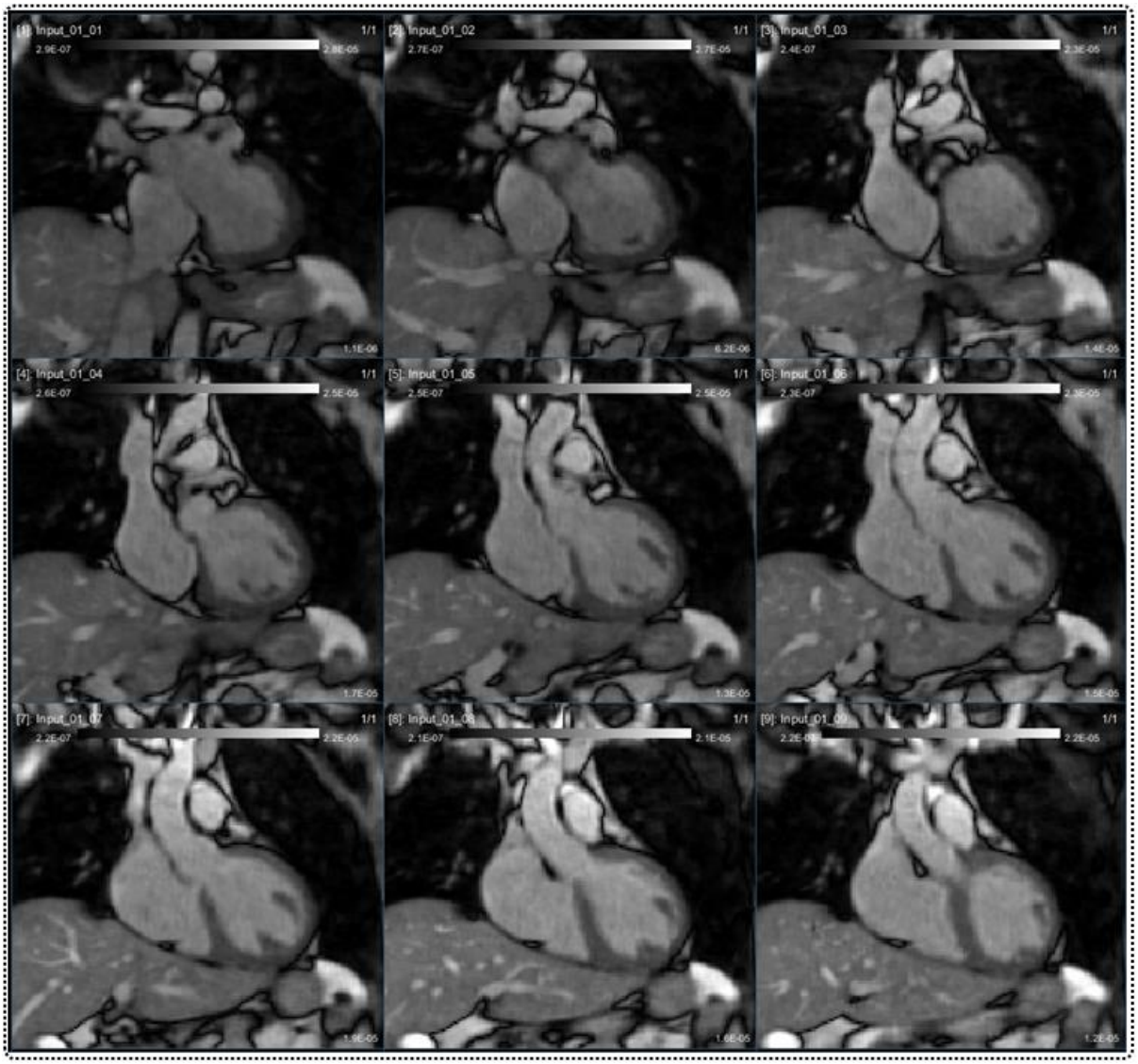

***Figure 7-8**. Coronal slices of the average of all MT-weighted datasets. Images were reconstructed using HD-PROST and acquired with acceleration factor 5 in a healthy human subject. Imaging parameters include resolution 1.7 mm^3, spoiled gradient echo acquistion with flip angle 15˚ and TE/TR=3.2/6.9 ms*

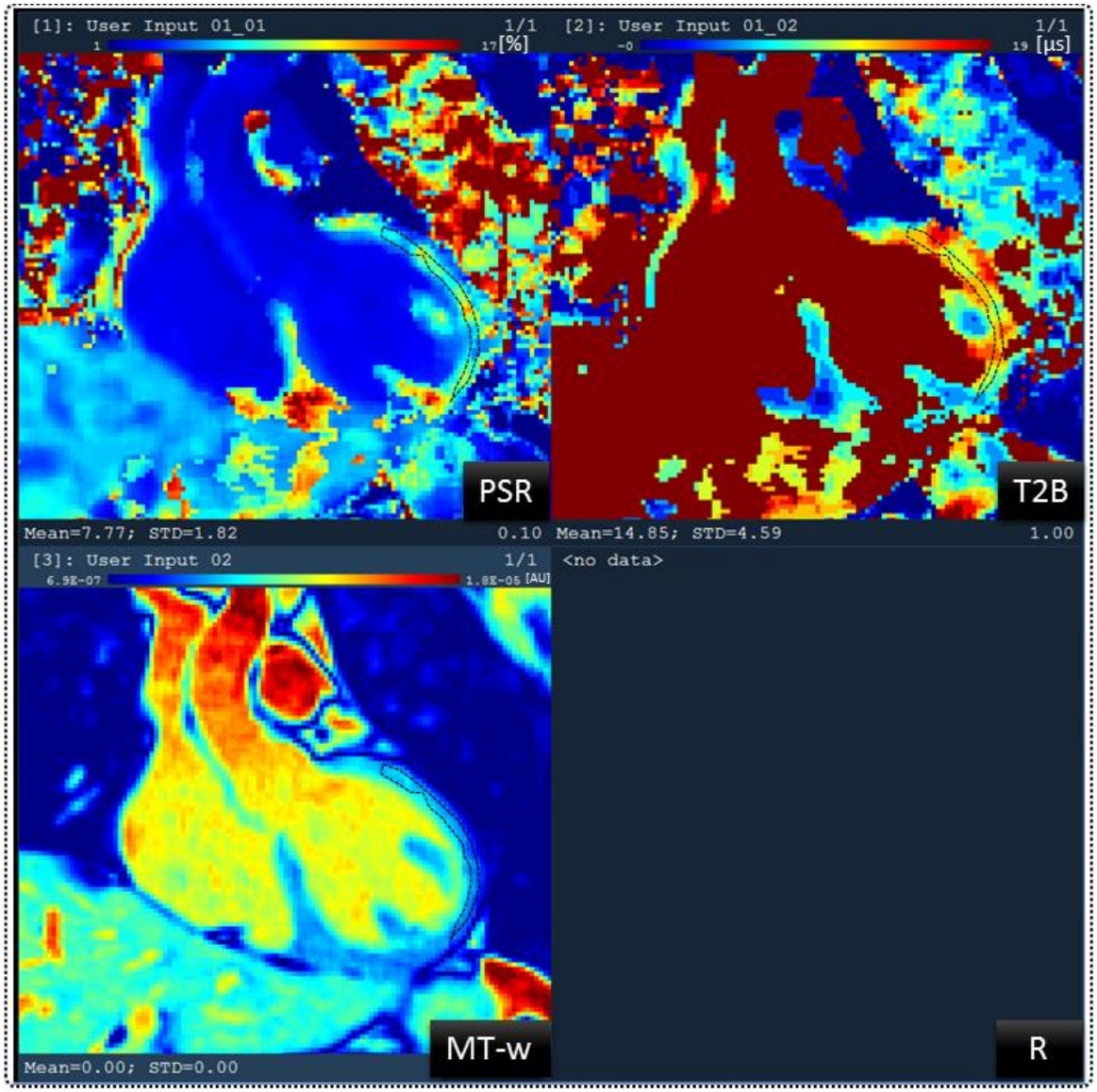

Figure 7-9*.MT parameter maps T2B and PSR along with corresponding MT weighted slice (arithmetic mean over 8 contrasts) for a healthy human subject, acquired using 8 MT contrasts, acceleration factor 5 and HD-PROST reconstruction after translational motion correction. A lateral region of interest (ROI) is drawn for measurement of MT parameter statistics.*

Discussion

Phantom experiments showed that the joint HD-PROST reconstruction can effectively reduce the noise on a multi-contrast batch of MT-weighted 3D images without significantly affecting the accuracy of quantitative MT measurements. A 3D patch-based denoising approach which applies SVD and truncation on already reconstructed images (method II) showed statistically

significant differences on parameter estimations. This suggests that the loss in accuracy of the signal/magnitude of each denoised MT-weigthed image may have a non-linear effect on the accuracy of MT parameter maps.

The experiments also showed that a reduction in the number of contrasts (or images) may introduce a bias in the estimation of MT parameters using the model/sequence proposed in this study, including PSR and T_2^B. It is not immediately clear which factor may have contributed to the increase in PSR and respective decrease in T_2^B values in protocols N8 and N5, but it is possible that the lack of contrasts on the low-saturation side of the MT spectrum may have skewed the matching towards the area in which EPG-X departs from ground truth (i.e. high saturation, see **Figure 7-3**). As EPG-X does not account for free-pool saturation during MT preparation, any free pool saturation that does occur may reflect a rapid increase in the model's MT saturation. A decrease in the T2 of the bound pool, which characterizes the shape and width of the spectrum (see equation *(7-2)*), would model a sharp increase in MT that happens mostly or only at the low-frequency region. In addition, the use of a single flip angle in the N25 protocol may have contributed to the differences observed with N8 and N5. Therefore, if possible, further studies may consider using an even larger number of measurements and multiple flip angles to determine the *ground truth*. Despite the apparent loss in accuracy, both N25 and N8 maps (see **Figure 7-6** and **Figure 7-9**) appeared homogenous and consistent throughout the myocardial tissue, as expected. This suggests that if the free pool saturation can be minimized or avoided altogether the maps may still hold significant potential.

The in-vivo 3D MTw datasets in a healthy human subject showed good image quality after translational motion correction and HD-PROST reconstruction. PSR and T_2^B maps appear to show potential for characterizing myocardial tissue in the beating heart, despite displaying some artefacts and apparently high sensitivity to noise. On the other hand, the model failed to converge in a homogenous R (exchange rate) map with values within the generally expected

range. This result was somewhat expected since *R* has the least amount of "weight" in the image's signal and the images were significantly affected by noise and imaging artefacts (e.g., free-pool saturation, under-sampling). However, it may be reasonable to expect that (due to its low weight) fixing R to a value within the general range of muscle tissue should not have an impact on the potential use of PSR or T_2^B maps to characterize myocardial tissue.

Conclusions

A proof-of-concept 3D whole heart free-breathing sequence for quantitative magnetization transfer imaging has been shown to characterize pool size ratio (PSR) and bound pool transverse relaxation times (T_2^B) in-vivo in a healthy human subject in approximately 9 minutes acquisition time. Although the maps appeared sensitive to noise and unwanted free pool saturation, the MT parameter maps (PSR and T_2^B) may hold significant potential for clinical applications and thus warrant further studies to explore other solutions to the challenges observed this work.

REFERENCES

1. Mewton, N., et al., *Assessment of myocardial fibrosis with cardiovascular magnetic resonance.* J Am Coll Cardiol, 2011. **57**(8): p. 891-903.
2. de Jong, S., et al., *Fibrosis and cardiac arrhythmias.* J Cardiovasc Pharmacol, 2011. **57**(6): p. 630-8.
3. van Oorschot, J.W., et al., *Endogenous contrast MRI of cardiac fibrosis: beyond late gadolinium enhancement.* J Magn Reson Imaging, 2015. **41**(5): p. 1181-9.
4. Ugander, M., et al., *Myocardial edema as detected by pre-contrast T1 and T2 CMR delineates area at risk associated with acute myocardial infarction.* JACC Cardiovasc Imaging, 2012. **5**(6): p. 596-603.
5. Stromp, T.A., et al., *Gadolinium free cardiovascular magnetic resonance with 2-point Cine balanced steady state free precession.* J Cardiovasc Magn Reson, 2015. **17**: p. 90.
6. Ward, K., A.E. Schussheim, and R.S. Balaban, *Contribution of mitochondria to cardiac muscle water/macromolecule proton magnetization transfer.* Magn Reson Med, 2003. **50**(6): p. 1312-6.
7. Saab, G., R.T. Thompson, and G.D. Marsh, *Multicomponent T2 relaxation of in vivo skeletal muscle.* Magn Reson Med, 1999. **42**(1): p. 150-7.

8. Levesque, I.R. and G.B. Pike, *Characterizing healthy and diseased white matter using quantitative magnetization transfer and multicomponent T(2) relaxometry: A unified view via a four-pool model.* Magn Reson Med, 2009. **62**(6): p. 1487-96.
9. Li, K., et al., *A rapid approach for quantitative magnetization transfer imaging in thigh muscles using the pulsed saturation method.* Magn Reson Imaging, 2015. **33**(6): p. 709-17.
10. Lopez, K., et al., *Quantitative magnetization transfer imaging for non-contrast enhanced detection of myocardial fibrosis.* Magn Reson Med, 2020.
11. Malik, S.J., R. Teixeira, and J.V. Hajnal, *Extended phase graph formalism for systems with magnetization transfer and exchange.* Magn Reson Med, 2018. **80**(2): p. 767-779.
12. Bustin, A., et al., *High-dimensionality undersampled patch-based reconstruction (HD-PROST) for accelerated multi-contrast MRI.* Magn Reson Med, 2019. **81**(6): p. 3705-3719.
13. Henningsson, M., et al., *Whole-heart coronary MR angiography with 2D self-navigated image reconstruction.* Magn Reson Med, 2012. **67**(2): p. 437-45.
14. Walsh, D.O., A.F. Gmitro, and M.W. Marcellin, *Adaptive reconstruction of phased array MR imagery.* Magn Reson Med, 2000. **43**(5): p. 682-90.
15. Bustin, A., et al., *Five-minute whole-heart coronary MRA with sub-millimeter isotropic resolution, 100% respiratory scan efficiency, and 3D-PROST reconstruction.* Magn Reson Med, 2019. **81**(1): p. 102-115.
16. Weigel, M., *Extended phase graphs: dephasing, RF pulses, and echoes - pure and simple.* J Magn Reson Imaging, 2015. **41**(2): p. 266-95.
17. Graham, S.J. and R.M. Henkelman, *Understanding pulsed magnetization transfer.* J Magn Reson Imaging, 1997. **7**(5): p. 903-12.
18. Morrison, C., G. Stanisz, and R.M. Henkelman, *Modeling magnetization transfer for biological-like systems using a semi-solid pool with a super-Lorentzian lineshape and dipolar reservoir.* J Magn Reson B, 1995. **108**(2): p. 103-13.
19. Ramani, A., et al., *Precise estimate of fundamental in-vivo MT parameters in human brain in clinically feasible times.* Magn Reson Imaging, 2002. **20**(10): p. 721-31.
20. Portnoy, S. and G.J. Stanisz, *Modeling pulsed magnetization transfer.* Magn Reson Med, 2007. **58**(1): p. 144-55.
21. Messroghli, D.R., et al., *Modified Look-Locker inversion recovery (MOLLI) for high-resolution T1 mapping of the heart.* Magn Reson Med, 2004. **52**(1): p. 141-6.
22. Akcakaya, M., et al., *Improved quantitative myocardial T2 mapping: Impact of the fitting model.* Magn Reson Med, 2015. **74**(1): p. 93-105.
23. Sled, J.G. and G.B. Pike, *Quantitative imaging of magnetization transfer exchange and relaxation properties in vivo using MRI.* Magn Reson Med, 2001. **46**(5): p. 923-31.

Chapter 8 : Closing statements

Summary

In **Chapter 1**, I discussed the specific motivations for this project and outlined the structure and contents of this report, including an assessment of the goals *vs* results along the way and final conclusions. Then, in **Chapter 2**, I discussed in detail the clinical concepts involved in this study, in addition to the fundamentals of the most widely adopted techniques in cardiac MR for the detection of myocardial fibrosis, highlighting their main advantages and challenges. I also presented a description of the physics and motivation for the use of Magnetization Transfer, with an emphasis on its current clinical applications and the potential of novel quantitative approaches in non-contrast enhanced myocardial tissue characterization. In **Chapters 3 and 4**, I described the theoretical basis for MR signal simulations, modelling and *Imaging* applied to cardiac MRI. I discussed the issue of respiratory motion and the need for accelerated image acquisition schemes in cardiac MRI, with special emphasis on a promising new techniques. Then, I presented the results of the experimental work carried out during the course of this project in **Chapters 5, 6 and 7**.

Chapter 5 described a three dimensional (3D) high-resolution free-breathing Magnetization Transfer Ratio (MTR) sequence for contrast-free assessment of myocardial infarct and coronary vein anatomy. Two datasets with and without off-resonance magnetization transfer preparation were sequentially acquired to compute MTR. 2D image navigators enabled beat-to-beat translational and bin-to-bin non-rigid motion correction. Two different imaging sequences were explored. MTR scar localization was compared against 3D late gadolinium enhancement (LGE) in a porcine model of myocardial infarction. MTR variability across the left ventricle and vessel sharpness in the coronary veins were evaluated in healthy human subjects. A decrease in MTR was observed in areas with LGE in all pigs (non-infarct:

25.1±1.7% vs infarct: 16.8±1.9%). The average infarct volume overlap on MTR and LGE was 62.5±19.2%. In humans, mean MTR in myocardium was between 37-40%. Spatial variability was between 15-20% of the mean value. 3D whole heart MT-prepared datasets enabled coronary vein visualization with up to 8% improved vessel sharpness for non-rigid compared to translational motion correction. MTR and LGE showed correlation in infarct detection and localization in a swine model but lack of histology was a limitation. In conclusion, free-breathing 3D MTR maps were shown to be feasible in humans but high spatial variability was observed. Therefore, the next part of the project was focused on separating out the contrast contributing factors from the effects of respiratory motion to tackle the spatial variability.

In **Chapter 6**, we develop a 2D gadolinium-free model-based quantitative magnetization transfer (qMT) technique to assess macromolecular changes associated with myocardial fibrosis. The proposed sequence consisted of a two-dimensional breath-held dual shot interleaved acquisition of five MT-weighted (MTw) spoiled gradient echo images, with variable MT flip angles and off-resonance frequencies. A two-pool exchange model and dictionary matching were used to quantify the pool size ratio (PSR) and bound pool T2 relaxation (T2B). The signal model was developed and validated using 25 MTw images on a Bovine Albumin Serum (BSA) phantom and in-vivo human thigh muscle. A protocol with 5 MTw images was optimized for single breath-hold cardiac qMT imaging. The proposed sequence was tested in 10 healthy subjects and 5 patients with myocardial fibrosis and compared to late gadolinium enhancement (LGE). PSR values in the BSA phantom were within the confidence interval of previously reported values (concentration 10% BSA=5.9±0.1%, 15% BSA=9.4±0.2%). PSR and T2B in thigh muscle were also in agreement with literature (PSR=10.9±0.3%, T2B=6.4±0.4us). In ten healthy subjects, global left ventricular PSR was 4.30±0.65%. In patients, PSR was reduced in areas associated with LGE (remote: 4.68±0.70% vs fibrotic: 3.12±0.78 %, n=5, $p<0.002$). In conclusion, in vivo model-based qMT mapping of

the heart was performed for the first time, with promising results for non-contrast enhanced assessment of myocardial fibrosis. Therefore, the final part of the project was focused translating the developed approach to 3D whole-heart imaging, to take advantage of the increased SNR and pursue T2B mapping.

Chapter 7 described a 3D free-breathing motion-corrected sequence for characterization of myocardial tissue using quantitative magnetization transfer imaging. A sequence for in-vivo cardiac imaging acquired 8 MT-prepared datasets in approximately 9 minutes in diastolic resting phase along with image navigators for beat-to-beat retrospective translational motion correction. The 8 undersampled datasets were jointly reconstructed using a high-dimensionality patch based reconstruction method that exploits the redundancy within and along the contrast dimension. A spin-bath model of exchange with Extended Phase Graph simulation was used to model the transient MT weighted signal of the measured datasets and to generate pool size ratio (PSR) and bound T2 (T2B) parameter maps based on dictionary matching. The sequence was evaluated in ex-vivo porcine myocardial tissue and in a healthy human subject. The ex-vivo measurements showed mean PSR value of 5.6±1.4%, mean T2B of 21.9±4.7μs and mean R of 36±11Hz, in accordance with similar studies in the literature. PSR and T2B mapping in the human subject showed promising results with respect to spatial variability of mean parameter values (PSR lateral 7.3±1.6% *vs* septal 8.2±1.1%, T2B: lateral 14.1±1.7μs *vs* septal 10.8±1.1μs) and clinical feasibility. Exchange rate mapping failed to converge in-vivo, while PSR and T2B maps appeared sensitive to noise and unwanted free-pool saturation.

Outlook

Further studies are still necessary to realise the full potential of free-breathing 3D quantitative MT imaging for non-contrast myocardial tissue characterization, yet, the results obtained along

each phase of this project in phantoms, healthy subjects and post myocardial infarction patients are substantial and appear to warrant the continuation of the same or a similar line of research.

Future studies could focus on correcting B1 inhomogeneities to improve the reproducibility of the matching (see **Chapter 6**, **Figure 6.3**, right) due to a lack of accuracy in the estimation of effective flip angle. For instance, this could be implemented using Chow's two point HASTE method [1] prior to the main sequence acquistion.

Alternatively, or in addition, future studies could be focused in accelerating the acquisition further (e.g., pushing for a higher undersampling) such that a higher number of MT contrasts can be acquired. As shown in **Chapter 7**, a high number of contrasts is desirable and reconstruction methods such as HD-PROST benefit from the redundancy.

Another aerea to be improved would be motion correction. For instance, 3D (or 2D sagittal) image navigators could be implemented in order to account for anterior-posterior heart motion and/or non-rigid motion correction (see **Chapter 4**, Page 72) could help reducing the partial volume effect associated with small/thin features. A study focused on motion correction would greatly benefit from a substantive validation in non-moving *in-vivo* muscle, such as, human thigh.

Thus, multiple areas of improvement are possible and the future of quantitative magnetization transfer in myocardial tissue characterization looks promising.

REFERENCES

1. Chow, K., I. Paterson, and R. Thompson, *1136 Cardiovascular radiofrequency (B1) field maps using HASTE*. Journal of Cardiovascular Magnetic Resonance, 2008. **10**(1): p. A261.